GREEN SYTNHESIS AND CHARACTERIZATION OF METAL OXIDE NANOPARTICLES: Fe (IRON), Cu (COPPER), AND Zn (ZINC)

by

Hüseyin Şengönül

B.S., Chemistry Education, Boğaziçi University, 2020

Submitted to the Institute for Graduate Studies in
Science and Engineering in partial fulfillment of
the requirements for the degree of
Master of Science

Graduate Program in Chemistry

Boğaziçi University

2023

Dedicated to my grandmothers

ACKNOWLEDGEMENTS

Firstly, I would like to express my heartfelt gratitude to Assoc. Prof. Oktay Demircan for his dedicated mentorship. His insightful feedback and constructive criticism have profoundly influenced not only the content of this thesis but also my academic growth. I am thankful to him for allowing me to work in his lab and providing constant motivation, especially during times when I felt discouraged.

I would also like to express my deep gratitude to Prof. Amitav Sanyal for his valuable guidance and for allowing me to use the facilities in the Sanyal Lab during the development of this study.

I am also thankful to Assoc. Prof. Sarp Kaya for reviewing my thesis and being on my thesis committee.

I would like to extend my heartfelt appreciation and gratitude to my lab friends who have been an invaluable source of support and camaraderie throughout this research journey. Their encouragement, insightful discussions, and collaborative spirit have significantly contributed to the success of this study. I am deeply grateful to Ayşenur Eslem, Çağla, Müşerref, Furkan, Janset, İpek, and Miraç for their friendship and support. I am also thankful to all my friends in the Department of Chemistry for creating unforgettable memories.

I would like to thank TÜBİTAK for their financial support as a recipient of the 2210-A scholarship and Boğaziçi University for their financial support in the BAP project (Project No: 21B05P5).

Last but not least, I would like to thank my family for their unwavering love, support, and understanding of my academic journey. Their belief in me has been instrumental in my achievements. I dedicate this study to the loving memory of my grandmothers, Gülveren, who passed away in 2017, and Sudiye, who passed away in 2023.

ABSTRACT

GREEN SYTNHESIS AND CHARACTERIZATION OF METAL OXIDE NANOPARTICLES: Fe (IRON), Cu (COPPER), AND Zn (ZINC)

The interest in the green synthesis of nanoparticles has significantly increased in the last decade as an alternative approach to chemical nanoparticle synthesis. Green synthesis is a technique that produces highly valuable materials by minimizing hazardous chemicals and using environmentally friendly, low-cost, and energy and time-saving materials, such as plant-based, industrial wastes, and recycled substances. This study presents the isolation and characterization of quercetin from *Prunus serrulata* (cherry blossom) and aims to control and understand the synthesis of nanoparticles (iron oxide, copper oxide, and zinc oxide) utilizing *Prunus serrulata* leaf extract as both reducing and capping agents. The effects of the mixing ratio of the volume of metal ions solution to *Prunus serrulata* leaf extract, the concentration of metal ions solutions, the pH, and the temperature of the reaction on the synthesis of nanoparticles are examined individually. The characterization of the plant-mediated extract is completed through Ultraviolet-Visible Spectroscopy (UV-Vis), Fourier Transform-Infrared Spectroscopy (FT-IR), Liquid Chromatography-Mass Spectrometry (LC-MS), and Nuclear Magnetic Resonance Spectroscopy (NMR). The synthesized nanoparticles were characterized by several instrumental analyses including FT-IR, scanning electron microscopy (SEM), energy dispersive X-ray spectroscopy (EDX), X-ray diffraction (XRD), and X-ray photoelectron spectroscopy (XPS). The optimum conditions for all of the synthesized nanoparticles were determined separately. For Fe_3O_4 nanoparticles, it follows as: 3:1 (Fe^{+3} solution:*Prunus serrulata* leaf extract) mixing ratio, 10 mM Fe^{+3} solution, pH 6, and 25 °C reaction temperature. For CuO nanoparticles, it follows as: 2:1 (Cu^{+2} solution:*Prunus serrulata* leaf extract) mixing ratio, 25 mM Cu^{+2} solution, pH 5, and 25 °C reaction temperature. Finally, for ZnO nanoparticles, it follows as: 2:1 (Zn^{+2} solution:*Prunus serrulata* leaf extract) mixing ratio, 25 mM Zn^{+2} solution, pH 5, and 25 °C reaction temperature.

ÖZET

METAL OKSİT NANOPARÇACIKLARININ YEŞİL SENTEZİ VE KARAKTERİZASYONU: Fe (DEMİR), Cu (BAKIR) VE Zn (ÇİNKO)

Nanoparçacıkların kimyasal yöntemlerle sentezlenmesine alternatif bir yaklaşım olan nanoparçacıkların yeşil sentezine olan ilgi, son on yılda önemli ölçüde artmıştır. Yeşil sentez, zararlı kimyasalları en aza indirgeyip, çevre dostu, düşük maliyetli, enerji ve zamandan kazandıran bitki bazlı, geri dönüştürülmüş maddeler ve endüstriyel atık gibi malzemeleri kullanarak yüksek değerli malzemeler üreten bir yöntemdir. Bu çalışma, quercetin'in *Prunus serrulata*'dan (kiraz çiçeği) izole ve karakterize edilmesini, sonrasında *Prunus serrulata*'dan hazırlanan yaprak özünün indirgeyici ve yüzey aktif malzeme olarak kullanılarak bu nanoparçacıkların (demir oksit, bakır oksit ve çinko oksit) sentezini anlamayı ve kontrol etmeyi amaçlar. Metal iyon çözeltisi hacminin *Prunus serrulata* yaprak özü karışımına hacminin oranının, metal iyon çözeltilerinin konsantrasyonunun, pH'nin ve reaksiyon sıcaklığının nanoparçacıkların sentezi üzerindeki etkileri tek tek incelenmiştir. Yaprak özünün karakterizasyonu Ultraviyole ve görünür ışık Spektroskopisi (UV-Vis), Fourier Dönüşümlü Kızılötesi Spektroskopisi (FT-IR), Sıvı Kromatografi-Kütle Spektrometresi (LC-MS) ve Nükleer Manyetik Rezonans (NMR) yöntemleri kullanılarak yapılmıştır. Sentezlenen nanoparçacıklar FT-IR, Taramalı Elektron Mikroskobu (SEM), Enerji Dağılımlı X-Işını Spektroskopisi (EDX), X-Işını Kırınımı (XRD) ve X-Işını Fotoelektron Spektroskopisi (XPS) yöntemleri kullanılarak karakterize edilmiştir. Sentezlenen nanoparçacıklarının her biri için ayrı ayrı en uygun koşullar belirlenmiştir. Fe_3O_4 nanoparçacıkları için en uygun koşullar şu şekildedir: 3:1 (Fe^{+3} solüsyonu:*Prunus serrulata* yaprak özü) karıştırma oranı, 10 mM Fe^{+3} solüsyonu, pH 6 ve 25 °C reaksiyon sıcaklığı. CuO nanoparçacıkları için: 2:1 (Cu^{+2} solüsyonu:yaprak özü) karıştırma oranı, 25 mM Cu^{+2} solüsyonu, pH 5 ve 25 °C reaksiyon sıcaklığı. Son olarak ZnO nanoparçacıkları için: 2:1 (Zn^{+2} solüsyonu:yaprak özü) karıştırma oranı, 25 mM Zn^{+2} solüsyonu, pH 5 ve 25°C reaksiyon sıcaklığı şeklindedir.

TABLE OF CONTENTS

ACKNOWLEDGEMENTS iv

ABSTRACT v

ÖZET vi

LIST OF FIGURES ix

LIST OF TABLES xiv

LIST OF ACRONYMS/ABBREVIATIONS xv

1. INTRODUCTION 1

1.1. Nanoparticles 1

1.1.1. Types of Nanoparticles 1

1.1.2. Synthesis of Nanoparticles 2

1.1.3. Applications of Nanoparticles 5

1.1.4. Green Synthesis of Nanoparticles 7

1.2. Iron Oxide Nanoparticles 8

1.3. Copper Oxide Nanoparticles 9

1.4. Zinc Oxide Nanoparticles 10

1.5. Characterization Techniques 10

1.5.1. Scanning Electron Microscopy (SEM) 10

1.5.2. Scanning Transmission Electron Microscopy (STEM) 11

1.5.3. X-Ray Diffraction (XRD) 11

1.5.4. X-Ray Photoelectron Spectroscopy (XPS) 11

1.5.5. Energy Dispersive X-Ray (EDX) 12

1.5.6. Ultraviolet-Visible Spectroscopy (UV-Vis) 12
1.5.7. Fourier-Transform Infrared Spectroscopy (FT-IR) 12
1.5.8. Liquid Chromatography-Mass Spectrometry (LC-MS) 12
1.5.9. Nuclear Magnetic Resonance Spectroscopy (NMR) 13
1.6. Aim of the Study 13
2. EXPERIMENTAL 15
2.1. Materials 15
2.2. Instrumentation 15
2.3. Preparation of *Prunus serrulata* Leaf Extract 17
2.4. Synthesis of Iron Oxide Nanoparticles 17
2.5. Synthesis of Copper Oxide Nanoparticles 18
2.6. Synthesis of Zinc Oxide Nanoparticles 19
3. RESULTS AND DISCUSSION 20
3.1. Characterization of *Prunus serrulata* Leaf Extract 20
3.2. Characterization of Iron Oxide Nanoparticles 24
3.3. Characterization of Copper Oxide Nanoparticles 39
3.4. Characterization of Zinc Oxide Nanoparticles 49
4. CONCLUSION 61
5. FUTURE WORK 62
REFERENCES 63
APPENDIX: ADDITIONAL FIGURES 74

LIST OF FIGURES

Figure 1.1. Different types of nanoparticles. 2

Figure 1.2. The illustration of the top-down and the bottom-up approaches. 2

Figure 1.3. The summary of three general synthesis methods for nanoparticles. 3

Figure 1.4. Different size comparisons of quantum size effect. 6

Figure 1.5. The illustration of XRD analysis. 11

Figure 2.1. The life cycle of the leaves of the *Prunus serrulata* tree. 16

Figure 2.2. Overall process of the synthesis of metal nanoparticles. 17

Figure 3.1. UV-Vis spectra of (a) *Prunus serrulata* leaf extracts in ACN, MeOH, and H_2O, and (b) *Prunus serrulata* leaf extract in H_2O and the synthesized Fe_3O_4 nanoparticles. 20

Figure 3.2. FT-IR spectra of (a) *Prunus serrulata* leaf extract in H_2O and (b) the synthesized Fe_3O_4 nanoparticles. 21

Figure 3.3. LC-MS spectrum of the *Prunus serrulata* leaf extract in H_2O after the synthesis of Fe_3O_4 nanoparticles. 22

Figure 3.4. The structure of quercetin, (b) the full ^{1}H-NMR spectrum of the quercetin dissolved from Fe_3O_4 nanoparticles, and (c) the enhanced spectrum of the same solution from 6.7 ppm to 8.7 ppm. 23

Figure 3.5. The SEM images of Fe_3O_4 nanoparticles synthesized in (a) a 3:1 ratio, (b) a 2:1 ratio, (c) a 1:1 ratio, and (d) a 1:2 ratio. 25

Figure 3.6. The XRD pattern of Fe_3O_4 nanoparticles synthesized in four different volume ratios. 26

Figure 3.7. The XPS spectra for the comparison of Fe_{2p} of Fe_3O_4 nanoparticles synthesized in four different volume ratios. 27

Figure 3.8. The SEM images of Fe_3O_4 nanoparticles synthesized with (a) 10 mM, (b) 25 mM, (c) 50 mM, and (d) 75 mM $FeCl_3$. 28

Figure 3.9. The XRD pattern of Fe_3O_4 nanoparticles synthesized with four different concentrations. 29

Figure 3.10. The XPS spectra for the comparison of Fe_{2p} of Fe_3O_4 nanoparticles synthesized with four different concentrations. 30

Figure 3.11. The SEM images of Fe_3O_4 nanoparticles synthesized by adjusting the pH values to (a) 4, (b) 6, (c) 8, and (d) 10. 31

Figure 3.12. The XRD pattern of Fe_3O_4 nanoparticles synthesized at the four different pH values. 32

Figure 3.13. The XPS spectra of Fe_3O_4 nanoparticles synthesized at the four different pH values. 33

Figure 3.14. The SEM images of Fe_3O_4 nanoparticles synthesized at (a) 25 °C, (b) 45 °C, and (c) 65 °C. 34

Figure 3.15. The XRD pattern of Fe_3O_4 nanoparticles synthesized at three different temperatures. 35

Figure 3.16. The (a) FT-IR spectroscopy and (b) EDX spectrum of the Fe_3O_4 nanoparticles with *Prunus serrulata* leaf extract under the optimum conditions. 36

Figure 3.17. The STEM images of the Fe_3O_4 nanoparticles synthesized under the optimum conditions from two different scales: (a) 500 nm and (b) 100 nm. 36

Figure 3.18. The XPS spectra of the Fe_3O_4 nanoparticles synthesized using *Prunus serrulata* leaf extract under the optimum conditions including the (a) survey and (b) Fe_{2p} (c), C_{1s}, (d) O_{1s}, and (e) N_{1s} profiles of the Fe_3O_4 nanoparticles. 38

Figure 3.19. The SEM images of CuO nanoparticles synthesized in (a) a 3:1 ratio, (b) a 2:1 ratio, (c) a 1:1 ratio, and (d) a 1:2 ratio. 40

Figure 3.20. The XRD pattern of CuO nanoparticles synthesized in four different volume ratios. 41

Figure 3.21. The SEM images of CuO nanoparticles synthesized with (a) 10 mM, (b) 25 mM, (c) 50 mM, and (d) 75 mM Cu^{+2} solution..... 42

Figure 3.22. The XRD pattern of CuO nanoparticles synthesized with four different concentrations. 43

Figure 3.23. The SEM images of CuO nanoparticles synthesized at (a) 25 °C, (b) 45 °C, and (c) 65 °C. 44

Figure 3.24. The XRD pattern of CuO nanoparticles synthesized at three different temperatures. 45

Figure 3.25. The (a) FT-IR spectroscopy and (b) EDX spectrum of the CuO nanoparticles with *Prunus serrulata* leaf extract under the optimum conditions. 46

Figure 3.26. The STEM images of the CuO nanoparticles synthesized under the optimum conditions from two different scales: (a) 200 nm and (b) 100 nm. 46

Figure 3.27. The XPS spectra of the CuO nanoparticles synthesized using *Prunus serrulata* leaf extract under the optimum conditions including the (a) survey and (b) Cu_{2p} (c), C_{1s}, (d) O_{1s}, and (e) N_{1s} profiles of the CuO nanoparticles. 48

Figure 3.28. The SEM images of ZnO nanoparticles synthesized under different conditions: (a) immediate pH adjustment, (b) pH adjustment after stabilization, and (c) no pH adjustment. 50

Figure 3.29. The SEM images of ZnO nanoparticles synthesized in (a) a 3:1 ratio, (b) a 2:1 ratio, (c) a 1:1 ratio, and (d) a 1:2 ratio. 51

Figure 3.30. The XRD pattern of ZnO nanoparticles synthesized in four different volume ratios. 52

Figure 3.31. The SEM images of ZnO nanoparticles synthesized with (a) 10 mM, (b) 25 mM, (c) 50 mM, and (d) 75 mM Zn^{+2} solution. 53

Figure 3.32. The XRD pattern of ZnO nanoparticles synthesized with four different concentrations. 54

Figure 3.33. The SEM images of ZnO nanoparticles synthesized at (a) 25 °C, (b) 45 °C, and (c) 65 °C. 55

Figure 3.34. The XRD pattern of ZnO nanoparticles synthesized at three different temperatures. 56

Figure 3.35. The (a) FT-IR spectroscopy and (b) EDX spectrum of the ZnO nanoparticles with *Prunus serrulata* leaf extract under the optimum conditions. 57

Figure 3.36. The STEM images of the ZnO nanoparticles synthesized under the optimum conditions from two different scales: (a) 50 nm and (b) 100 nm. 57

Figure 3.37. The XPS spectra of the ZnO nanoparticles synthesized using *Prunus serrulata* leaf extract under the optimum conditions including the (a) survey and (b) Zn_{2p} (c), C_{1s}, (d) $O_{1}s$, and (e) N_{1s} profiles of the ZnO nanoparticles. 59

Figure A.1. The ^{1}H-NMR spectrum of *Prunus Serrulata* leaf extract in CD_3CN. 74

Figure A.2. The ^{1}H-NMR spectrum of *Prunus Serrulata* leaf extract in CD_3OD. 75

Figure A.3. The ^{1}H-NMR spectrum of *Prunus Serrulata* leaf extract in D_2O. 75

LIST OF TABLES

Table 1.1. General synthesis methods and their importance. 5

Table 2.1. The chemicals that are used in this study. 15

LIST OF ACRONYMS/ABBREVIATIONS

ACN	Acetonitrile
BF	Bright Field
CD_3CN	Acetonitrile-d3
CD_3OD	Methanol-d4
CTAB	Cetyltrimethylammonium bromide
CuO	Copper (II) oxide
$CuSO_4.5H_2O$	Copper sulfate pentahydrate
D_2O	Deuterium oxide
EDX	Energy Dispersive X-Ray
$Fe(NO_3)_3$	Iron (III) nitrate
Fe_3O_4	Iron (II, III) oxide
$FeCl_2$	Iron (II) chloride
$FeCl_3$	Iron (III) chloride
FT-IR	Fourier-Transform Infrared Spectroscopy
GC-MS	Gas Chromatography-Mass Spectrometry
GO	Graphene oxide
H_2O	Water
HAADF	High-angle annular dark-field
HMDB	The Human Metabolome Database
LC-MS	Liquid Chromatography-Mass Spectrometry
M/MO_x NPs	Metal/metal oxide nanoparticles
MeOH	Methanol
NaOH	Sodium hydroxide
NMR	Nuclear Magnetic Resonance Spectroscopy
rGO	Reduced graphene oxide
Se	Selenium
SEM	Scanning Electron Microscopy
STEM	Scanning Transmission Electron Microscopy
UV	Ultraviolet
UV-Vis	Ultraviolet-Visible Spectroscopy

XPS	X-Ray Photoelectron Spectroscopy
XRD	X-Ray Diffraction
$Zn(NO_3)_2.6H_2O$	Zinc nitrate hexahydrate
ZnO	Zinc oxide

1. INTRODUCTION

1.1. Nanoparticles

Improvements in nanotechnology and nanoscience have emerged remarkably in recent years. Nanoparticles, or nanocomposites are defined as particulate matter with dimensions between 1 nm and 100 nm [1]. They possess the unique property of having a high surface area to volume ratio which provides advantages for using them in many research fields [1]. Nanoparticles promote increased higher chemical activity and greater absorption and interaction with any kind of system.

Nanoparticles and small molecules are two different concepts of particulate nature. Nanoparticles can be engineered and modified to have desired properties, such as the implementation of magnetic properties through various chemical reactions. On the other hand, small molecules are used as they are and cannot be modified. For example, drugs used in cancer treatment with a smaller molecular structure have some limitations concerning side effects and cytotoxicity whereas nanoscale drug carriers like metal nanoparticles are employed to address this problem [2].

1.1.1. Types of Nanoparticles

There have been countless research works with several types of nanoparticles in the literature. Nanoparticles can be divided into three different groups: organic, inorganic, and carbon-based [3]. Organic nanoparticles contain nanoparticles such as lipids, polymeric structures, and dendrimers, whereas inorganic nanoparticles contain metal/metal oxides, mesoporous silica, core-shell structures, and quantum dots [4]. In addition to these, carbon nanotubes and graphene oxide nanoparticles can be presented under carbon-based nanoparticles since they have different carbon arrangements. Different types of nanoparticles are illustrated in Figure 1.1.

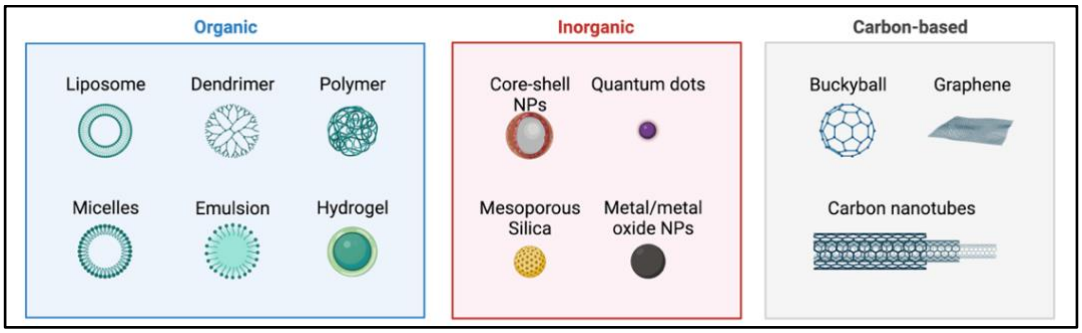

Figure 1.1. Different types of nanoparticles.

1.1.2. Synthesis of Nanoparticles

Generally, there are two ways of nanoparticle synthesis: top-down and bottom-up approaches seen in Figure 1.2. The top-down way of synthesizing nanoparticles is defined as reducing the size of the bulk material toward to nanoscale. On the other hand, the bottom-up approach refers to producing nanomaterials from smaller atoms and molecules [5]. The top-down approach requires more energy to synthesize nanoparticles compared to the bottom-up method. Furthermore, manufacturing small-sized nanoparticles and controlling the morphology of nanoparticles is limited by using physical methods. However, the bottom-up approach is the more acceptable and effective method [6]. The bottom-up approach involves chemical reactions. In this method, variations of the reaction precursors and different reaction conditions such as temperature and pH can influence the size and shape of the nanoparticles whilst obtaining the desired morphology. Hence, controlling the morphology of the nanoparticles is better in the bottom-up approach.

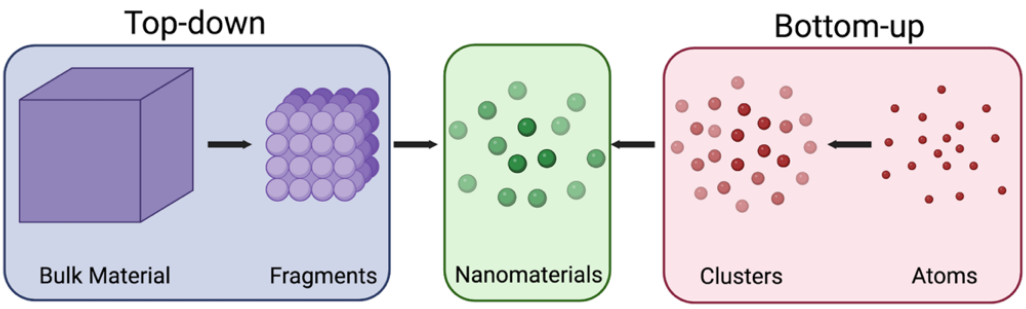

Figure 1.2. The illustration of the top-down and the bottom-up approaches.

Various chemical reactions and methods have been developed for the production of nanoparticles based on the bottom-up methodology. Sol-gel processing [7], hydrothermal synthesis [8], co-precipitation [9], thermal decomposition [10], and microemulsion [11] methods are some of the techniques based on the bottom-up approach, excluding the thermal decomposition method since it is based on the top-down approach for the nanoparticle synthesis. In addition to these methods, interest in the green synthesis of nanoparticles using biological materials has emerged over the last decade. All these paths through chemical synthesis have been used to build a common method of synthesizing different types of nanoparticles for many different research fields. Different methods of synthesis are summarized in Figure 1.3.

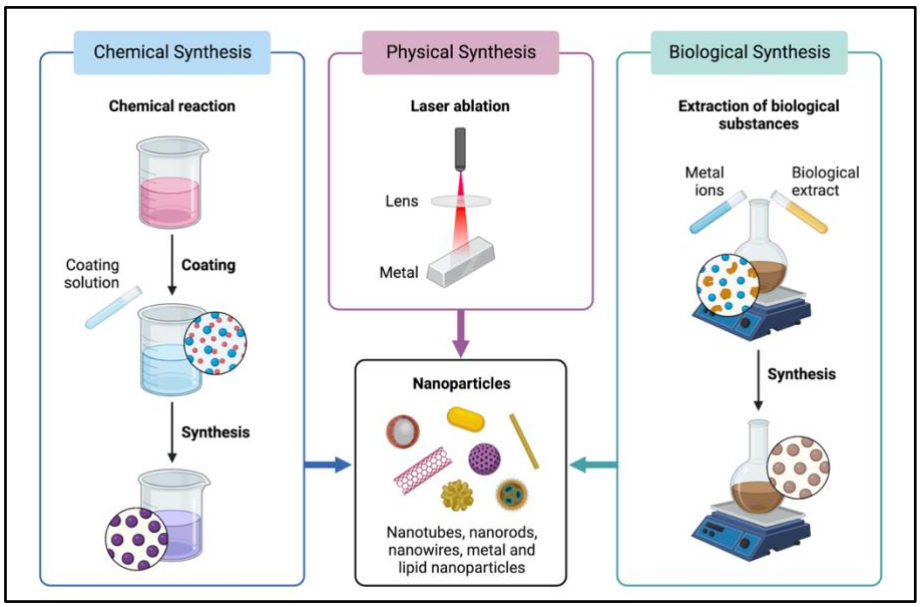

Figure 1.3. The summary of three general synthesis methods for nanoparticles.

The sol-gel process is one of the techniques that are used frequently for the synthesis of nanoparticles. In this method, the sol (colloidal suspension) obtained from metallic alkoxides, or organometallic precursor goes through phase transformations in order to produce gel (gelatin form of liquid) material [9]. First, the chemical reaction between metallic alkoxides and water, in the pH-dependent environment, occurs through hydrolyzation and condensation of metallic alkoxides [12]. Later, the solvent within the reaction containing metallic alkoxides is removed by drying with proper heating, and the final product is obtained.

Hydrothermal synthesis is one of the oldest methods used for many years. It has been used successfully for the synthesis of microporous crystals, ionic conductors, luminescence phosphors, and nanomaterials [13]. Essentially, it is a solution reaction-based approach that includes the use of solvents with high boiling temperatures and various types of surfactants in a controlled environment [14]. The reactants are first dissolved in an aqueous medium, then ions are separated due to the temperature difference, and finally, the dissolved material grows, and nanomaterials are produced [15].

The co-precipitation method is another classic method for the synthesis of magnetic nanoparticles. Precipitation of metal ions (e.g., Fe^{+2} or Fe^{+3}) can be established by adding a base (e.g., sodium hydroxide (NaOH)) into the metal ion solution [16]. It is easier to apply this method, but controlling the size and morphology is relatively low compared to other methods.

The thermal decomposition method is another chemical way of producing nanoparticles. However, this method is part of the top-down approach in which desired nanoparticles can be established from the bulk. In this method, magnetic nanoparticles are produced after a mixture of metal ions and surfactants decompose under high temperatures [17]. At the end of this process, featureless monodispersed nanoparticles are obtained [10]. Using this method requires a higher amount of energy compared to other methods, but a higher amount of yield is also obtained.

The microemulsion technique is a method that involves an oil and water mixture in micelles. In order to synthesize nanoparticles in micelles certain rules are required. First, a collision happens between two nonempty micelles to transfer of entire solute in one micelle and formation of the empty micelle, interchange of the reactants among the nanodroplets occurs when the fusion reaction between two micelles takes place later, and the nucleation reaction happens before the reaction growth step by an interchange of reactants and products [18]. In this case, reaction growth which is nanoparticle formation can be controlled by different parameters including reaction precursors, temperature, and pH.

Overall, the general synthesis conditions and some of the advantages of various methodologies are listed in under Table 1.1.

Table 1.1. General synthesis methods and their importance.

Synthesis Methods	**General Synthesis Conditions**	**Important Notes**
Sol-gel	Utilized under more than 100 °C temperature, organic solvents are used.	Controllable structures are obtained.
Hydrothermal	High pressure and temperature are required under aqueous environment.	Minimum loss of materials is achieved, nanomaterials are unstable at high temperatures.
Co-precipitation	Used under room temperature conditions, organic solvents are employed.	Easy to apply.
Thermal decomposition	Utilization of high temperatures (200-300 °C) and longer reaction times are required.	Produced nanoparticles are monodispersed and have narrow size distribution.
Microemulsion	A mixture of oil, surfactant, and water is used.	The produced nanoparticles may be divergent whereas reaction is hard to apply.
Biological/Green synthesis	Employed under room temperature conditions, water is used as solvent.	Easiest, cheapest, and environmental-friendly. The control on the synthesis is limited.

1.1.3. Applications of Nanoparticles

A distinguishing factor that interests in nanoparticles emerged in recent years is that they have unique properties of having a high surface area to volume ratio and quantum confinement effects. Having a high surface area to volume ratio means that a smaller amount of any substance might be useful for any specific subject. When the particle size decreases, atoms behave differently compared to particles that have larger sizes. For example,

nanocrystals with different sizes absorb and re-emit ultraviolet (UV) light and the emission wavelength changes with different sizes of the nanocrystals [19]. In the end, different colors of the spectrum might be observed depending on different sizes as illustrated in Figure 1.4.

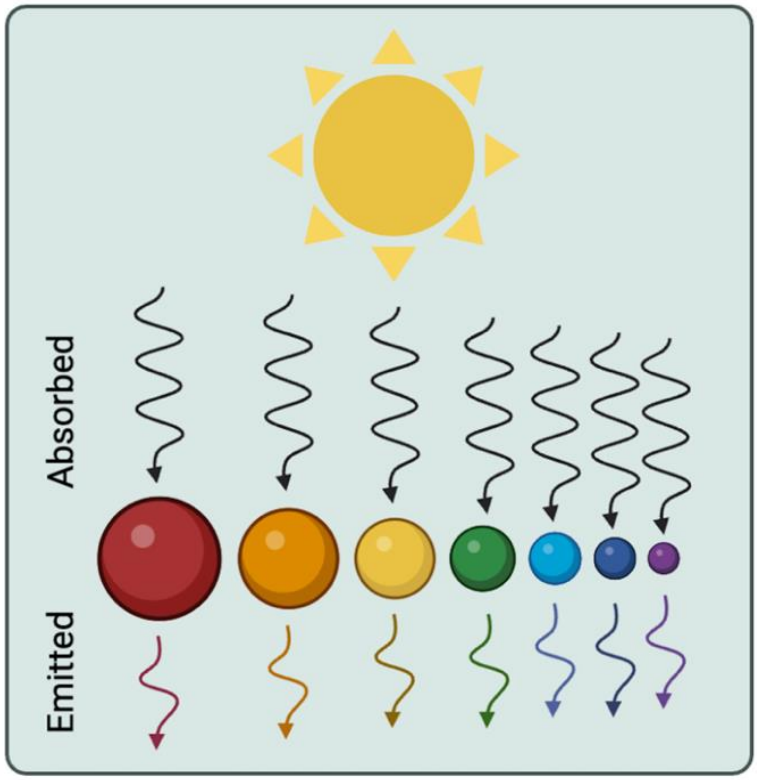

Figure 1.4. Different size comparisons of quantum size effect.

Biomedical nanoparticle research is one of the essential application fields where nanoparticles are frequently employed. Nanoparticles have been studied on different diseases such as cancer [20], HIV/AIDS [21], diabetes [22], and neurodegenerative diseases like Huntington's disease [23]. The common point of these diseases is that their treatments are inefficient and side effects are enormously dangerous during the process since they can cause death. Therefore, using the advantages of nanoparticles for the diagnosis, prevention, or treatment of diseases is highly valued [24]. For example, polymer brush-coated magnetic nanoparticles are produced for the diagnosis and early treatments, and the functionalization of these nanoparticles is accomplished by "clickable" functional groups which are called active sites to which only selected groups can attach, and moreover, new properties emerging from the nanoparticles can be employed to detect cancer cells earlier stages [25]. On the other hand, derivatives of graphene such as graphene oxide (GO) or reduced graphene oxide

(rGO) with a smaller number of oxygens compared to GO, are used in different biomedical applications thanks to their electrochemical properties. For example, nanocomposites of GO with polymers, gold, and different magnetic nanoparticles provide many advantages to biotechnological applications in phototherapy, bio-imaging, bio-sensing, gene, and drug delivery [26]. The electron transfer caused by the π-π^* transition between the orbitals of atoms in graphene oxide provides bio-sensing and bio-imaging applications due to the movement of delocalized π electrons [26]. Furthermore, rGO which is produced from GO by different methods including several chemical processes, is capable of having functionalized different organic groups that lead to usage in biomedical research.

Nutritional supplements including nanoparticles are another significant application area for nanoparticle research. Metal/metal oxide nanoparticles (M/MO_x NPs) are used in the nutrition industry not only for commercial purposes but also in the animal nutrition industry due to promising earlier results of using nanoparticles in animal nutrition. For example, selenium (Se) nanoparticles are used in both nutritional supplements [27] and animal nutrition productions [28]. However, due to the nature of itself, Se must be evaluated carefully since a higher amount of it in a supplementary diet might be toxic whereas a deficiency of Se might have problems in the body [29]. Se is found in nature in organic and inorganic forms. Organic Se is usually found in amino acids like selenocysteine, selenomethionine, selenohomocysteine, etc. whereas inorganic Se is usually found as selenium dioxide, selenious acid, and selenic acid [30]. Se is important for muscle growth, immunity functions, reproduction, and healthy and steady performance of organs in the body whilst it produces antioxidative properties and antibacterial activity [31]. Therefore, determining an appropriate amount of Se by using nanoparticles in nutritional supplements is vital for human health considering its capability of damage to the body.

1.1.4. Green Synthesis of Nanoparticles

The synthesis of nanoparticles using plant-based materials is called the green chemistry approach which is a part of both nanotechnology and biotechnology [32]. The green synthesis of nanoparticles requires plant-mediated extracts for both reduction and stabilization for the production of M/MO_x NPs. Polyphenols, terpenoids, flavonoids, and

phenolic acids are known to have a role in reduction and supporting stabilization for the green synthesis method.

Conventional chemical methods for the synthesis of nanoparticles have some limitations such as using of hazardous, toxic, and expensive chemicals, and the requirement of high temperature and pressure for the reaction takes place [33]. The toxicity of M/MO_x NPs must be considered seriously since the danger of contaminating the earth and causing adverse effects on human health can exacerbate the situation [34]. Using plant-based materials instead of chemicals prevents damage to the environment, reduces the cost of production, and most importantly, saves time by only a single-step chemical reaction for the synthesis of nanoparticles that have different sizes, morphologies, and crystal structures.

The green synthesis route is not restricted by only plant-based materials since it also includes different microorganisms [35] and fungi [36]. For example, it has been studied that Ag nanoparticles were synthesized by using MKH1 bacterium [37], and *Penicillium italicum* fungi [38] with further antioxidant activity of nanoparticles on *Staphylococcus aureus*, *Salmonella enterica*, Bacillus cereus, and *Escherichia coli* were also investigated.

On the other hand, the greatest challenge in the green synthesis of nanoparticles is the amount of the obtained product yield. Even though this method produces less harmful waste to the environment, product yield is much less than the nanoparticles synthesized with other chemical methods. Therefore, it is important to increase product yield by using every possible chemical ingredient of bioorganic molecules in leaf or seed extracts, microorganisms, and fungi.

1.2. Iron Oxide Nanoparticles

Iron oxide nanoparticles were widely distributed in various fields of nanoscience and have been used for many years. Mostly, iron oxide nanoparticles were primarily utilized for their magnetic properties in biomedical research, environmental remediation, and materials science. In biomedical research, they are employed in magnetic resonance imaging as contrast agents while they serve as carriers for drug delivery systems [39]. In environmental remediation, they are used for the removal of heavy metals and other pollutants from water

and rich soil [40]. In materials science, they are utilized as catalysts [41], and electrode materials [42].

There are a variety of techniques for synthesizing iron oxide nanoparticles including sol-gel, co-precipitation, thermal decomposition, microemulsion, etc. Each of these techniques has their own advantages and disadvantages. The choice of approach relies on the specific application and desired properties of the iron oxide nanoparticles. The common point of these methods is that they all include several chemicals for the reaction precursor such as chloride or nitrate salts of iron ($FeCl_2$, $FeCl_3$, or $Fe(NO_3)_3$), reducing agents include sodium borohydride, or ascorbic acid, and many surfactants like cetyltrimethylammonium bromide (CTAB).

1.3. Copper Oxide Nanoparticles

Copper oxide nanoparticles have been employed in numerous fields for many years. Recently, new applications for copper oxide nanoparticles in catalysis, solar energy, and biomedical research have emerged. They serve as catalysts in a variety of chemical reactions, such as the selective oxidation of benzyl alcohols in the aqueous phase [43] and the catalytic reduction of methylene blue dye [44]. Copper oxide nanoparticles are utilized in the solar energy industry as p-type semiconductors with a 1.5 eV band gap energy which is close to the 1.4 eV energy gap for a solar energy system in its optimal state [45]. Also, copper oxide nanoparticles have been employed as antibacterial effects in biomedical studies [46]. Additionally, they also have the potential to be used as a cancer therapy by producing reactive oxygen species, which can play a significant role in causing the death of bladder cells [47].

Comparable methods that were utilized to produce iron oxide nanoparticles have also been employed to fabricate copper oxide nanoparticles. Sonochemical and electrochemical synthesis methods are also utilized in addition to sol-gel, microemulsion, and hydrothermal procedures. Sonochemical synthesis of copper oxide nanoparticles can be created by continuous utilization of high-frequency sound waves to form of novel nanostructure [48], whereas electrochemical synthesis can be established by applying a potential to copper electrodes in NaCl solution to produce copper oxide nanoparticles [49].

1.4. Zinc Oxide Nanoparticles

Zinc oxide nanoparticles are valuable in a variety of nanoscience applications due to their unique properties. They possess various beneficial features that range from electronics to cosmetics [50], such as semiconductor materials and UV absorbents for sunscreen protection industries [51], besides having low cost and stability [52]. Additionally, as iron oxide and copper oxide nanoparticles, zinc oxide nanoparticles have also been performed in biomedical research. They can be applied in the biomedical field, such as veterinary sciences to treat a variety of skin disorders and assist in wound healing [53].

Sol-gel, co-precipitation, hydrothermal process, thermal decomposition procedures, etc. are used in the synthesis of zinc oxide nanoparticles similar to iron oxide and copper oxide nanoparticles. As a result, all of these techniques have been used for many years with practically any metal. However, the toxicity of these nanoparticles must be carefully considered and should not be ignored.

1.5. Characterization Techniques

Several characterization techniques have been applied to various types of analytical methodologies for nanoparticle characterization. The surfaces, crystalline structures, and elemental composition of the materials have been examined by using several methods. Moreover, additional analysis methods are required to comprehend the mechanism occurring during the synthesis process.

1.5.1. Scanning Electron Microscopy (SEM)

Scanning Electron Microscopy (SEM) is a characterization technique that is used to observe high-resolution images of the surface of samples. The surface of the sample is scanned with an electron beam. Later, the electrons that are emitted or backscattered are used to produce final images. However, since it is difficult to detect scattered electrons from insulated materials, they are covered with conductive metals such as, platin and gold before the analysis. Finally, morphologies, sizes, and aggregations of the sample are observed.

1.5.2. Scanning Transmission Electron Microscopy (STEM)

Scanning Transmission Electron Microscopy (STEM) is a similar method compared to SEM. In this method, nanoparticles are observed with higher resolutions using various detectors such as bright field (BF) and high-angle annular dark-field (HAADF). These detectors facilitate the acquisition of images with a sense of depth. The samples are usually placed on the copper grid which allows collecting more electrons from the source.

1.5.3. X-Ray Diffraction (XRD)

X-Ray Diffraction (XRD) is an instrumental method that is employed to determine the crystal structure of a sample. Incident X-ray beams are sent across to the surface of materials. A detector is used to collect diffracted X-rays each of which has a specific angle for the crystalline structure of any given substance. Surface patterns are discovered with the data provided by the detector. Overall, the graphical representation of scattered patterns provides details about the crystal structure of the sample. The process is illustrated in Figure 1.5.

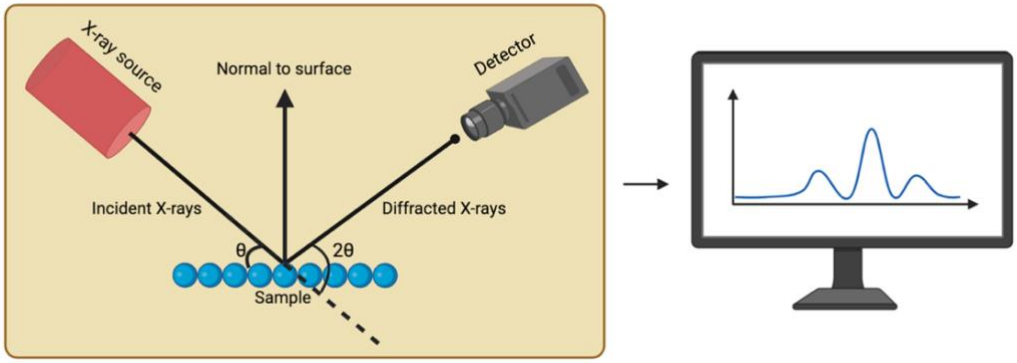

Figure 1.5. The illustration of XRD analysis.

1.5.4. X-Ray Photoelectron Spectroscopy (XPS)

X-Ray Photoelectron Spectroscopy (XPS) is another spectroscopic technique that is utilized to identify the chemical composition of samples. In this method, electrons within a sample absorb photons of certain energy until they are released from the sample later [54].

Details on the electronic states of atoms at the surface are obtained from binding energy calculations of emitted electrons.

1.5.5. Energy Dispersive X-Ray (EDX)

Energy Dispersive X-Ray (EDX) analysis is applied in conjunction with SEM to identify the elemental composition at the surface of nanomaterials [55]. However, it is important to note that this analytical technique is insufficient to comprehend the atomic behavior of elements, because a huge surface area, roughly deep in 2µm, is covered [56]. It is useful for identifying the overall elemental mapping of the sample and estimating elemental proportions.

1.5.6. Ultraviolet-Visible Spectroscopy (UV-Vis)

Ultraviolet-Visible Spectroscopy (UV-Vis) is a technique used to measure the absorbance of analytes, such as transition metal ions and biological molecules, utilizing ultraviolet light to identify their quantitative properties [57]. Additionally, it can be employed as an alternative approach to study nanoparticles by measuring their size and concentration and observing their stability, since destabilization of nanoparticles can trigger a decrease in intensity peaks [57].

1.5.7. Fourier-Transform Infrared Spectroscopy (FT-IR)

Fourier-Transform Infrared Spectroscopy (FT-IR) is used to identify and study the chemical composition of a sample by measuring the absorption or emission of infrared radiation. It is mostly used to determine various functional groups in organic molecules whereas inorganic compounds can be identified as well.

1.5.8. Liquid Chromatography-Mass Spectrometry (LC-MS)

Liquid Chromatography-Mass Spectrometry (LC-MS) is an effective analytical technique that is employed to separate, identify, and quantify both known and unknown substances as well as to clarify the structure and chemical properties of different molecules

[58]. It involves utilizing liquid chromatography to separate the components of a sample, followed by identification and quantification of the separated components using mass spectrometry. It has been used for compounds in plant materials, and it offers high selectivity.

1.5.9. Nuclear Magnetic Resonance Spectroscopy (NMR)

Nuclear Magnetic Resonance Spectroscopy (NMR) is a widely utilized and advanced analytical method that provides information about the structure and properties of molecules. The method works by applying a magnetic field to the atomic nuclei of atoms in the sample and then measuring the radio frequency radiation emitted by the nuclei to characterize the sample [59]. This is because different atomic nuclei have different chemical surroundings [59]. NMR is a non-destructive technique, meaning that it does not damage the sample or alter the sample, and the sample can be used for further analysis [60].

1.6. Aim of the Study

As explained in the introduction section, nanoparticles have a wide range of uses, and many studies have been conducted on their applications in medical science or materials science. However, it is no mystery that these studies are costly and generate a lot of waste. One solution to this issue is the conjunction of nanoparticles with cheap and environmental-friendly biomaterials. It is a necessity not only for scientific research but also for practical and commercial reasons. Considering these reasons, therefore, it is necessary to explore alternative, more cost-effective, and sustainable methods for synthesizing and analyzing various MO_x NPs.

The aim of this thesis is to synthesize and characterize iron oxide, copper oxide, and zinc oxide nanoparticles using a green synthesis pathway. To achieve this, *Prunus serrulata* leaves were utilized, and a leaf extract was prepared. The use of the leaf extract as both a reducing agent and stabilizing agent played a key role in reducing metal ions and obtaining the desired nanoparticles. The parameters affecting the formation of nanoparticles, including the mixing ratio of metal ion solution to leaf extract, concentration, pH, and temperature were examined. The characterization of the nanoparticles was carried out using SEM, XRD,

and XPS, whereas UV-Vis, FT-IR, LC-MS, and NMR were performed to characterize the leaf extract. *Prunus serrulata* leaves have never been studied as a part of green synthesis for any kind of M/MO_x NPs. It is an honor to have contributed to the addition of a new type of leaf to the literature on the synthesis of M/MO_x NPs.

2. EXPERIMENTAL

2.1. Materials

Prunus serrulata leaves were collected from North Campus, Boğaziçi University, Istanbul, Türkiye. The chemicals that are used in this study are shown in Table 2.1. Distilled water was employed as the solvent. All chemicals and the solvent were of analytical grade and used without additional purification.

Table 2.1. The chemicals that are used in this study.

Chemicals	Supplier
$FeCl_3$	Thermo Scientific
$CuSO_4.5H_2O$	Thermo Scientific
$Zn(NO_3)_2.6H_2O$	Thermo Scientific
NaOH	Merck

2.2. Instrumentation

Prunus serrulata leaf extract and the produced nanoparticles were characterized by the utilization of UV-Vis, FT-IR, LC-MS, NMR, SEM, STEM, EDX, XRD, and XPS analytical techniques.

The UV-Vis, FT-IR, LC-MS, and NMR methodologies were used to characterize *Prunus serrulata* leaf extract. The UV-Vis spectra were monitored using Varian Cary 100 Scan spectrophotometer, in the range of 250 nm to 800 nm with a resolution of 1 nm using quartz cuvettes. The FT-IR spectra were recorded utilizing the Thermo Scientific Nicolet 380 with an attenuated total reflectance attachment in the range of 400-4000 cm^{-1}. The LC-MS analysis was performed using the Shimadzu LC20AD with additional equipment. The NMR results were obtained by employing the Varian Mercury 400 MHz NMR at the Boğaziçi University Advanced Technologies Research and Development Center, North Campus of Boğaziçi University.

SEM and STEM results were obtained using the Thermo Scientific Quattro S by applying 5-20 kV voltage at the Center for Life Sciences and Technologies, Kandilli Campus of Boğaziçi University. The EDX results were recorded using the same instrument with an additional attachment at the same time. The XRD patterns were investigated employing the Rigaku D/MAX-Ultima+/PC with a 40 kV, 40 mA, 2°/min step size, and 0.02° scanning rate at the Boğaziçi University Advanced Technologies Research and Development Center, North Campus of Boğaziçi University. The XPS analysis was carried out with the Thermo Scientific K-Alpha X-Ray Photoelectron Spectrometer at the Koç University Surface Science and Technology Center, Rumelifeneri Campus of Koç University. The calculated binding energies were referenced to the adventitious C_{1s} peak at 284.5 eV.

Figure 2.1. The life cycle of the leaves of the *Prunus serrulata* tree.

2.3. Preparation of *Prunus serrulata* Leaf Extract

Fresh *Prunus serrulata* leaves in Figure 2.1 (All images were taken in 2022) were gathered from the North Campus of Boğaziçi University in Istanbul, Türkiye. The leaves were washed with tap water first, followed by washing with distilled water several times properly to remove dust and dirt. They were dried for 5 days at room temperature while kept away from direct sunlight. The dried leaves were then powdered using a coffee grinder.

Prunus serrulata leaf extract was obtained by the extraction of 2.5 g of dried powder in 50 mL of distilled water using a magnetic stirrer at 60 °C for 1 hour. The heated mixture was allowed to cool down at room temperature. The extract was filtered through a sieve first, then it was centrifuged to assist filtration. The resulting extract was then filtered through Whatman No. 1 filter paper. A known volume of the filtered extract was taken. The remaining extract was stored in the fridge at 4 °C for further use.

2.4. Synthesis of Iron Oxide Nanoparticles

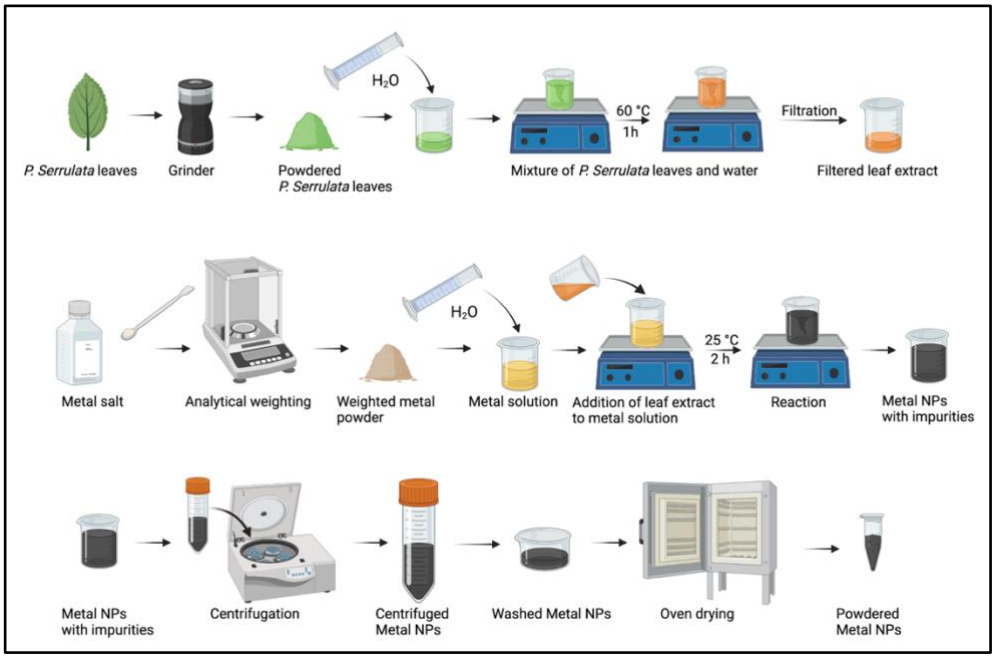

Figure 2.2. Overall process of the synthesis of metal nanoparticles.

Iron oxide nanoparticles were synthesized by employing *Prunus serrulata* leaf extract. An original experimental setup was configured for this study. Initially, the impact of mixing ratios of 3:1, 2:1, 1:1, and 1:2 on synthesis was examined while maintaining constant parameters: 10 mM $FeCl_3$, pH 6, and 25 °C. Second, the effect of concentrations of metal ion solution, Fe^{+3} solution, was investigated by tracking four different concentrations, 10 mM, 25 mM, 50 mM, and 75 mM whereas such parameters were kept constant: 3:1 mixing ratio, pH 6, 25 °C. Then, the reflection of four pH values of 4, 6, 8, and 10 on synthesis was observed while the following parameters were maintained constant: 3:1 mixing ratio, 10 mM $FeCl_3$, 25 °C. Finally, the effect of temperatures of 25 °C, 45 °C, and 65 °C on synthesis was observed while such parameters were kept constant: 3:1 mixing ratio, 10 mM $FeCl_3$, pH 6.

The reaction was initiated by the addition of *Prunus serrulata* leaf extract drop by drop into a specific $FeCl_3$ solution on a magnetic stirrer. Then, the pH for each reaction was adjusted employing 0.25 M NaOH to a predetermined value after the initiation of the reaction before it was left to complete for 2 hours. A black precipitate indicating the formation of iron (II, III) oxide (Fe_3O_4) nanoparticles was immediately observed after the addition of *Prunus serrulata* leaf extract. The obtained Fe_3O_4 nanoparticles were centrifuged for 10 minutes at 6000 round per minute (RPM). The product was washed twice with distilled water and once with ethanol to remove impurities. Finally, Fe_3O_4 nanoparticles were dried overnight in an oven at 80 °C. Overall process was illustrated in Figure 2.2.

2.5. Synthesis of Copper Oxide Nanoparticles

The same method of synthesis that was employed to produce iron oxide nanoparticles was correlated to produce copper oxide nanoparticles. The effects of mixing ratio, concentration, and temperature were investigated separately. Due to the previous iron oxide nanoparticles synthesis experimental results which are explained later, the pH effect is not considered. In this experiment, copper sulfate pentahydrate ($CuSO_4.5H_2O$) was used as a copper metal ion source. The mixing ratios of 3:1, 2:1, 1:1, and 1:2, concentrations of 10 mM, 25 mM, 50 mM, and 75 mM, and temperatures of 25 °C, 45 °C, and 65 °C were studied similarly to the Fe_3O_4 nanoparticles.

The reaction was initiated by the addition of *Prunus serrulata* leaf extract drop by drop into a specific $CuSO_4.5H_2O$ solution on a magnetic stirrer. The pH was adjusted by

employing 0.25 M NaOH to a predetermined value (pH 5) after the initiation of the reaction before it was left to complete for 2 hours. A brown precipitate indicating the formation of CuO nanoparticles was immediately observed after the addition of *Prunus serrulata* leaf extract. The produced CuO nanoparticles were centrifuged for 10 minutes at 6000 RPM. The product was washed twice with distilled water and once with ethanol to remove impurities. Finally, CuO nanoparticles were dried overnight in an oven at 80 °C.

2.6. Synthesis of Zinc Oxide Nanoparticles

A similar but not the same method was employed to produce zinc oxide (ZnO) nanoparticles. The effects of mixing ratio, concentration, and temperature were examined. Zinc nitrate hexahydrate ($Zn(NO_3)_2.6H_2O$) was used as a zinc ion source for the synthesis of ZnO nanoparticles. The pH effect on the synthesis of zinc oxide nanoparticles was not studied as explained previously on the synthesis of Fe_3O_4 nanoparticles, which it had no effect on the morphology or crystalline structure of the Fe_3O_4 nanoparticles. The synthesis of ZnO nanoparticles was modified. *Prunus serrulata* leaf extract and Zn^{+2} ions were reacted in three different ways: First, the Zn^{+2} ions and the leaf extract were mixed, and the pH was adjusted immediately for 2.5 hours. Second, the Zn^{+2} ions and the leaf extract were reacted initially for 1.5 hours, followed by the pH adjustment for another 1 hour. Third, only Zn^{+2} ions and the leaf extract reacted for 2.5 hours. The best method was identified, and the effects of mixing ratio, concentration, and temperature were investigated further.

The reaction was initiated by the addition of *Prunus serrulata* leaf extract drop by drop into a specific $Zn(NO_3)_2.6H_2O$ solution on a magnetic stirrer. Then, the pH was adjusted by employing 0.25 M NaOH to a predetermined value (pH 5) after the initiation of the reaction before it was left to complete for 2 hours. A brown-black precipitate indicating the formation of ZnO nanoparticles was immediately observed after the addition of *Prunus serrulata* leaf extract. The produced ZnO nanoparticles were centrifuged for 10 minutes at 6000 RPM. The product was washed twice with distilled water and once with ethanol to remove impurities. Finally, ZnO nanoparticles were dried overnight in an oven at 80 °C.

3. RESULTS AND DISCUSSION

3.1. Characterization of *Prunus serrulata* Leaf Extract

Prunus serrulata leaf extract was characterized to understand the nature behind its capability of reducing and stabilizing activities. In order to observe this, *Prunus serrulata* leaf extracts were prepared in several types of solvents, including acetonitrile (ACN), methanol (MeOH), and water (H_2O). UV-Vis, FT-IR, LC-MS, and NMR analyzes were conducted to determine the specific flavonoid responsible for the production of the nanoparticles.

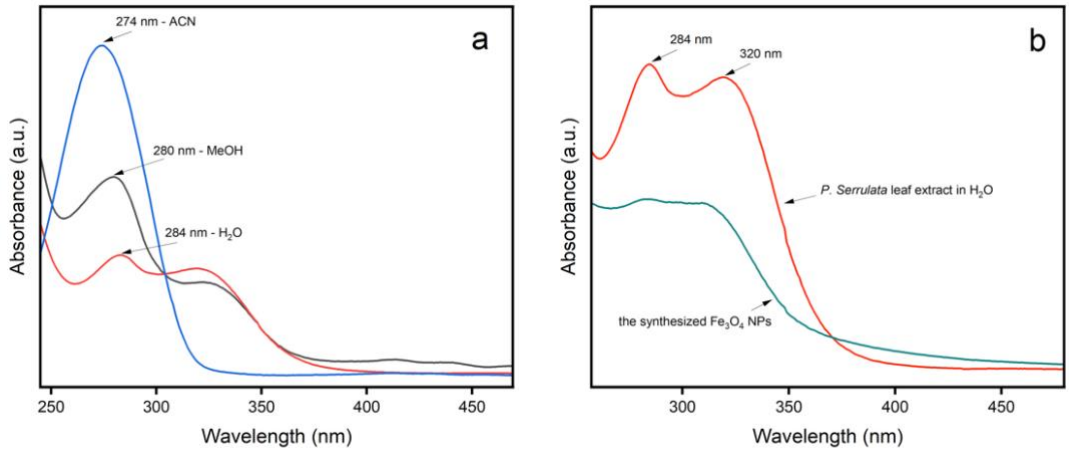

Figure 3.1. UV-Vis spectra of (a) *Prunus serrulata* leaf extracts in ACN, MeOH, and H_2O, and (b) *Prunus serrulata* leaf extract in H_2O and the synthesized Fe_3O_4 nanoparticles.

The UV-Vis spectra of *Prunus serrulata* leaf extracts in ACN, MeOH, and H_2O were examined in Figure 3.1a. The corresponding $\pi \rightarrow \pi^*$ transition of *Prunus serrulata* leaf extract in ACN showed an absorption peak at 274 nm, whereas the MeOH and H_2O extracts of *Prunus serrulata* leaves indicated absorption peaks at 280 nm and 284 nm, respectively. The bathochromic shift was observed as a result of the solvents which have different polarities. Moreover, the extract in ACN had a single peak whereas the MeOH and H_2O extracts had double peaks. Generally, leaf extracts contain many phytochemicals, and each solvent has the ability to dissolve different types of phytochemicals [61]. The

phytochemicals in the leaf extracts, particularly the flavonoids, are absorbed in the range of 270 nm to 320 nm according to similar studies [62–64]. Furthermore, the absorption peaks of the *Prunus serrulata* leaf extract in H_2O and the Fe_3O_4 nanoparticles were displayed in Figure 3.1b. The decrease in intensity of the absorption peaks of the *Prunus serrulata* leaf extract in H_2O after the reaction implied that the flavonoid content in the leaf extract was responsible for the reaction that took place which was also shown in a similar study [62]. Thus, UV-Vis spectroscopy results confirmed the preliminary detection of flavonoid content in the Fe_3O_4 nanoparticles.

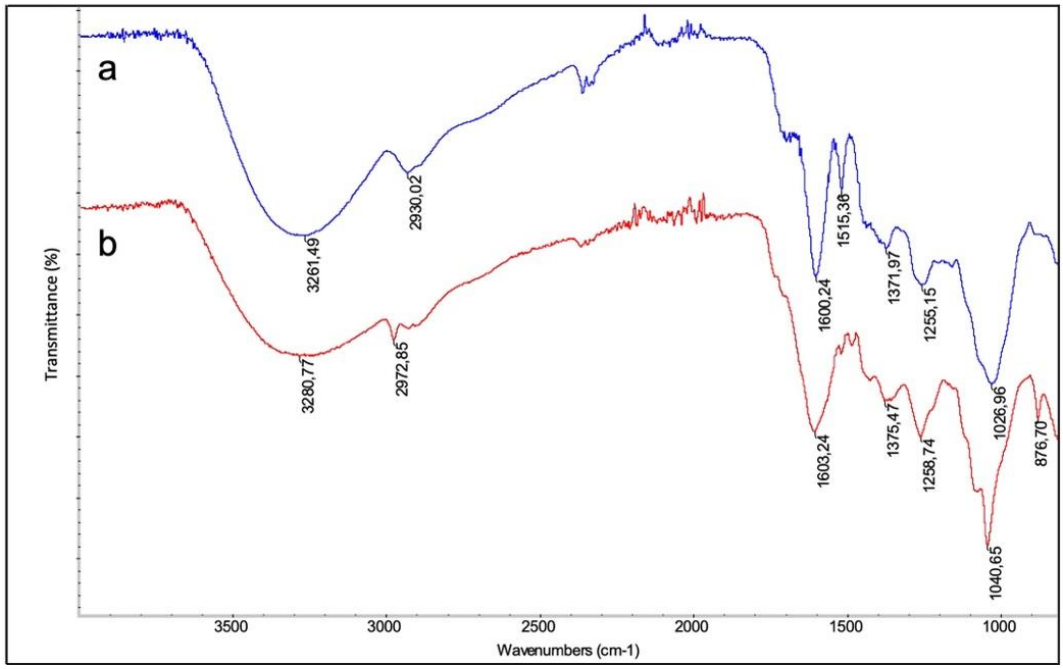

Figure 3.2. FT-IR spectra of (a) *Prunus serrulata* leaf extract in H_2O and (b) the synthesized Fe_3O_4 nanoparticles.

The FT-IR spectroscopy analysis of the *Prunus serrulata* leaf extract in H_2O and the Fe_3O_4 nanoparticles is presented in Figure 3.2 to understand the molecular interactions of the phytochemicals. The FT-IR peaks of *Prunus serrulata* leaf extract in H_2O (Figure 3.2a) and Fe_3O_4 nanoparticles (Figure 3.2b) show similarities. There is a slight shifting in all peaks which may be caused after the nanoparticle synthesis. The data were fitted according to a study [65]. The broad peaks at 3261 cm^{-1} and 3280 cm^{-1} corresponded to O-H stretching. The peaks at 1600 cm^{-1} and 1603 cm^{-1} can be attributed to C=C stretching in the aromatic ring. The low signal peaks at 1371 cm^{-1}, 1375 cm^{-1}, 1255 cm^{-1}, and 1258 cm^{-1} can be

explained by the bending of the C-H vibrations in the inner plane of the aromatic ring. The strong peaks at 1026 cm^{-1} and 1040 cm^{-1} correspond to C-O-C stretching, aromatic ether. Lastly, the peak at 876 cm^{-1} represents the C-H vibrations in the outer plane of the aromatic ring.

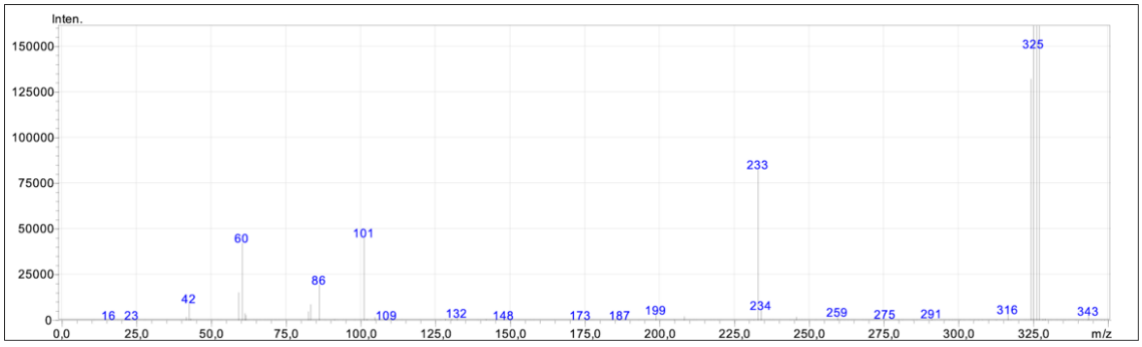

Figure 3.3. LC-MS spectrum of the *Prunus serrulata* leaf extract in H_2O after the synthesis of Fe_3O_4 nanoparticles.

Analysis of the LC-MS spectrum in Figure 3.3 revealed molecular ions and fragments similar to those of quercetin. According to the database numbers FIO00275, CE000169, and PB004085 from the MassBank [66], the unknown flavonoid which is dissolved from the outer shell of the stabilized Fe_3O_4 nanoparticles exhibited characteristic fragments that could be attributed to the quercetin molecule in Figure 3.3. The strong characteristic fragment observed at m/z 325 highly suggests that the most abundant fragment should be quercetin since it has m/z 302 in the $[M+Na]^+$ mode. Additionally, the presence of various fragmentations, such as m/z at 233, 259, 275, and 291 supports the idea that the flavonoid should be quercetin as these fragments have been found in similar studies [67–69].

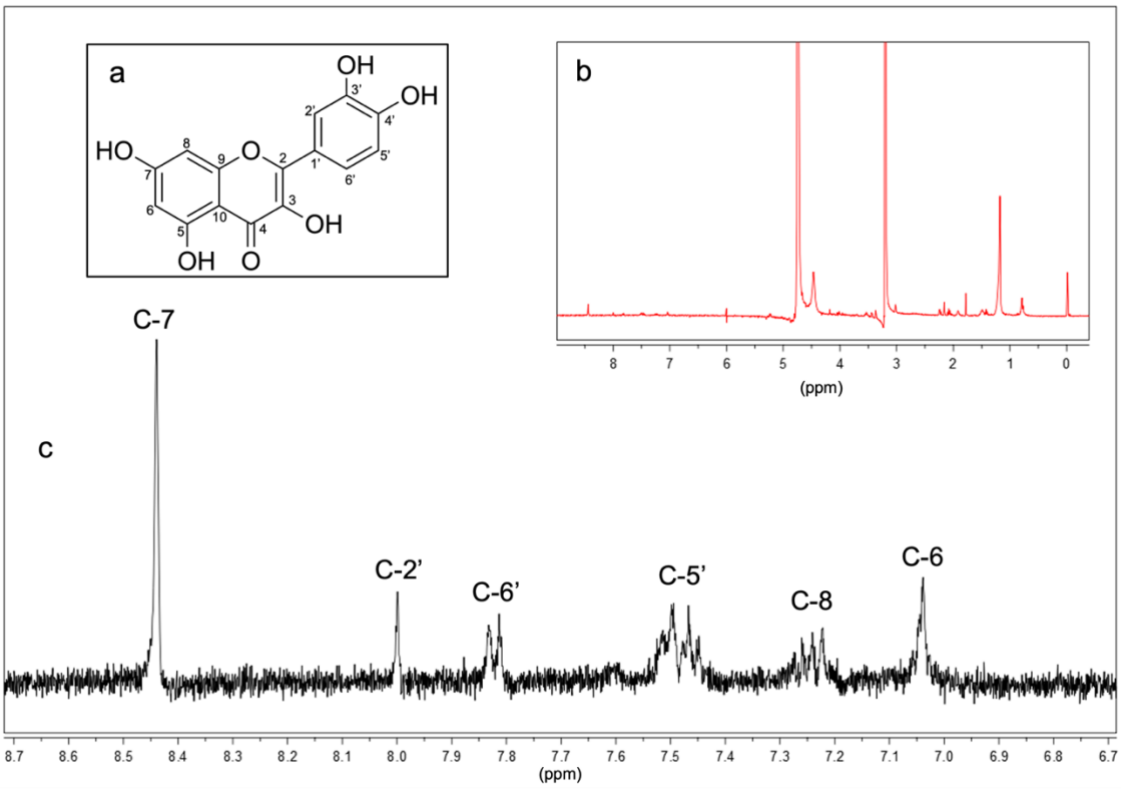

Figure 3.4. The structure of quercetin, (b) the full ^{1}H-NMR spectrum of the quercetin dissolved from Fe_3O_4 nanoparticles, and (c) the enhanced spectrum of the same solution from 6.7 ppm to 8.7 ppm.

The proton NMR (^{1}H-NMR) analysis is required to confirm that the isolated flavonoid dissolved from the stabilized nanoparticles was quercetin. Figure 3.4 displays the structure of quercetin and the ^{1}H-NMR spectra of the molecule derived from the nanoparticles. The structure of quercetin was demonstrated in Figure 3.4a. The numbers were given to each C atom in the structure. The dominant signals in the full spectrum from at 3.3 ppm and 4.9 ppm were methanol-d4 (CD_3OD) peaks in Figure 3.4b. The 6 characteristic signals were assigned to quercetin signals in enhanced spectrum in Figure 3.4c as follows: H on C-6 (s) at 7.05 ppm, H on C-8 (s) at 7.25 ppm, H on C-5' (d) at 7.5 ppm, H on C-6' (d) at 7.8 ppm, H on C-2' (d) at 8.0 ppm, and H of OH on C-7 (s) at 8.45 ppm.

The data on the ^{1}H-NMR spectrum of quercetin in CD_3OD is limited in the literature. Most of the data was found as the quercetin was dissolved in deuterated dimethyl sulfoxide (DMSO-d6) [70]. Therefore, chemical shifting in DMSO-d6, 2.5 ppm, and in CD_3OD, 3.3

ppm, was considered to compare the results in this study with other research findings. The Human Metabolome Database (HMDB) is an open-source data bank that has various data on metabolites in a high number of research with several instrumental techniques such as NMR, LC-MS, and Gas Chromatography-Mass Spectrometry (GC-MS) [71]. This database was used to identify quercetin signals in the NMR spectra. The data was analyzed after the difference between DMSO-d6 and CD_3OD was compensated by subtracting 2.5 ppm from 3.3 ppm. According to HMDB: 166371 and HMDB: 166675, 6 signals were detected for the quercetin protons, and all of them had low intensities due to the dissolved molecule having a trace amount.

The ^{1}H-NMR spectra of *Prunus serrulata* leaf extracts in acetonitrile-d3 (CD_3CN), CD_3OD, and deuterium oxide (D_2O) were presented in Figure A.1, Figure A.2, and Figure A.3, respectively. The graphics are almost impossible to interpret due to the several types of phytochemical contents. Therefore, the present study focused on which specific type of flavonoid was obtained from the nanoparticles.

3.2. Characterization of Iron Oxide Nanoparticles

The synthesis of Fe_3O_4 nanoparticles is controlled by a variety of factors. A comprehensive analysis for the synthesis of Fe_3O_4 nanoparticles was designed and performed to attain a specific morphology within the desired size range. Factors such as the mixing ratio of Fe^{+3} solution to leaf extract, the concentration of Fe^{+3} solution, pH, and reaction temperature were examined to comprehend their impacts on the synthesis of Fe_3O_4 nanoparticles.

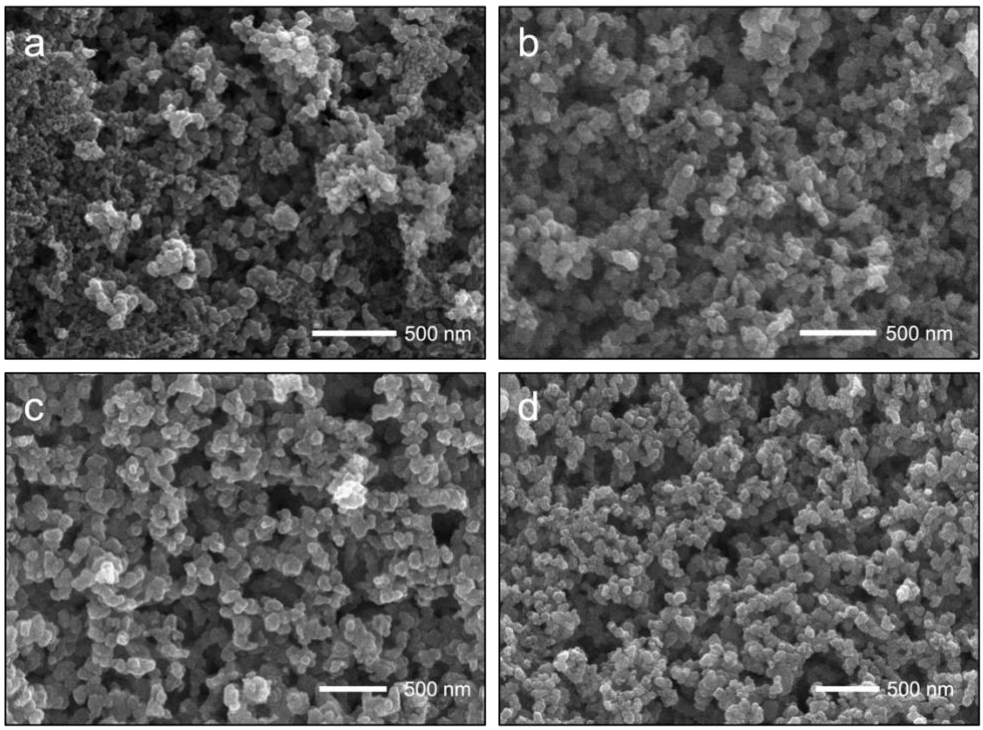

Figure 3.5. The SEM images of Fe_3O_4 nanoparticles synthesized in (a) a 3:1 ratio, (b) a 2:1 ratio, (c) a 1:1 ratio, and (d) a 1:2 ratio.

The impact of the mixing ratio of the volume of Fe^{+3} solution and the volume of leaf extract on the synthesis of Fe_3O_4 nanoparticles was observed by maintaining other factors constant while changing the mixing ratio of the volume of Fe^{+3} solution to the leaf extract. Figure 3.5. shows the SEM images of Fe_3O_4 nanoparticles synthesized in four different volume ratios. All ratios were expressed as metal ion solution:leaf extract.

The SEM image of Fe_3O_4 nanoparticles synthesized in a 3:1 ratio is shown in Figure 3.5a. The nanoparticles were produced due to the strong steric interaction between the metal ions and phytochemicals in the leaf extract. The nanoparticles were separated and displayed cavities. They were uniform, spherical, and approximately ranged in size from 35 nm to 50 nm.

Figure 3.5b shows the SEM image of Fe_3O_4 nanoparticles synthesized in a 2:1 ratio. The nanoparticles are more distinct and separated compared to those shown in Figure 3.5a. They ranged in size from 40 nm to 52 nm. Additionally, the Fe_3O_4 nanoparticles synthesized in a 1:1 ratio, as seen in Figure 3.5c, and a 1:2 ratio, as seen in Figure 3.5d, also have similar

SEM images indicating that adequate bioorganic molecules interacted with the metal ions, and the reaction was completed without further increase in size with no agglomeration.

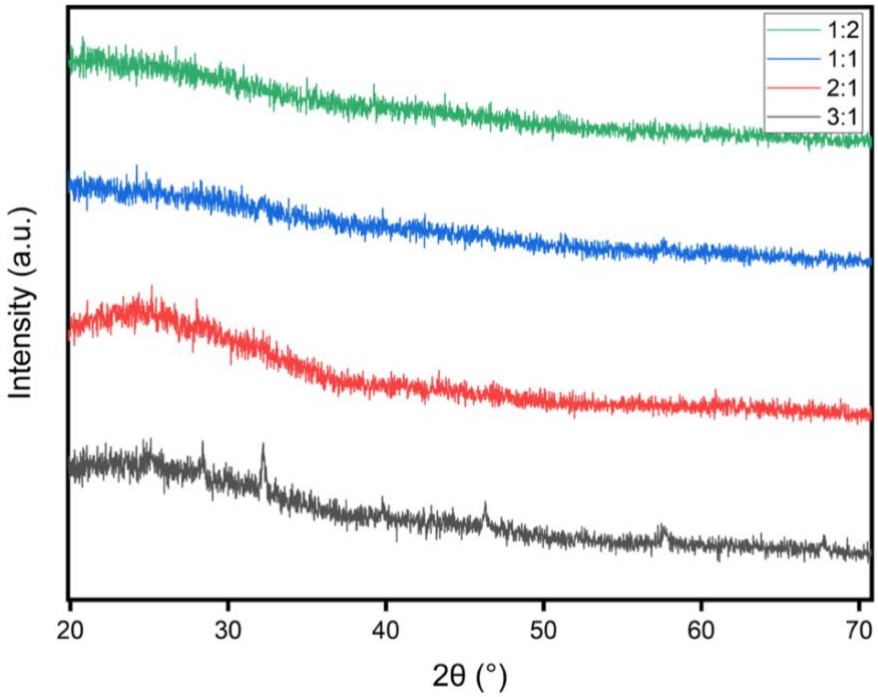

Figure 3.6. The XRD pattern of Fe_3O_4 nanoparticles synthesized in four different volume ratios.

The XRD pattern of Fe_3O_4 nanoparticles synthesized in four different volume ratios is shown in Figure 3.6. The XRD peak of Fe_3O_4 nanoparticles synthesized in a 3:1 ratio has slightly sharper peaks at 2θ=29°, 33°, 40°, 46°, and 58°, distinguishing it from the XRD peaks of Fe_3O_4 nanoparticles synthesized in the other mixing ratios. The XRD peak of Fe_3O_4 nanoparticles synthesized in a 2:1 ratio has a slight bump at 2θ=25° caused by the phytochemicals from the leaf extract. The other ratios, 1:1 and 1:2, did not show any distinctive peaks at any 2θ, stating that X-rays were not collected from the surface of the nanoparticles at all. Overall, all Fe_3O_4 nanoparticles were amorphous, but only the nanoparticles synthesized in a 3:1 mixing ratio showed slight crystalline properties. Therefore, the optimum condition for the impact of the mixing ratio of the Fe^{+3} solution and the leaf extract on the synthesis of Fe_3O_4 nanoparticles was determined as a 3:1 ratio.

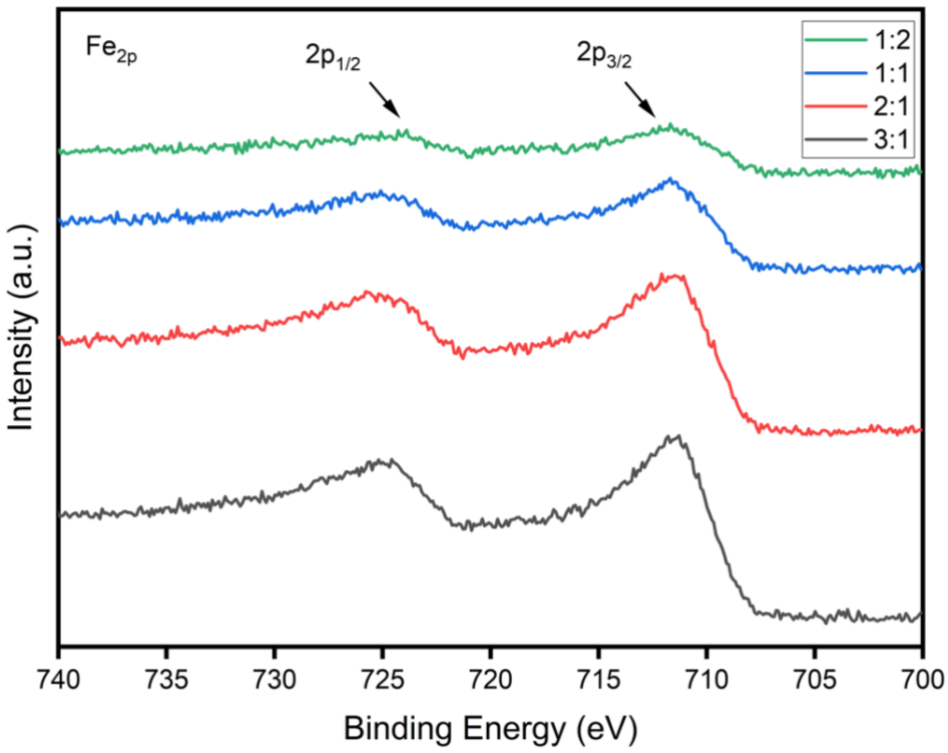

Figure 3.7. The XPS spectra for the comparison of Fe_{2p} of Fe_3O_4 nanoparticles synthesized in four different volume ratios.

The XPS spectra for the comparison of Fe_{2p} of Fe_3O_4 nanoparticles synthesized in four different volume ratios are shown in Figure 3.7. Each spectrum has characteristic peaks for $2p_{1/2}$ and $2p_{3/2}$ profiles at 725 eV and 710.8 eV, respectively. However, Fe_3O_4 nanoparticles synthesized in both a 1:1 ratio and a 1:2 ratio have broader peaks compared to those synthesized in both a 3:1 ratio and a 2:1 ratio. The presence of an excess amount of bioorganic surface-active molecules and the amorphous structure of Fe_3O_4 nanoparticles contribute to this broadening. Therefore, considering the results of SEM, XRD, and XPS together, the optimum mixing ratio between Fe^{+3} solution and the leaf extract was determined as a 3:1 ratio.

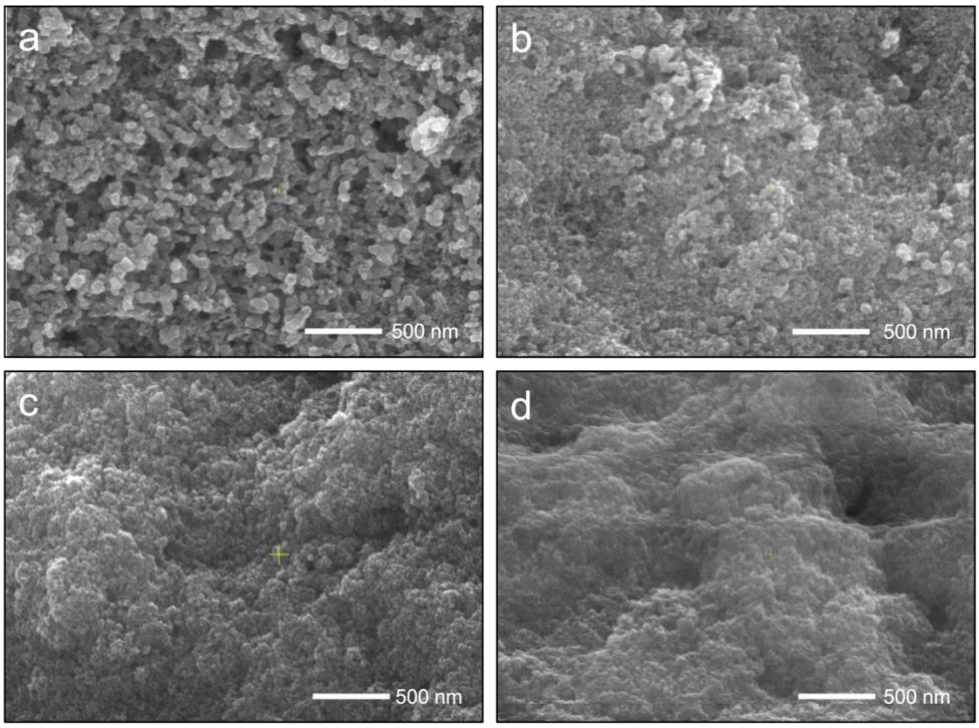

Figure 3.8. The SEM images of Fe_3O_4 nanoparticles synthesized with (a) 10 mM, (b) 25 mM, (c) 50 mM, and (d) 75 mM $FeCl_3$.

The effect of the concentration of Fe^{+3} solution on the synthesis of Fe_3O_4 nanoparticles was monitored by maintaining other factors constant while changing the concentration of the Fe^{+3} solution. Figure 3.8. represents the SEM images of Fe_3O_4 nanoparticles synthesized with four different concentrations of $FeCl_3$.

Figure 3.8a is easily distinguished from Figure 3.8b, c and d. It shows more distinct and separated nanoparticles with uniform and spherical shapes. They are approximately ranged in size from 40 nm to 50 nm. Figure 3.8b indicates that nanoparticles produced with 25 mM Fe^{+3} solution have slightly observable but not as much as those nanoparticles produced with 10 mM Fe^{+3} solution. On the other hand, the steric interaction between phytochemicals from the leaf extract and Fe^{+3} ions is not strong enough at higher concentrations of 50 mM and 75 mM Fe^{+3} solution as it is in the lower concentrations in Figure 3.8c and d. Hence, this causes bulky material to form instead of nanoparticles.

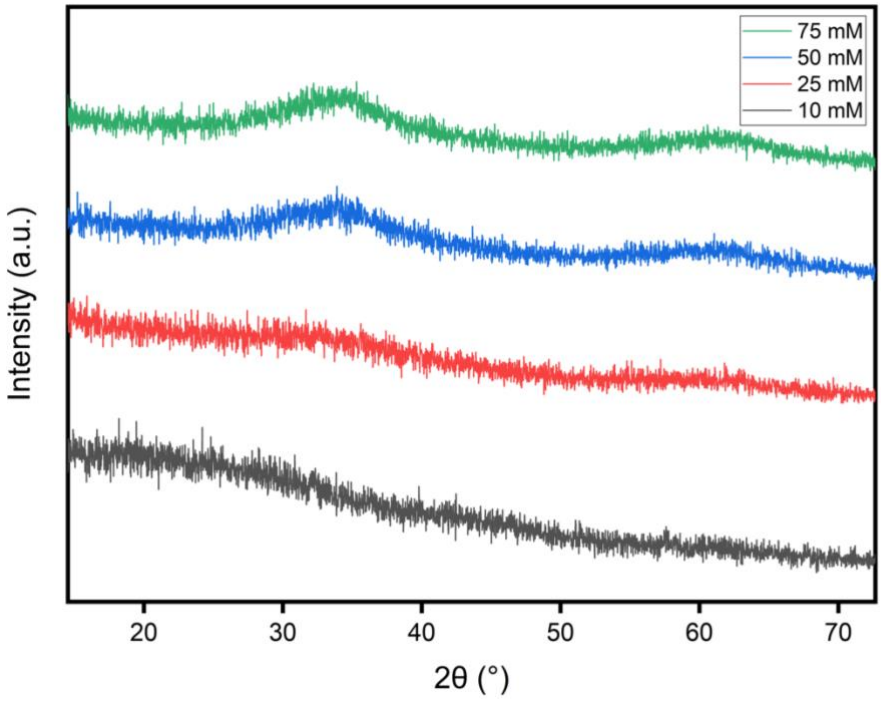

Figure 3.9. The XRD pattern of Fe_3O_4 nanoparticles synthesized with four different concentrations.

The XRD pattern of Fe_3O_4 nanoparticles synthesized with four different concentrations is represented in Figure 3.9. The XRD peaks of Fe_3O_4 nanoparticles synthesized with both 10 mM and 25 mM Fe^{+3} solutions have similarities. However, they differ in that they both have broader peaks compared to the XRD peaks of Fe_3O_4 nanoparticles synthesized in both 50 mM and 75 mM Fe^{+3} solutions. Moreover, Fe_3O_4 nanoparticles synthesized with both 50 mM and 75 mM Fe^{+3} solutions have slightly sharper peaks that can be attributed to the characteristic peaks of Fe_3O_4 nanoparticles at $2\theta = 35°$ and at $2\theta = 62°$ indicating that the crystalline structure is relatively stronger compared to Fe_3O_4 nanoparticles synthesized with both 10 mM and 25 mM Fe^{+3} solutions which are obviously amorphous. This is due to samples with low signal-to-noise ratios and poor crystalline structures produce XRD patterns with broadened peaks, and they do not have significant XRD peaks [72]. Thus, it was not expected to have strong crystalline structures in these results.

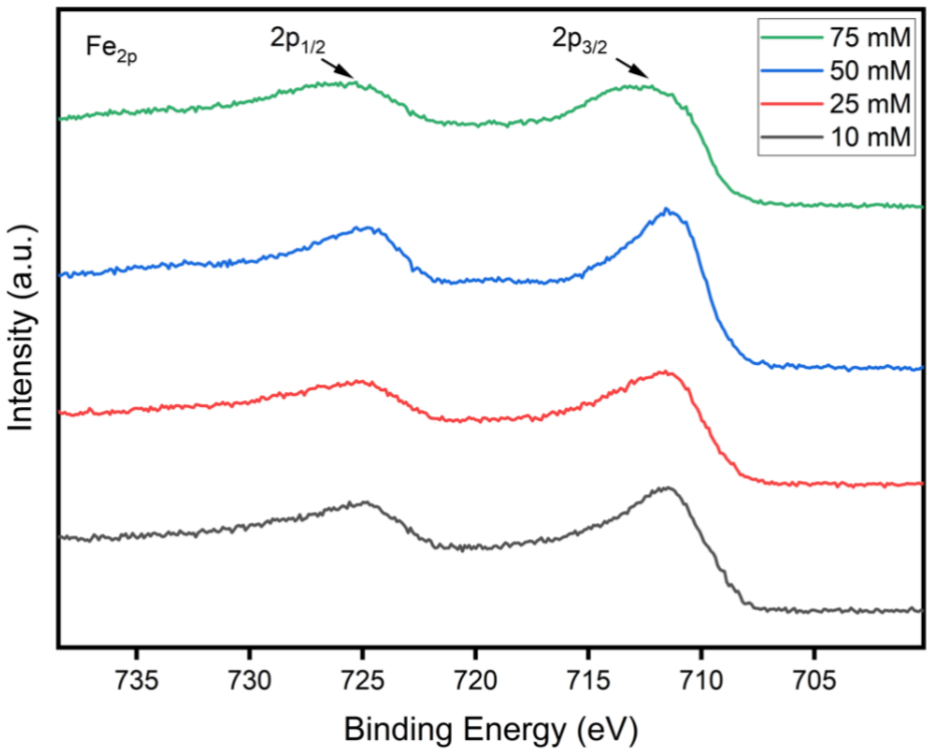

Figure 3.10. The XPS spectra for the comparison of Fe_{2p} of Fe_3O_4 nanoparticles synthesized with four different concentrations.

Figure 3.10 compares the $2p_{1/2}$ and $2p_{3/2}$ profiles of the Fe_{2p} for the XPS analysis with four different concentrations. The XPS spectra demonstrate the same characteristic peaks at 725 eV and 710.8 eV for all concentration values, respectively. The spectra of 10 mM, 25 mM, and 50 mM Fe^{+3} solutions have sharper peaks whereas the spectrum of 75 mM Fe^{+3} solution has lightly broader bumps at the top of the curves. The 50 mM spectrum has a small satellite between 721 eV and 715 eV suggesting that Fe_2O_3 could be formed [73]. This could be caused by different molecular interactions or molecular orientations between Fe^{+3} ions and bioorganic molecules from the leaf extract during the reaction. The 75 mM spectrum has broader bumps due to the higher concentration of Fe^{+3} solution which inhibits the formation of strong bonding between surfactants and metal ions in the reaction and causes failure to stabilize the production of nanoparticles.

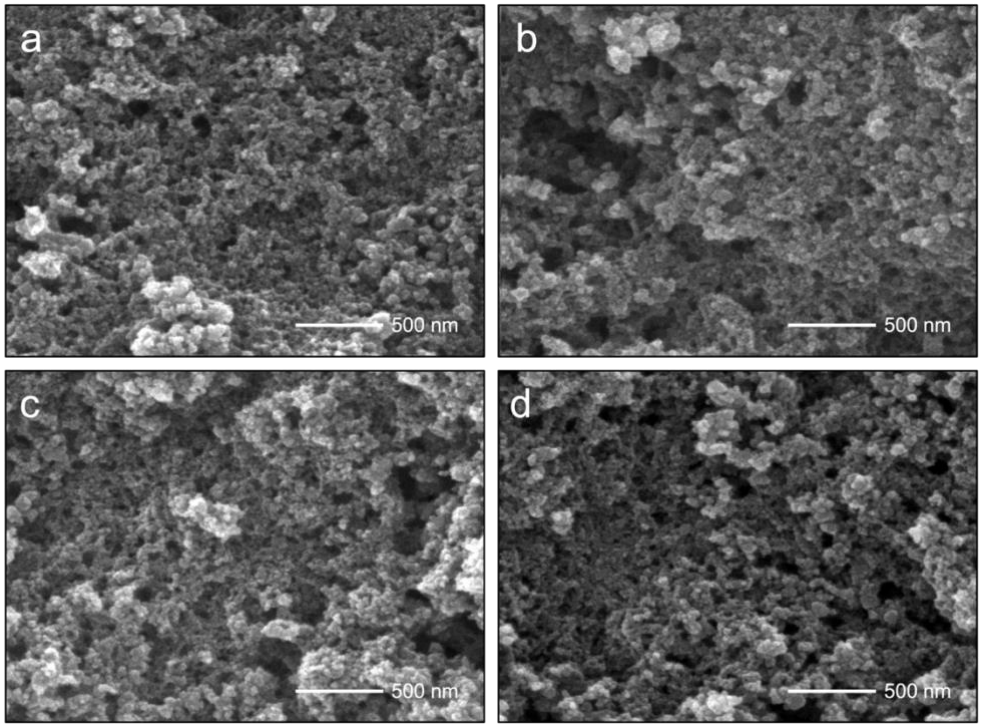

Figure 3.11. The SEM images of Fe_3O_4 nanoparticles synthesized by adjusting the pH values to (a) 4, (b) 6, (c) 8, and (d) 10.

The effect of the pH of the solution on the synthesis of Fe_3O_4 nanoparticles was studied by maintaining other factors constant while adjusting the pH of the solution. Figure 3.11 represents the SEM images of Fe_3O_4 nanoparticles synthesized by adjusting the pH values.

The effect of different pH values (4, 6, 8, and 10) on the synthesis of Fe_3O_4 nanoparticles was investigated. The morphology of Fe_3O_4 nanoparticles is similar without any noticeable difference in the SEM images shown in Figure 3.11a-d. The SEM images showed that the Fe_3O_4 nanoparticles were uniform and homogenous in all samples. All synthesized Fe_3O_4 nanoparticles had a spherical shape, and the size distribution was similar in all samples. Additionally, the average size of the nanoparticles was approximately 40 nm.

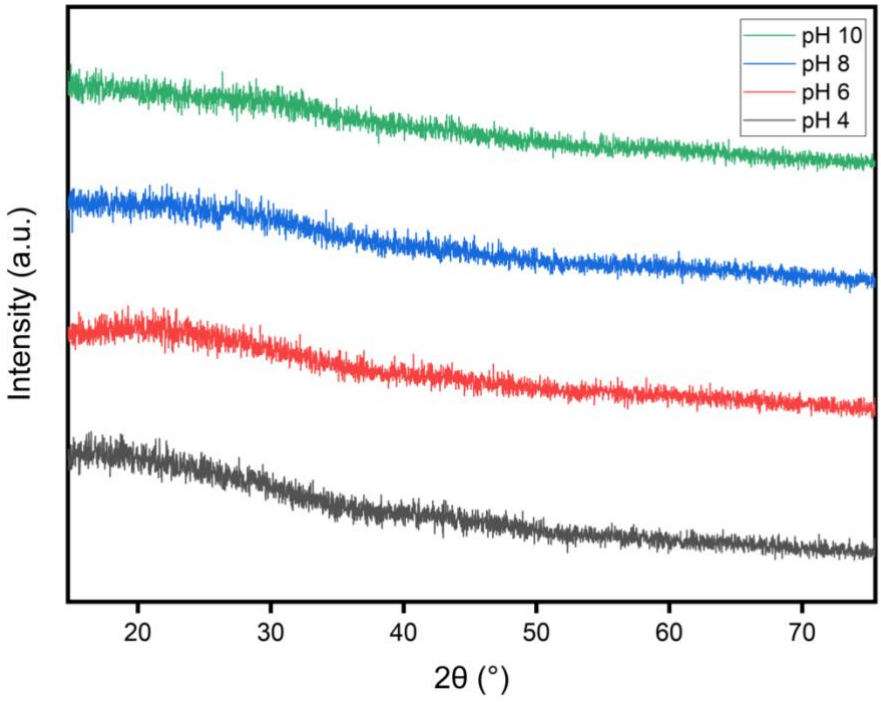

Figure 3.12. The XRD pattern of Fe_3O_4 nanoparticles synthesized at the four different pH values.

The XRD pattern for Fe_3O_4 nanoparticles synthesized at the different pH values is displayed in Figure 3.12. A bump is observed at $2\theta = 20°$ for pH 4 and pH 6 values. However, the XRD pattern does not show any clear characteristic peaks that can be attributed to the Fe_3O_4 nanoparticles. This means that the synthesized Fe_3O_4 nanoparticles have an amorphous crystalline structure. There is similar research suggesting that the deficiency of diffraction peaks corresponds to impurities or oxides from the bioorganic molecules of the leaf extract [74].

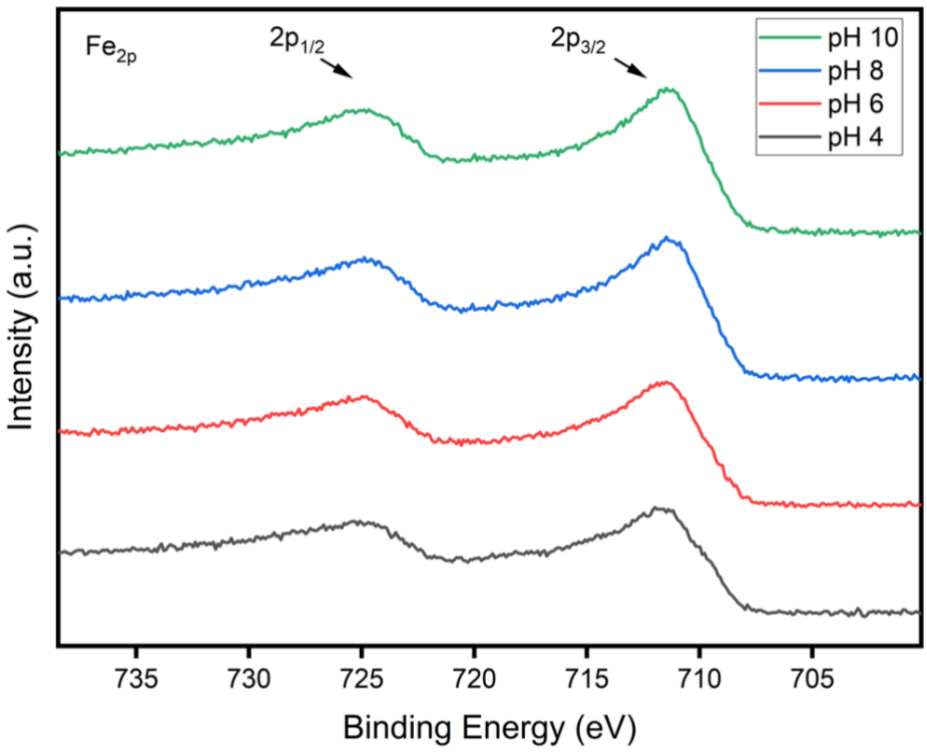

Figure 3.13. The XPS spectra of Fe_3O_4 nanoparticles synthesized at the four different pH values.

The XPS results for the $2p_{1/2}$ and $2p_{3/2}$ profiles of the Fe_{2p} peak comparison of Fe_3O_4 nanoparticles synthesized at the four different pH values is shown in Figure 3.13. The XPS spectra indicate the same characteristic peaks at 725 eV and 710.8 eV for all pH values. There is no observable satellite peak between the $2p_{1/2}$ and $2p_{3/2}$ profiles which suggests that the Fe_3O_4 nanoparticles synthesized at the four different pH values are considered to be in Fe_3O_4 form according to a similar study [73]. Overall, there is no significant effect on the morphology and crystalline structure of the synthesized Fe_3O_4 nanoparticles.

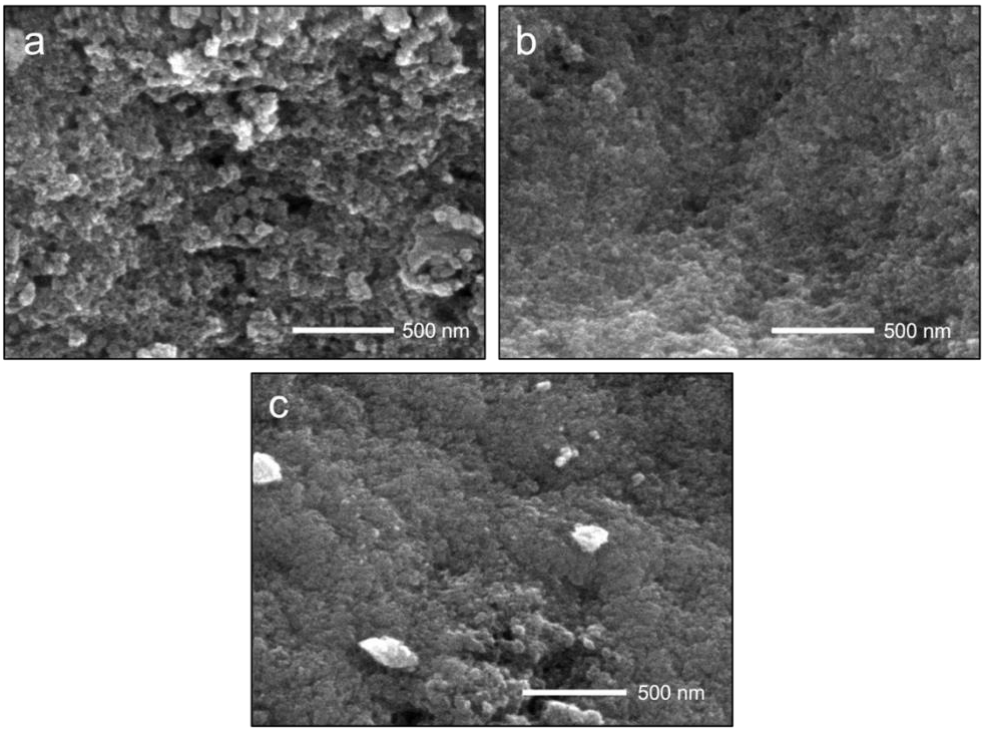

Figure 3.14. The SEM images of Fe_3O_4 nanoparticles synthesized at (a) 25 °C, (b) 45 °C, and (c) 65 °C.

The impact of the temperature of the reaction on the synthesis of Fe_3O_4 nanoparticles was studied by maintaining other factors constant while adjusting the temperature of the reaction. Figure 3.14. shows the SEM images of Fe_3O_4 nanoparticles synthesized at different temperatures.

Figure 3.14a showed that the Fe_3O_4 nanoparticles synthesized at 25 °C were visibly different and had a relatively uniform appearance. Their average size is between 30 nm and 50 nm. However, the Fe_3O_4 nanoparticles synthesized at 45 °C were less distinct than the Fe_3O_4 nanoparticles synthesized at 25 °C in Figure 3.14b. In Figure 3.14c, the Fe_3O_4 nanoparticles synthesized at 65 °C are slightly larger and more aggregated than the Fe_3O_4 nanoparticles synthesized at lower temperatures. Their size distribution is less uniform. It was expected that changing the temperature in the synthesis process could alter the size of the synthesized Fe_3O_4 nanoparticles by increasing the kinetic energy of Fe^{+3} ions and bioactive materials. However, only the synthesized Fe_3O_4 nanoparticles synthesized at 65 °C indicated some aggregation meaning that increasing the temperature during nanoparticle synthesis has no significant effect on the morphology of Fe_3O_4 nanoparticles.

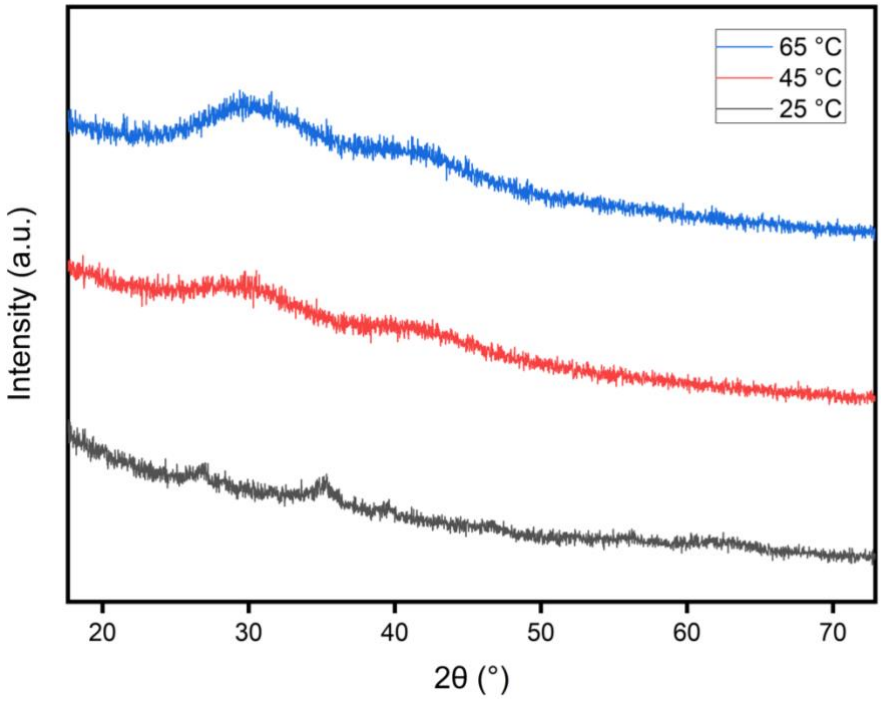

Figure 3.15. The XRD pattern of Fe_3O_4 nanoparticles synthesized at three different temperatures.

The XRD pattern of Fe_3O_4 nanoparticles synthesized at three different temperatures is shown in Figure 3.15. The XRD peaks of Fe_3O_4 nanoparticles synthesized at 45 °C and 65 °C present similar patterns. The only difference is that Fe_3O_4 nanoparticles synthesized at 25 °C have slightly sharper peaks at 2θ=28°, 36°, and 62° suggesting relatively stronger crystalline structure than the Fe_3O_4 nanoparticles synthesized at other temperatures. Therefore, 25 °C temperature was determined as an optimum parameter in the synthesis of Fe_3O_4 nanoparticles.

After analyzing the effects of the mixing ratio, concentration, pH, and temperature on the synthesis of Fe_3O_4 nanoparticles the optimum combination of these parameters was determined to be a 3:1 mixing ratio, 10 mM $FeCl_3$ solution, pH 6, and a reaction temperature of 25 °C. The FT-IR, EDX, STEM, and detailed XPS analysis were conducted to further characterize the optimal conditions.

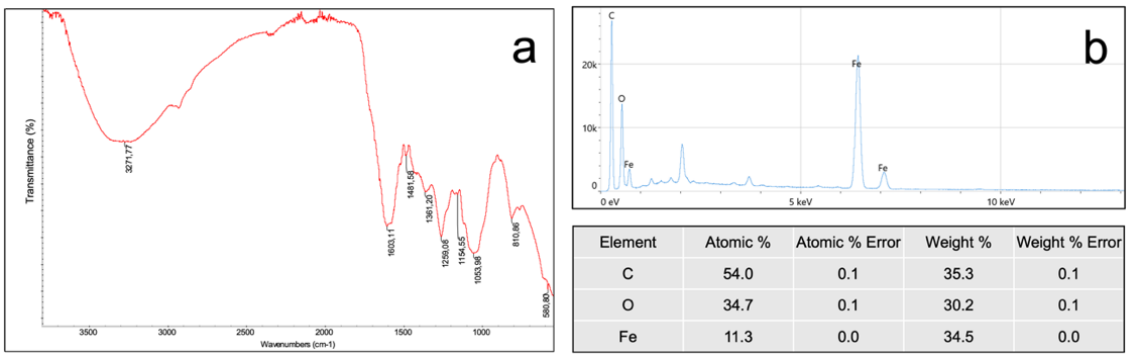

Element	Atomic %	Atomic % Error	Weight %	Weight % Error
C	54.0	0.1	35.3	0.1
O	34.7	0.1	30.2	0.1
Fe	11.3	0.0	34.5	0.0

Figure 3.16. The (a) FT-IR spectroscopy and (b) EDX spectrum of the Fe_3O_4 nanoparticles with *Prunus serrulata* leaf extract under the optimum conditions.

The FT-IR spectroscopy and EDX spectrum of the Fe_3O_4 nanoparticles synthesized under the optimum conditions are presented in Figure 3.16. The FT-IR spectroscopy in Figure 3.16a is similar to the FT-IR spectra obtained from the leaf extract, indicating the same flavonoid is found around the Fe_3O_4 nanoparticles. Additionally, the EDX spectrum of the Fe_3O_4 nanoparticles synthesized under the optimum conditions is presented in Figure 3.16b. The elemental composition of the Fe_3O_4 nanoparticles includes C, mostly from the phytochemicals around the metal, Fe, and O elements. The atomic percentages of these elements with C at 54%, O at 34.7%, and Fe at 11.3 % indicate that the Fe percentage in the synthesized Fe_3O_4 nanoparticles is relatively low.

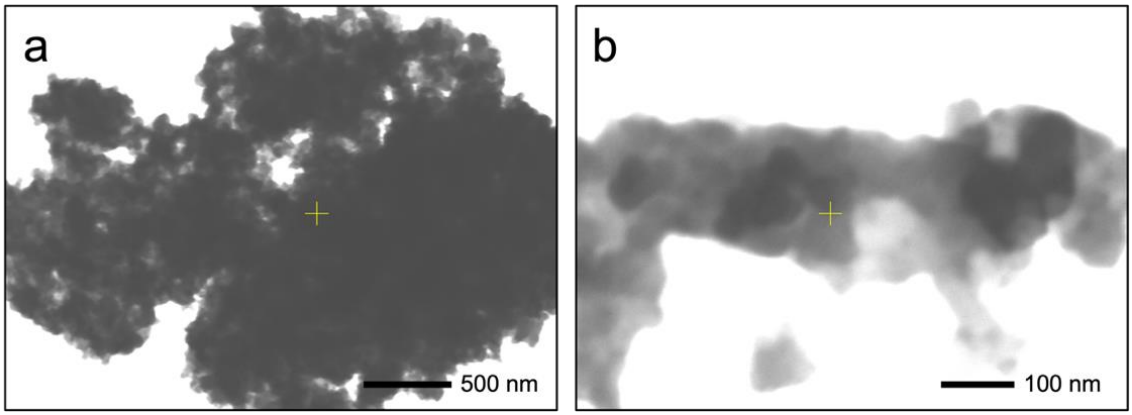

Figure 3.17. The STEM images of the Fe_3O_4 nanoparticles synthesized under the optimum conditions from two different scales: (a) 500 nm and (b) 100 nm.

The STEM images of the Fe_3O_4 nanoparticles synthesized under the optimum conditions are represented in Figure 3.17. The Fe_3O_4 nanoparticles were observed at a scale of 500 nm in Figure 3.17a and at a scale of 100 nm in Figure 3.17b. The contrast between the darker inner sphere and the lighter or gray outer sphere indicates that the Fe_3O_4 nanoparticles synthesized under the optimum conditions are spherical and covered with organic molecules. The sizes of the Fe_3O_4 nanoparticles are ranged between 30 nm to 60 nm. The STEM images were obtained by partially dissolving the solid Fe_3O_4 nanoparticles in water first, then evaporating them on the copper grid. Therefore, aggregation is observed due to the reformation of nanoparticles. This phenomenon helped to explain the results obtained from the XRD, XPS, and EDX analyses.

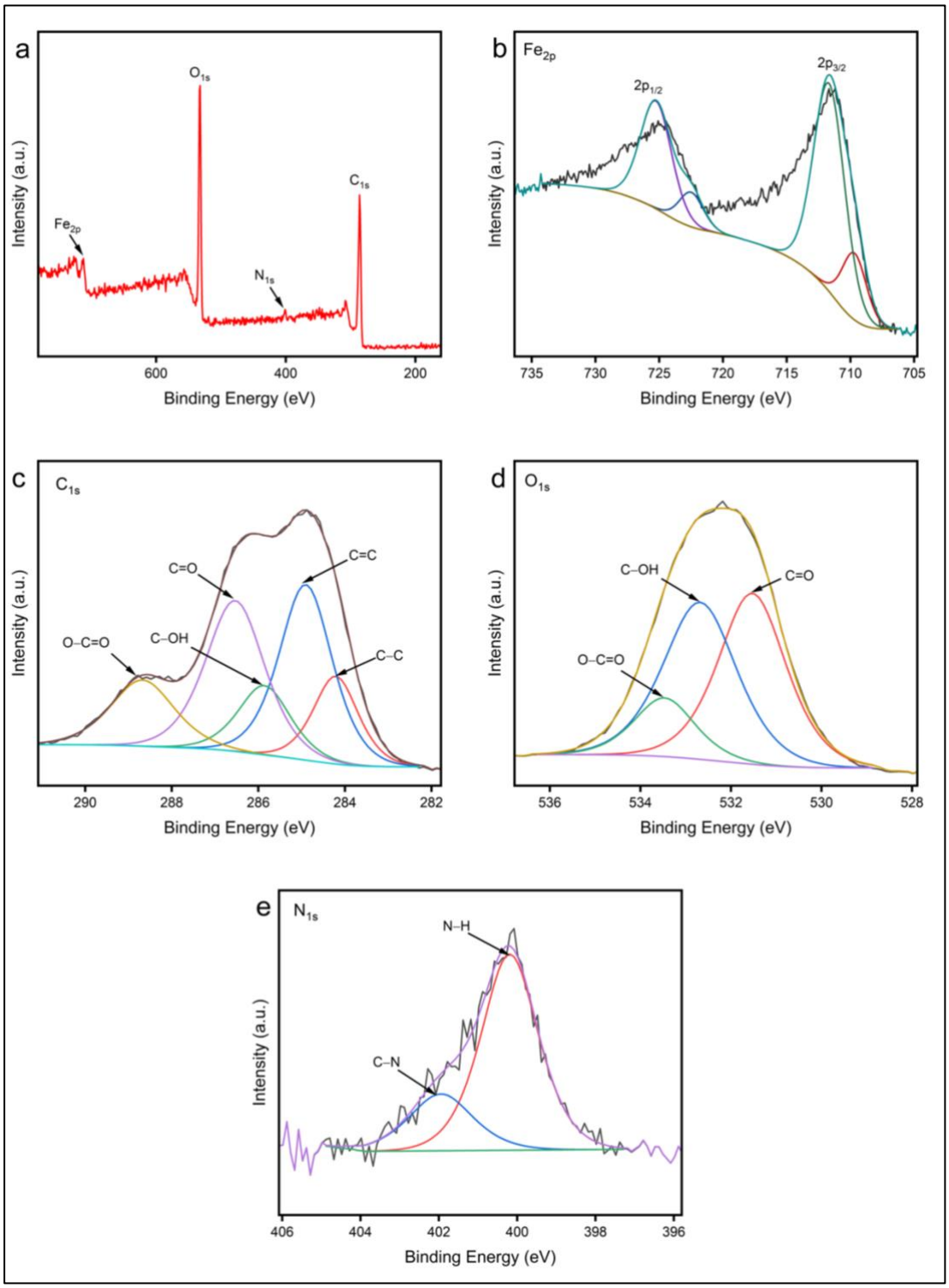

Figure 3.18. The XPS spectra of the Fe_3O_4 nanoparticles synthesized using *Prunus serrulata* leaf extract under the optimum conditions including the (a) survey and (b) Fe_{2p} (c), C_{1s}, (d) O_{1s}, and (e) N_{1s} profiles of the Fe_3O_4 nanoparticles.

The XPS results of the Fe_3O_4 nanoparticles synthesized under the optimum conditions are shown in Figure 3.18. The XPS survey in Figure 3.18a showed the presence of Fe, O, C, and N elements on the surface of Fe_3O_4 nanoparticles. The Fe_{2p} profile in Figure 3.18b displayed several characteristic peaks of $2p_{1/2}$ and $2p_{3/2}$. The peaks at 709.78 eV and 711.68 eV for $2p_{3/2}$ and 722.48 eV and 725.28 for $2p_{1/2}$ are Fe^{+2} and Fe^{+3} peaks according to similar research [75]. The C_{1s} profile in Figure 3.18c revealed the five characteristic peaks [76]. The C–C peak at 284.28 eV, the C=C peak at 284.88 eV, the C–OH peak at 285.88 eV, the C=O peak at 286.58 eV, and the O–C=O at 288.68 eV were observed. The O_{1s} profile in Figure 3.18d showed three characteristic peaks [76]. The C=O peak at 531.58 eV, the C–OH peak at 532.68 eV, and the O–C=O peak at 533.48 eV were observed. The N_{1s} profile in Figure. 3.13e displayed two characteristic peaks [77]. The N–H peak at 399.98 eV and the C–N peak at 401.88 eV were observed. Overall, the C_{1s}, O_{1s}, and N_{1s} profiles confirmed that the surface of the nanoparticles was in oxide form, whereas the Fe_{2p} profile indicated the presence of Fe^{+2} and Fe^{+3} peaks meaning that it was in the Fe_3O_4 form. The XPS analysis was consistent with the XRD and FT-IR results.

3.3. Characterization of Copper Oxide Nanoparticles

The synthesis of CuO nanoparticles is controlled by a variety of factors. A broad analysis for the synthesis of CuO nanoparticles was designed and performed to attain a specific morphology within the desired size range. Factors such as the mixing ratio of Cu^{+2} solution to leaf extract, the concentration of Cu^{+2} solution, pH, and the reaction temperature were inspected to understand their impacts on the synthesis of CuO nanoparticles.

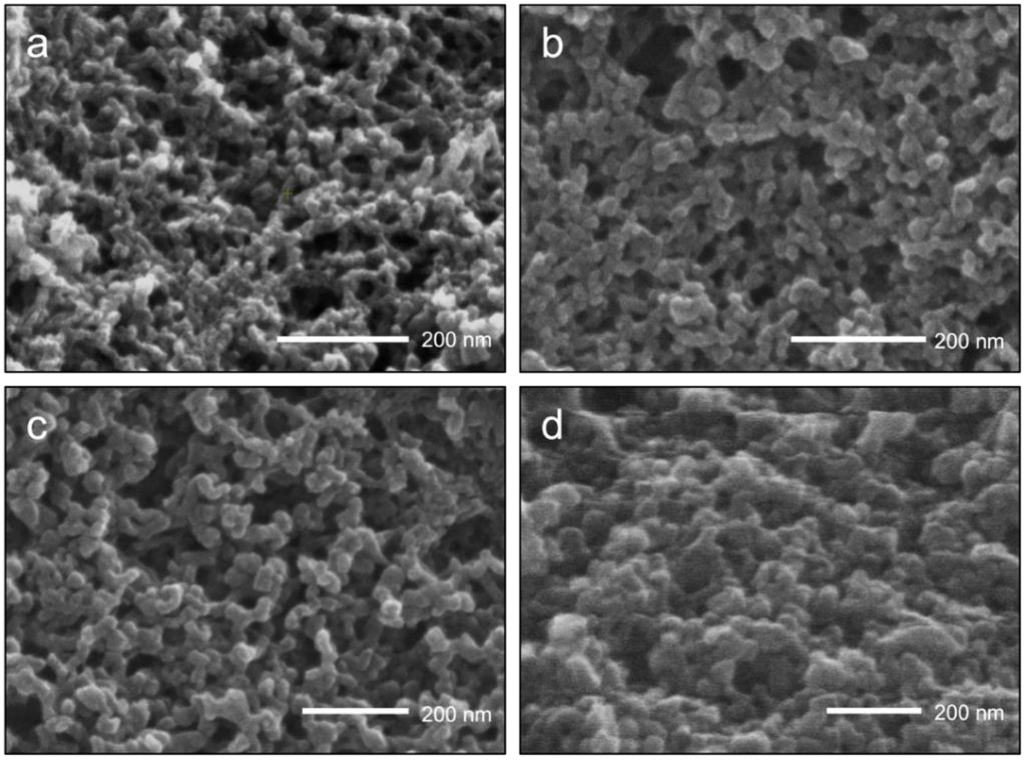

Figure 3.19. The SEM images of CuO nanoparticles synthesized in (a) a 3:1 ratio, (b) a 2:1 ratio, (c) a 1:1 ratio, and (d) a 1:2 ratio.

The impact of the mixing ratio of the volume of Cu^{+2} solution and the leaf extract on the synthesis of CuO nanoparticles was observed by maintaining other factors constant while changing the mixing ratio of the volume of Cu^{+2} solution to the leaf extract. Figure 3.19 shows the SEM images of CuO nanoparticles synthesized in four different volume ratios.

The SEM image of CuO nanoparticles synthesized in a 3:1 ratio is shown in Figure 3.19a. The formation of nanoparticles took place, and the nanoparticles were distinct enough to separate them from each other. Figure 3.19b-c display the SEM images of CuO nanoparticles synthesized in a 2:1 and a 1:1 ratios. The CuO nanoparticles synthesized in a 2:1 and a 1:1 ratios were more distinct than the CuO nanoparticles synthesized in a 3:1 ratio. The CuO nanoparticles synthesized in a 1:2 ratio is slightly aggregated due to the stronger interaction between the leaf extract and Cu+2 ions, hence reaction was completed before reaching the final desired ratio. Overall, the CuO nanoparticles were uniform, distinct, and spherical in shape. They were approximately ranged in size from 15 nm to 25 nm.

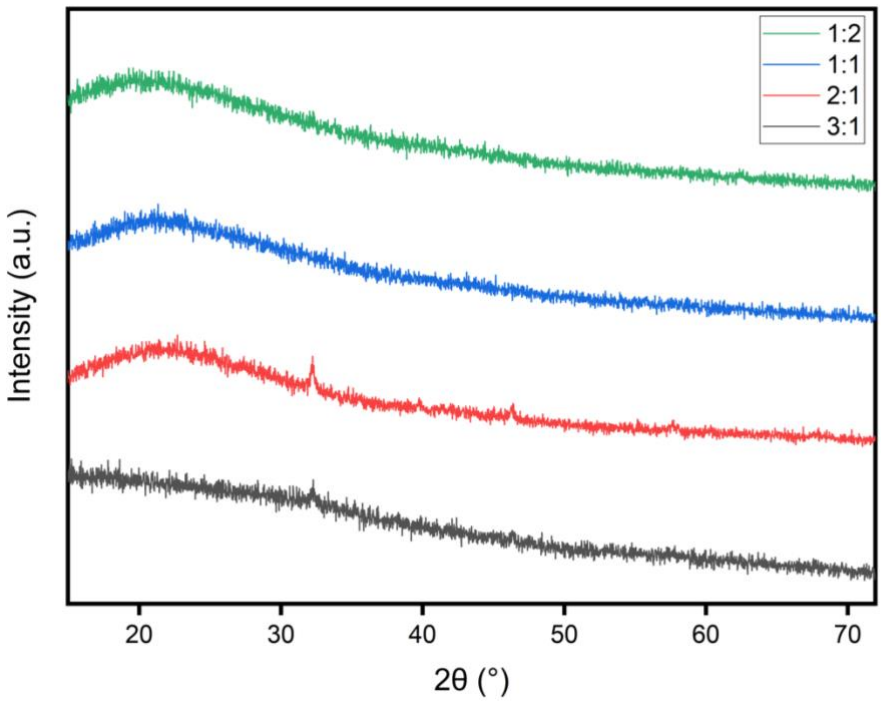

Figure 3.20. The XRD pattern of CuO nanoparticles synthesized in four different volume ratios.

The XRD pattern of CuO nanoparticles synthesized in four different volume ratios is presented in Figure 3.20. The XRD peaks of CuO nanoparticles synthesized in 3:1, 1:1, and 1:2 ratios have similar patterns, with no characteristic peaks observed at any 2θ value. On the other hand, CuO nanoparticles synthesized in a 2:1 ratio presented slight characteristic peaks at 2θ=33°, 45°, and 57°, suggesting the production of CuO nanoparticles. The XRD peaks of CuO nanoparticles synthesized in 1:1 and 1:2 ratios had similar bumps at 2θ=23°, which can be explained by the bioorganic molecules from the leaf extract covered the nanoparticles. Overall, CuO nanoparticles were mostly amorphous, but only the nanoparticles synthesized in a 2:1 ratio showing slight crystalline properties. Therefore, the optimum parameter for the impact of the mixing ratio of the Cu^{+2} solution and the leaf extract on the synthesis of CuO nanoparticles was determined as a 2:1 ratio.

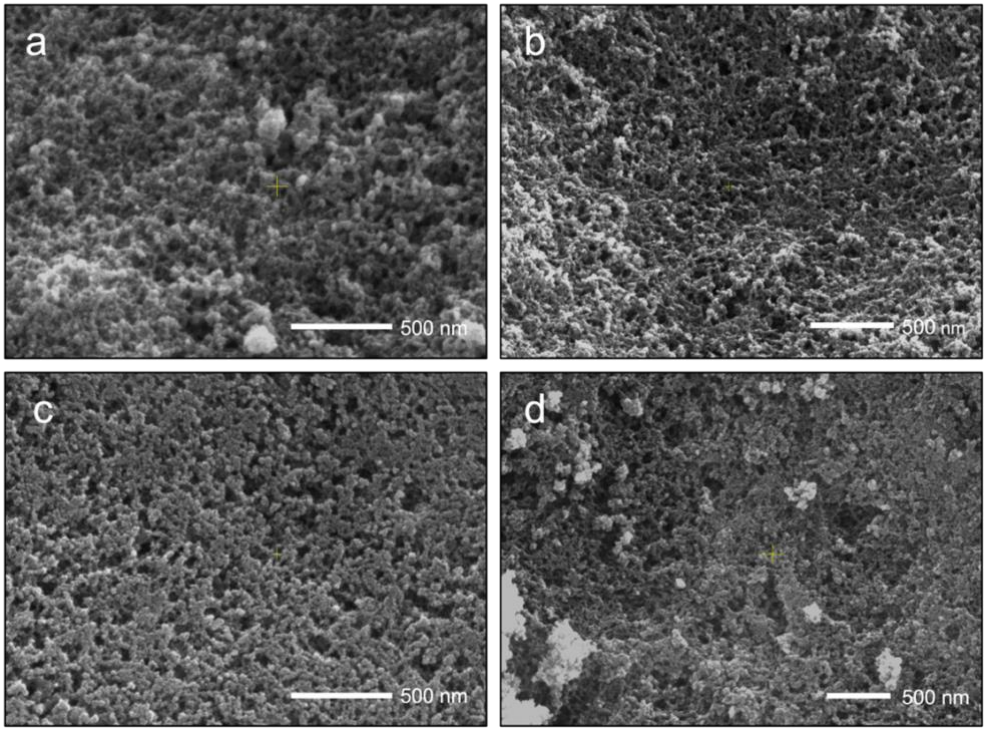

Figure 3.21. The SEM images of CuO nanoparticles synthesized with (a) 10 mM, (b) 25 mM, (c) 50 mM, and (d) 75 mM Cu^{+2} solution.

The effect of the concentration of Cu^{+2} solution on the synthesis of CuO nanoparticles was examined by maintaining other factors constant while changing the concentration of Cu^{+2} solution. Figure 3.21 signifies the SEM images of CuO nanoparticles synthesized with four different concentrations of $CuSO_4.5H_2O$.

Figure 3.21a shows the SEM image of CuO nanoparticles synthesized with a concentration of 10 mM Cu^{+2} solution. The nanoparticles were formed. However, due to the low steric interaction between the phytochemicals from the leaf extract and Cu^{+2} solution, they were not clear and not uniform. On the other hand, the nanoparticles synthesized with a concentration of 25 mM Cu^{+2} solution were more distinct and homogenous in Figure 3.21b, whereas the nanoparticles synthesized with concentrations of 50 mM and 75 mM Cu^{+2} solution were produced but agglomerated in Figure 3.21c and d. The nanoparticles synthesized with concentration of 50 mM Cu^{+2} solution were homogenous in Figure 3.21c. However, they were looked like as they were stabilized layer by layer. Furthermore, the nanoparticles synthesized with concentration of 75 mM Cu^{+2} solution had small mounds even if there were nanoparticles with smaller sizes in Figure 3.21d. Overall, increasing the

concentration of Cu^{+2} solution caused slightly more agglomeration on the synthesis of CuO nanoparticles.

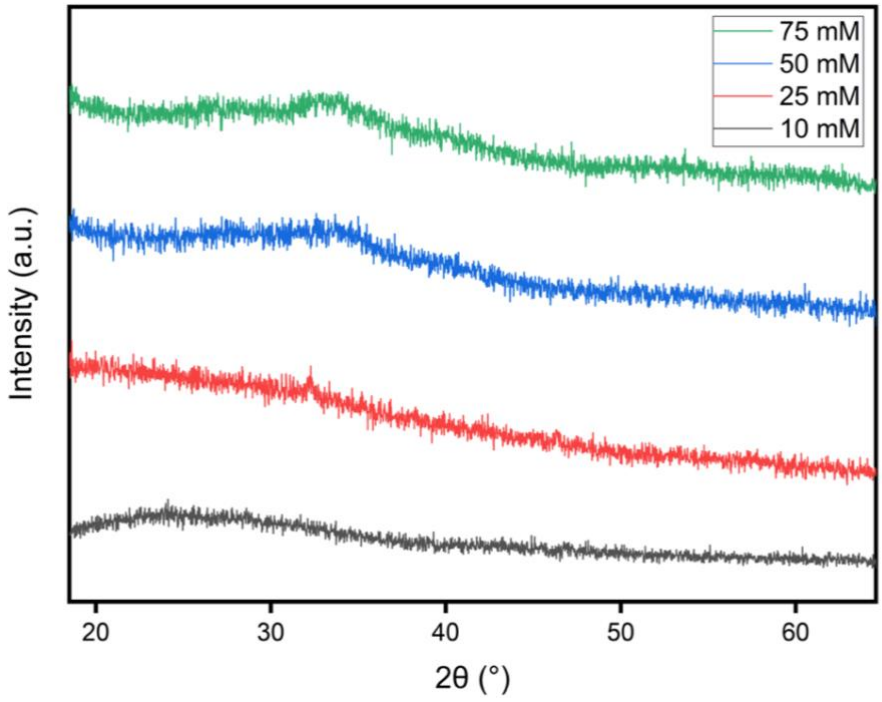

Figure 3.22. The XRD pattern of CuO nanoparticles synthesized with four different concentrations.

The XRD pattern of CuO nanoparticles synthesized with four different concentrations is shown in Figure 3.22. The XRD peaks of CuO nanoparticles synthesized with both 50 mM and 75 mM Cu^{+2} solution have similar peaks. They showed peaks at 2θ=35° and 2θ =54° which can be attributed to the phytochemicals from the leaf extract on the surface of nanoparticles, but they did not include any specific CuO nanoparticles peaks. On the other hand, CuO nanoparticles synthesized with 25 mM Cu^{+2} solution showed tiny characteristic peaks at 2θ=33° and 45° compared to other nanoparticles synthesized with different concentrations, making it more preferable. Moreover, CuO nanoparticles synthesized with 10 mM Cu^{+2} solution showed barely any peak indicating that the nanoparticles had no crystalline peaks. Therefore, the optimum parameter for the synthesis of CuO nanoparticles was determined as a 25 mM Cu^{+2} solution.

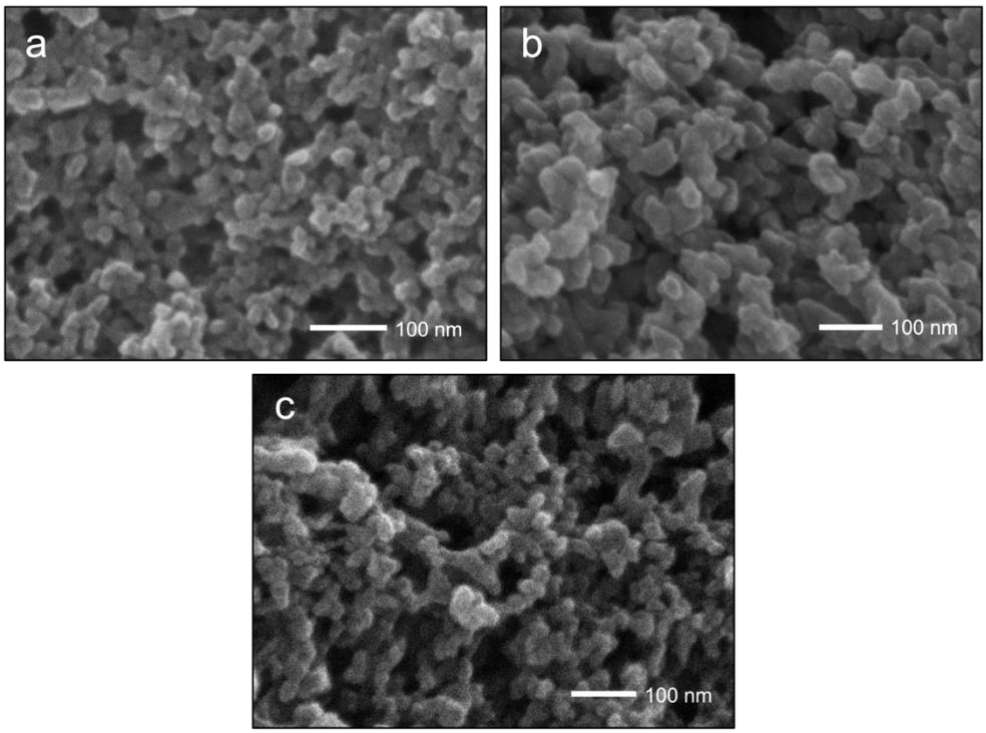

Figure 3.23. The SEM images of CuO nanoparticles synthesized at (a) 25 °C, (b) 45 °C, and (c) 65 °C.

The impact of the temperature of the reaction on the synthesis of CuO nanoparticles was observed by maintaining other factors constant while adjusting the temperature of the reaction. Figure 3.23 monitor the SEM images of CuO nanoparticles synthesized at different temperatures.

The CuO nanoparticles have similar morphology in all figures Figure 3.23a-c. They all were distinct and spherical in shape. The nanoparticles were ranged in size approximately 15 nm to 25 nm. The only difference in all images was that the nanoparticles synthesized at 65 °C was small aggregation that caused from higher kinetic energy during the synthesis while increasing the temperature of the reaction. Overall, increasing the temperature of the reaction on the synthesis of CuO nanoparticles had no noticeable difference on the morphology of nanoparticles.

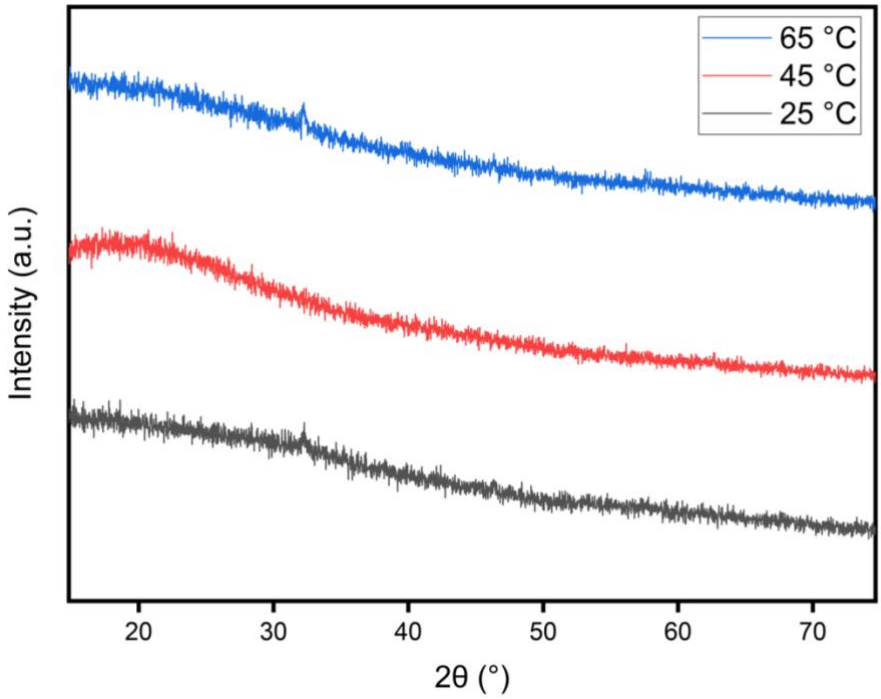

Figure 3.24. The XRD pattern of CuO nanoparticles synthesized at three different temperatures.

The XRD pattern of CuO nanoparticles synthesized at three different temperatures is shown in Figure 3.24. The XRD peaks of CuO nanoparticles synthesized at all temperatures present similar patterns. The only difference is that CuO nanoparticles synthesized at 45 °C have slight bump at 2θ=18°, whereas CuO nanoparticles synthesized at 25 °C and 65 °C have a slight sharp peak at 2θ=33° which put them forward. Therefore, optimum parameter for the synthesis of CuO nanoparticles was determined to be a 25 °C.

The optimum combination of these parameters was determined as follows after analyzing the effects of the mixing ratio, concentration, and temperature on the synthesis of CuO nanoparticles: a 2:1 mixing ratio, 25 mM Cu^{+2} solution, pH 5, and a reaction temperature of 25 °C. FT-IR, EDX, STEM, and detailed XPS analysis were conducted to further characterize the optimal conditions.

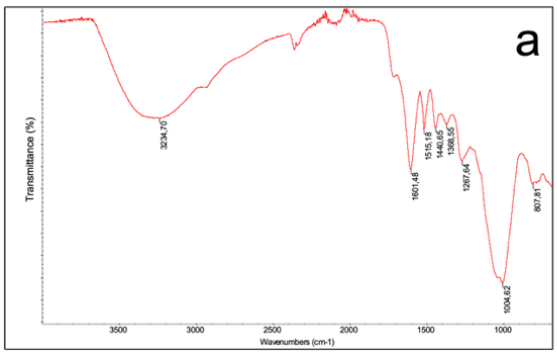

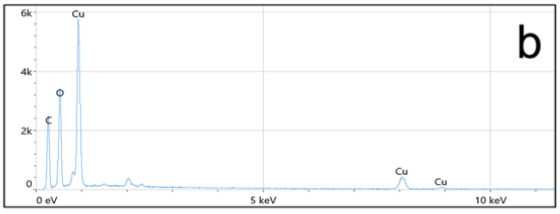

Element	Atomic %	Atomic % Error	Weight %	Weight % Error
C	39.7	0.2	22.3	0.1
O	45.5	0.2	34.0	0.2
Cu	14.7	0.1	43.7	0.2

Figure 3.25. The (a) FT-IR spectroscopy and (b) EDX spectrum of the CuO nanoparticles with *Prunus serrulata* leaf extract under the optimum conditions.

The FT-IR spectroscopy and EDX spectrum of the CuO nanoparticles synthesized under the optimum conditions are shown in Figure 3.25. The FT-IR spectroscopy in Figure 3.25a is almost identical to the previous FT-IR result obtained from Fe_3O_4 nanoparticles, confirming that CuO nanoparticles are covered with the same flavonoid, quercetin. Furthermore, the EDX spectrum in Figure 3.25b confirmed the CuO nanoparticles mostly consisted of O at 39.7%, then C at 45.5%, and Cu at 14.7% which shows the CuO nanoparticles oxidized more than Fe_3O_4 nanoparticles during the reaction.

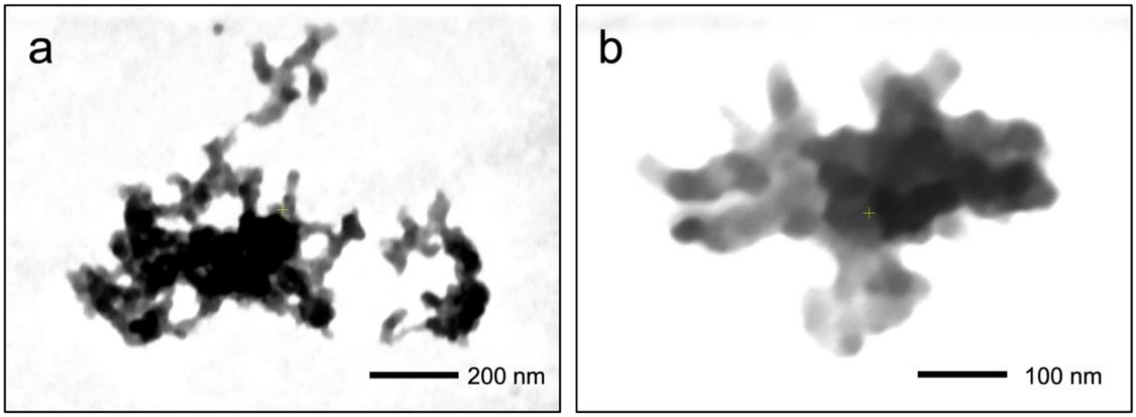

Figure 3.26. The STEM images of the CuO nanoparticles synthesized under the optimum conditions from two different scales: (a) 200 nm and (b) 100 nm.

The STEM images of the CuO nanoparticles synthesized under the optimum conditions are shown in Figure 3.26. The CuO nanoparticles at a scale of 200 nm in Figure

3.26a and a scale of 100 nm in Figure 3.26b had a contrast in nanoparticles, the darker inner sphere and the lighter or gray outer sphere, suggesting that the CuO nanoparticles synthesized under the optimum conditions were spherical and covered with organic molecules. The sizes of the CuO nanoparticles ranged between 20 nm to 25 nm. The STEM images were obtained by partially dissolving the solid CuO nanoparticles in EtOH first, then evaporating them on the copper grid. Therefore, aggregation was observed due to the reformation of nanoparticles. This phenomenon helped to explain the results obtained from the XRD, XPS, and EDX analyses.

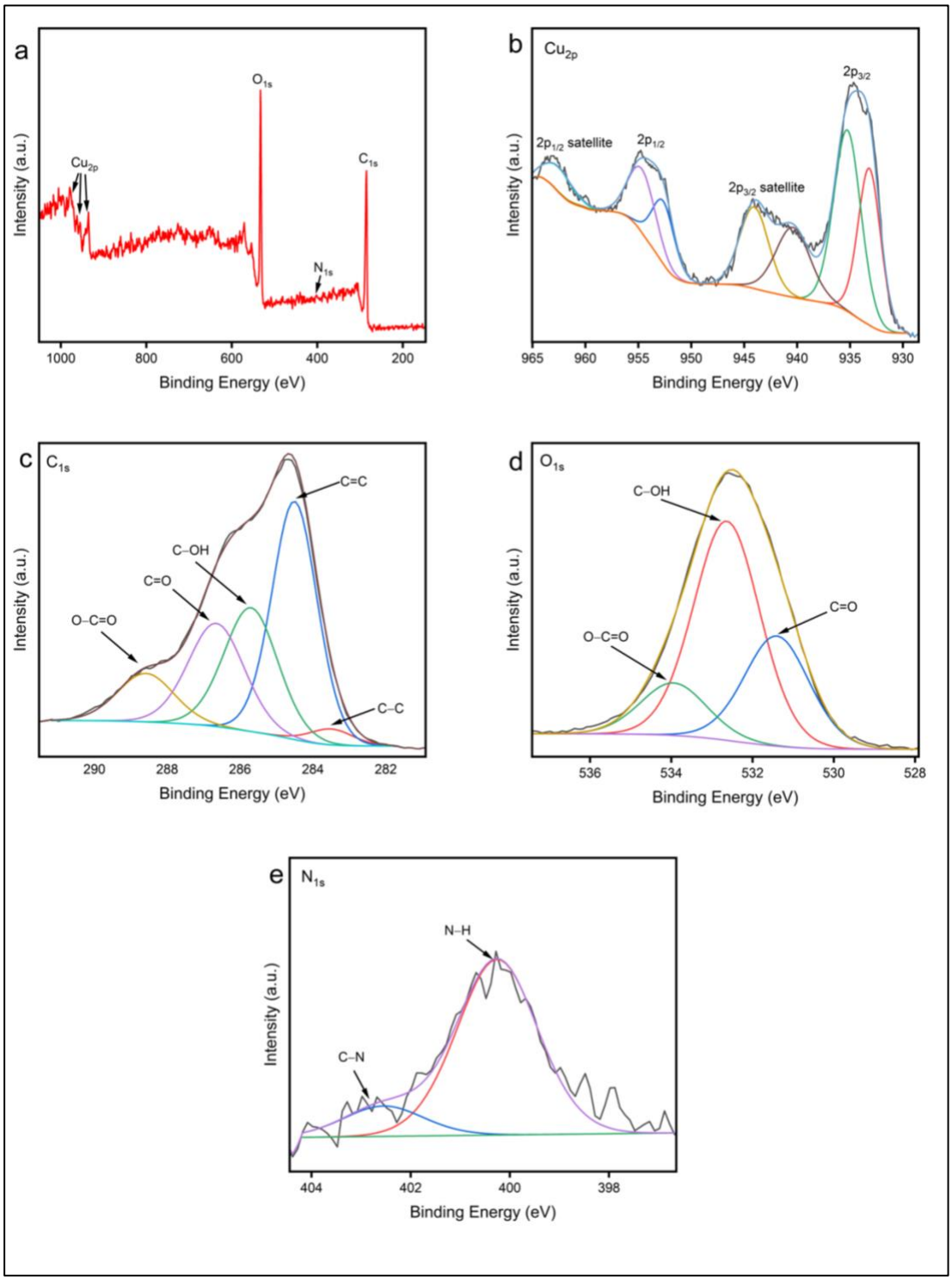

Figure 3.27. The XPS spectra of the CuO nanoparticles synthesized using *Prunus serrulata* leaf extract under the optimum conditions including the (a) survey and (b) Cu_{2p} (c), C_{1s}, (d) O_{1s}, and (e) N_{1s} profiles of the CuO nanoparticles.

The XPS results of the CuO nanoparticles synthesized under the optimum conditions are shown in Figure 3.27. The XPS survey in Figure 3.27a showed the presence of Cu, O, C, and N elements on the surface of CuO nanoparticles. The Cu_{2p} profile in Figure 3.27b displayed several characteristic peaks of $2p_{1/2}$ satellite, $2p_{1/2}$, $2p_{3/2}$ satellite, and $2p_{3/2}$ at 963.38 eV, 954.98 eV and 952.88 eV, 944.18 eV and 940.48 eV, 935.28 eV and 933.18 eV, respectively. The difference between $2p_{1/2}$ and $2p_{3/2}$ is 20.02 eV indicated the presence of Cu^{+2} ions in CuO nanoparticles, consistent with previous research [78–80]. Moreover, the presence of Cu^{+1} ions also seen in the XPS figure suggested that the mixture of Cu^{+1} and Cu^{+2} ions are both present in CuO nanoparticles [81, 82]. However, Cu^{+1} ions had a very low atomic percentage (0.87%), implying nanoparticles were mostly in CuO form. The C_{1s} profile in Figure 3.27c revealed the five characteristic peaks. The C–C peak at 283.58 eV, the C=C peak at 284.48 eV, the C–OH peak at 285.68 eV, the C=O peak at 286.68 eV, and the O–C=O at 288.58 eV were observed. The O_{1s} profile in Figure 3.27d showed three characteristic peaks. The C=O peak at 531.48 eV, the C–OH peak at 532.68 eV, and the O–C=O peak at 533.98 eV were observed. The N_{1s} profile in Figure. 3.27e displayed two characteristic peaks. The N–H peak at 400.28 eV and the C–N peak at 402.58 eV were observed. Overall, the C_{1s}, O_{1s}, and N_{1s} profiles confirmed that the surface of the nanoparticles was in oxide form whereas the Cu_{2p} profile indicated the presence of Cu^{+2} and Cu^{+1} peaks meaning that it was mostly in the CuO form. The XPS analysis was consistent with the XRD and FT-IR results.

3.4. Characterization of Zinc Oxide Nanoparticles

The synthesis of ZnO nanoparticles is controlled by a variety of factors. A comprehensive analysis for the synthesis of ZnO nanoparticles was designed and performed to attain a specific morphology within the desired size range. Factors such as the mixing ratio of Zn^{+2} solution to leaf extract, the concentration of Zn^{+2} solution, and the reaction temperature were examined to comprehend their impacts on the synthesis of ZnO nanoparticles.

The synthesis of ZnO nanoparticles was required one previous experiment about preventing chemical synthesis of ZnO material instead of producing ZnO nanoparticles using the green synthesis method.

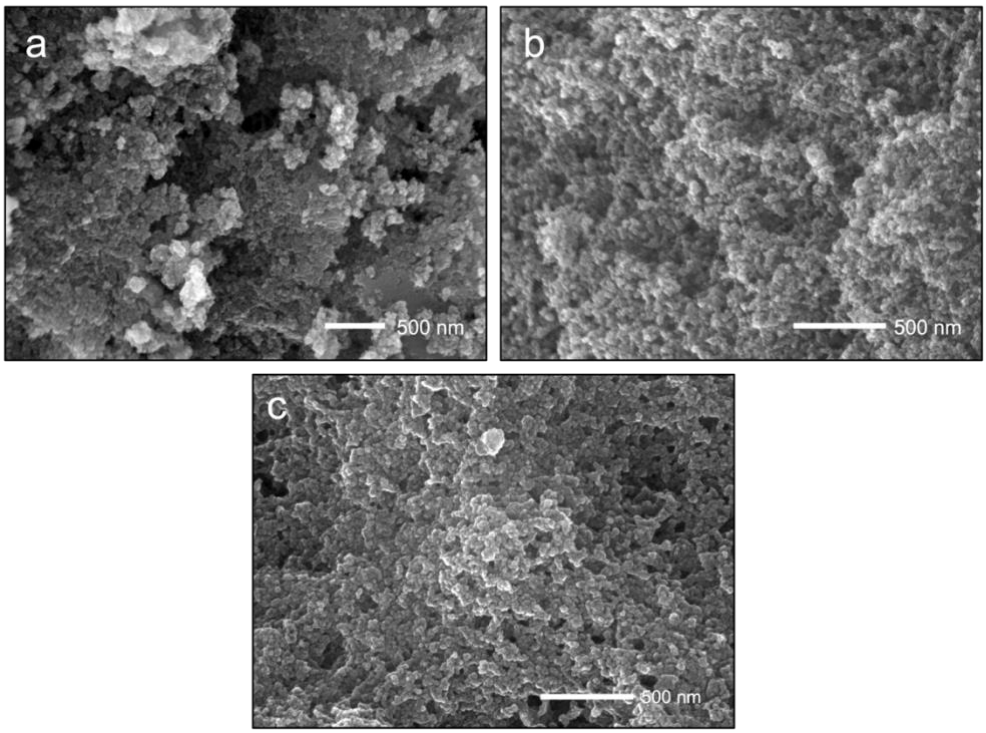

Figure 3.28. The SEM images of ZnO nanoparticles synthesized under different conditions: (a) immediate pH adjustment, (b) pH adjustment after stabilization, and (c) no pH adjustment.

The impact of pH adjustment on ZnO nanoparticle synthesis is presented in Figure 3.28. This experiment was conducted before identifying the optimal conditions, as Zn^{+2} ions tend to react with OH^- ions from NaOH molecules, potentially hindering the green synthesis process and leading to the chemical synthesis of ZnO molecules. Figure 3.28a displays the synthesis of ZnO nanoparticles with immediate pH adjustment, resulting in non-uniform nanoparticles with agglomeration and cavities. In contrast, Figure 3.28b shows the synthesis of ZnO nanoparticles with stabilization prior to the pH adjustment, resulting in uniform nanoparticles with similar size distribution. Finally, Figure 3.28c depicts the synthesis of ZnO nanoparticles without the pH adjustment, leading to homogenous but slightly agglomerated nanoparticles. Consequently, the optimal method for synthesizing ZnO nanoparticles was determined to be the stabilization first and then the pH adjustment method, as it prevents the chemical synthesis of ZnO nanoparticles.

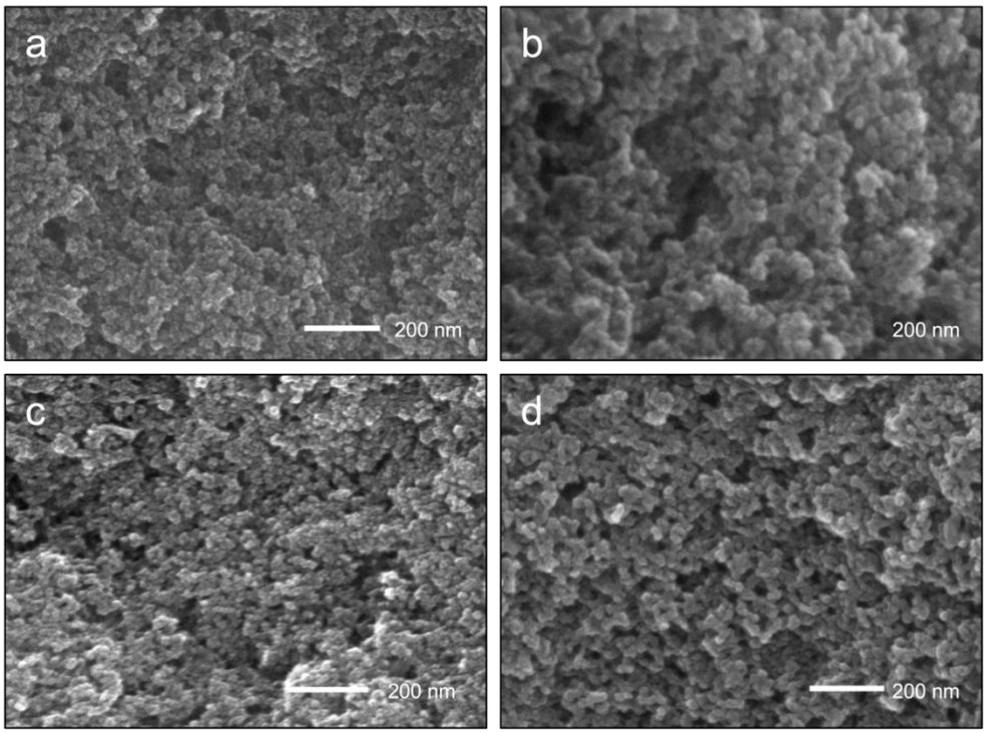

Figure 3.29. The SEM images of ZnO nanoparticles synthesized in (a) a 3:1 ratio, (b) a 2:1 ratio, (c) a 1:1 ratio, and (d) a 1:2 ratio.

The impact of the mixing ratio of the volume of Zn^{+2} solution and the leaf extract on the synthesis of ZnO nanoparticles was observed by maintaining other factors constant while changing the mixing ratio of the volume of Zn^{+2} solution to the leaf extract. Figure 3.29 shows the SEM images of ZnO nanoparticles synthesized in four different volume ratios.

The SEM image of ZnO nanoparticles synthesized in a 3:1 ratio is presented in Figure 3.29a. The nanoparticles were produced, and they were distinct enough to separate them from each other. Figure 3.29b-d show the SEM images of ZnO nanoparticles synthesized in a 2:1, a 1:1, and a 1:2 ratios. The ZnO nanoparticles synthesized in a 2:1, a 1:1, and a 1:2 ratios were similar to the ZnO nanoparticles synthesized in a 3:1 ratio. Overall, the ZnO nanoparticles were uniform and homogenous while having similar size distributions. They were approximately ranged in size from 10 nm to 15 nm.

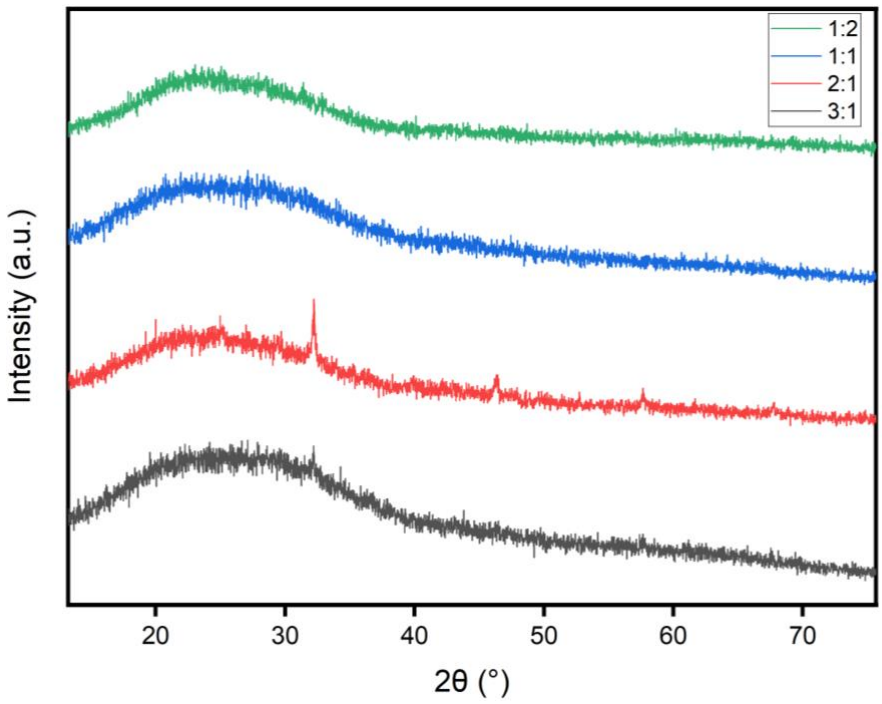

Figure 3.30. The XRD pattern of ZnO nanoparticles synthesized in four different volume ratios.

The XRD pattern of ZnO nanoparticles synthesized in four different volume ratios is presented in Figure 3.30. The XRD peaks of ZnO nanoparticles synthesized in a 3:1, a 1:1, and a 1:2 ratios have almost the same pattern. They all have broader peaks at 2θ=26°, caused by the phytochemicals from the leaf extract. The XRD peak of ZnO nanoparticles synthesized in a 2:1 ratio have slightly sharper peaks at 2θ=32°, 47°, 58°, and 69° that distinguishes it from other nanoparticles. These slightly sharper peaks indicate that ZnO nanoparticles synthesized in a 2:1 ratio had a stronger crystalline structure compared to other nanoparticles synthesized in various ratios. Therefore, the optimum condition for the impact of the mixing ratio of the Zn^{+2} solution and the leaf extract on the synthesis of ZnO nanoparticles was determined as a 2:1 ratio.

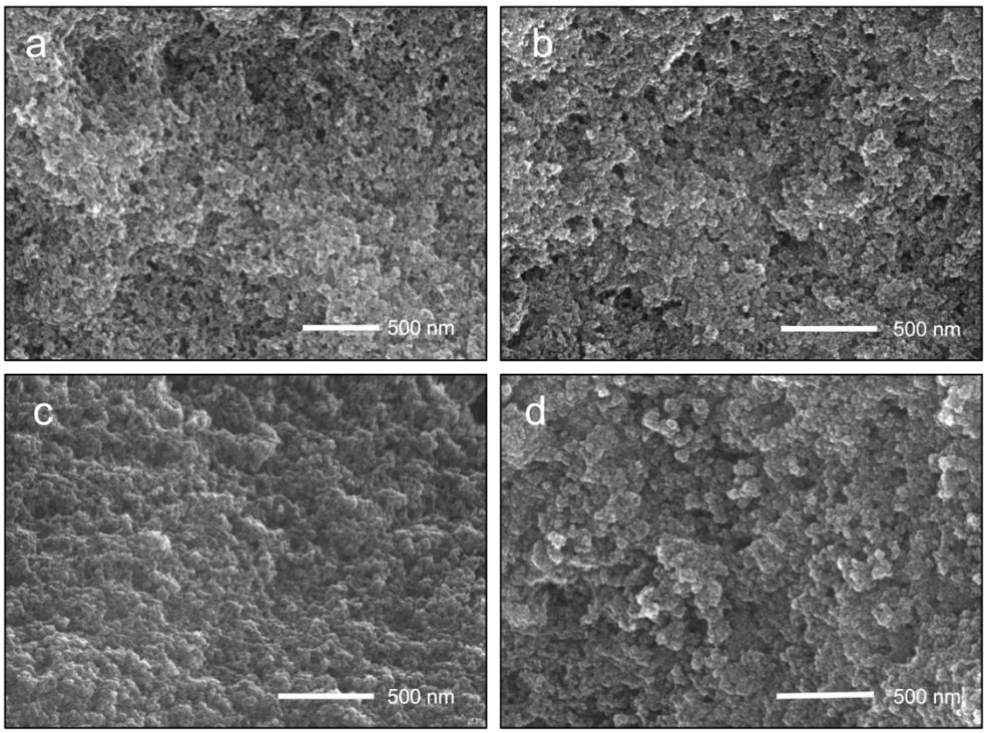

Figure 3.31. The SEM images of ZnO nanoparticles synthesized with (a) 10 mM, (b) 25 mM, (c) 50 mM, and (d) 75 mM Zn^{+2} solution.

The effect of the concentration of Zn^{+2} solution on the synthesis of ZnO nanoparticles was observed by maintaining other factors constant while changing the concentration of Cu^{+2} solution. Figure 3.31 indicates the SEM images of ZnO nanoparticles synthesized with four different concentrations of Zn^{+2} solution, $ZnNO_3.6H_2O$.

Figure 3.31a-d show the SEM images of ZnO nanoparticles synthesized with a concentration of 10 mM to 75 mM Zn^{+2} solution. The nanoparticles were formed in all concentrations. They were considerably distinct and homogenous. In all images, they were approximately ranged in size from 10 nm to 15 nm. Overall, increasing the concentration of Zn^{+2} solution did not cause any significant difference in the morphology of the synthesized ZnO nanoparticles.

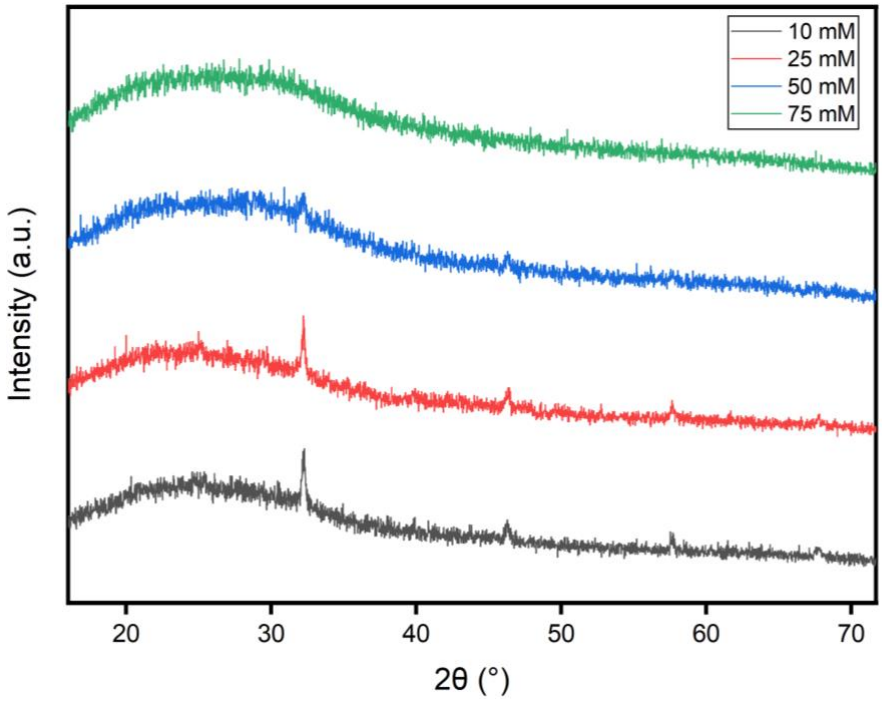

Figure 3.32. The XRD pattern of ZnO nanoparticles synthesized with four different concentrations.

The XRD pattern of ZnO nanoparticles synthesized at four different concentrations is presented in Figure 3.32. The XRD peaks of ZnO nanoparticles synthesized with 10 mM and 25 mM Zn^{+2} solutions have similar patterns. They have sharp peaks at 2θ=32°, 47°, 58°, and 69° that can confirm the ZnO nanoparticles were produced with a weakened crystalline structure. The XRD peaks of ZnO nanoparticles synthesized with 50 mM Zn^{+2} solution and 25 mM Zn^{+2} solution have broader peaks, or they do not show any clear peaks which make them more amorphous. This XRD pattern indicates that increasing the concentration of the Zn^{+2} solution resulted in a more amorphous crystalline structure. Therefore, the optimum condition for the impact of the concentration of the Zn^{+2} solution on the synthesis of ZnO nanoparticles was determined to be a 25 mM ratio.

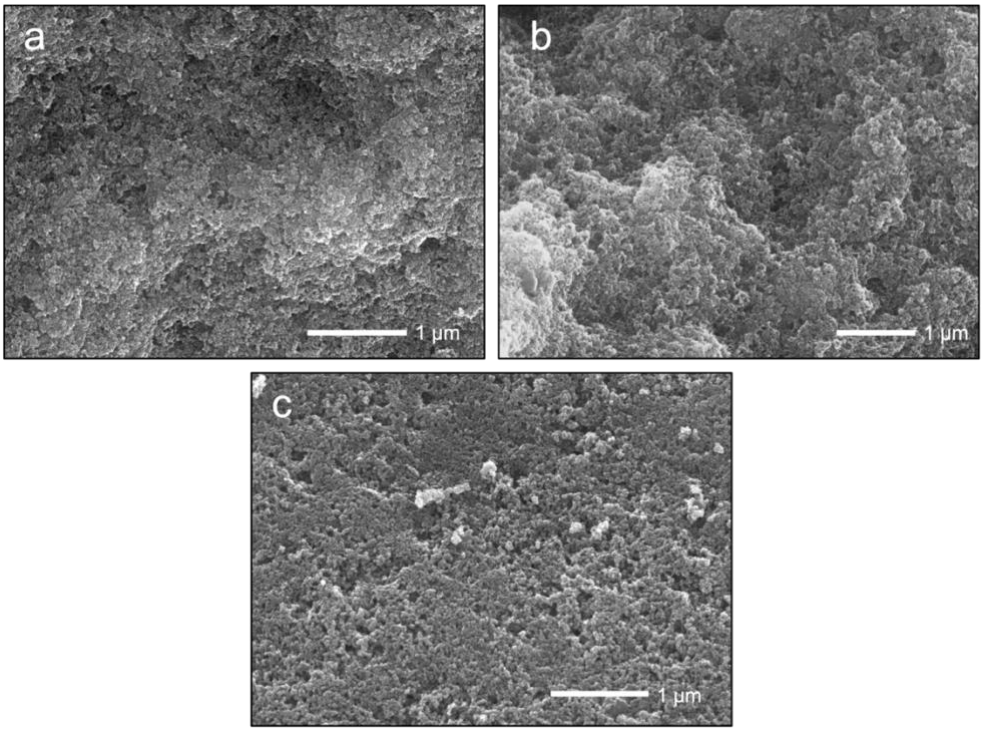

Figure 3.33. The SEM images of ZnO nanoparticles synthesized at (a) 25 °C, (b) 45 °C, and (c) 65 °C.

The impact of the temperature of the reaction on the synthesis of ZnO nanoparticles was observed by maintaining other factors constant while adjusting the temperature of the reaction. Figure 3.33 demonstrate the SEM images of ZnO nanoparticles synthesized at three different temperatures.

The ZnO nanoparticles have similar morphology in all figures (Figure 3.33a-c). They were all distinct and spherical in shape. They were ranged in size from approximately 10 nm to 15 nm. The only difference among all images, which were taken from a distance of 1 µm, was that the nanoparticles synthesized at 65 °C in Figure 3.33c appear more organized or lack a mound-like appearance, which was present in Figure 3.33a and b due to differences in angles of the image. Overall, increasing the reaction temperature had no noticeable impact on the synthesis of ZnO nanoparticles.

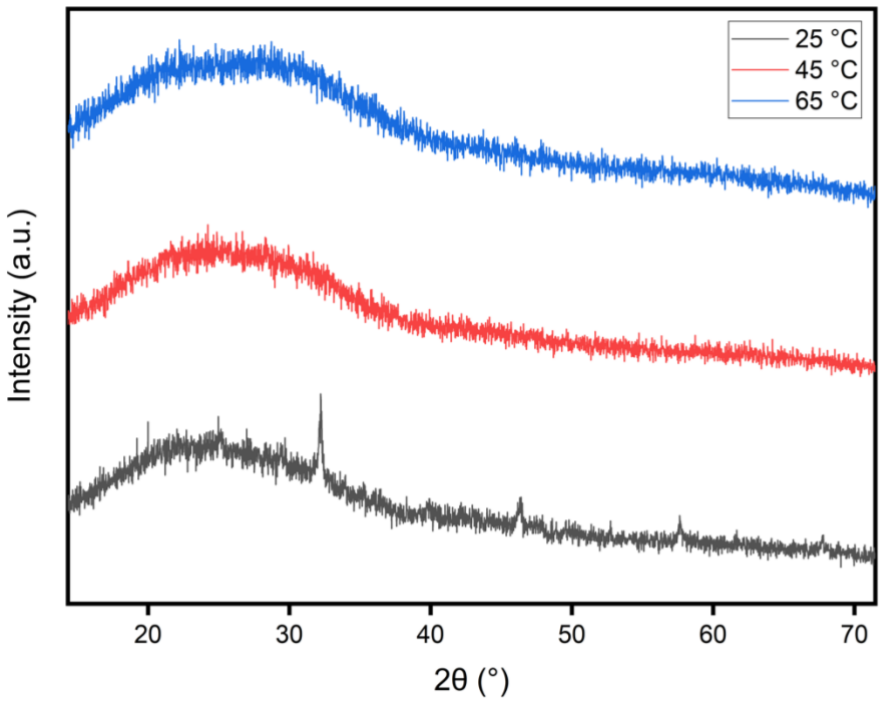

Figure 3.34. The XRD pattern of ZnO nanoparticles synthesized at three different temperatures.

The XRD pattern of ZnO nanoparticles synthesized at three different temperatures is shown in Figure 3.34. The XRD peaks of ZnO nanoparticles synthesized at 45 °C and 65 °C present similar patterns. The only difference is that ZnO nanoparticles synthesized at 25 °C have sharp peaks at 2θ=32°, 47°, 58°, and 69° that possess nanoparticles had a stronger crystalline structure. Therefore, the optimum condition for the impact of the temperature on the synthesis of ZnO nanoparticles was determined as 25 °C.

The optimum combination of these parameters was determined after analyzing the effects of the mixing ratio, concentration, and temperature on the synthesis of ZnO nanoparticles as follows: a 2:1 mixing ratio, 25 mM Zn^{+2} solution, pH 5, and a reaction temperature of 25 °C. FT-IR, EDX, STEM, and detailed XPS analysis were conducted to further characterize the optimal conditions.

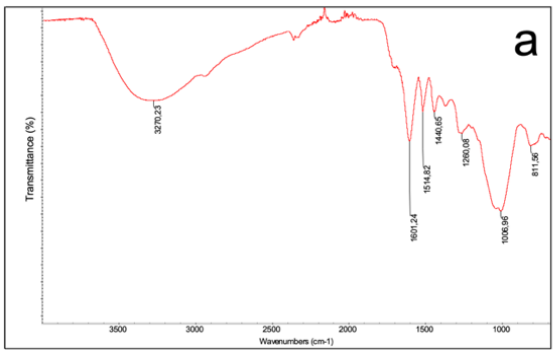

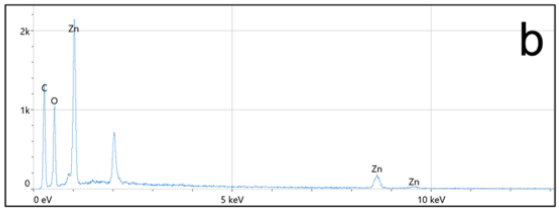

Element	Atomic %	Atomic % Error	Weight %	Weight % Error
C	51.0	0.3	28.3	0.2
O	33.4	0.3	24.7	0.2
Zn	15.6	0.1	47.0	0.3

Figure 3.35. The (a) FT-IR spectroscopy and (b) EDX spectrum of the ZnO nanoparticles with *Prunus serrulata* leaf extract under the optimum conditions.

The FT-IR spectroscopy and EDX spectrum of the ZnO nanoparticles synthesized under the optimum conditions are shown in Figure 3.35. The FT-IR spectroscopy in Figure 3.35a is identical to the previous FT-IR results obtained from Fe_3O_4 and CuO nanoparticles, confirming that ZnO nanoparticles are covered with the same flavonoid, quercetin. Additionally, the EDX spectrum in Figure 3.35b confirmed the ZnO nanoparticles mostly consisted of C at 51%, then O at 33.4%, and Zn at 15.6% which supports the role of phytochemicals in the synthesis of each metal nanoparticle.

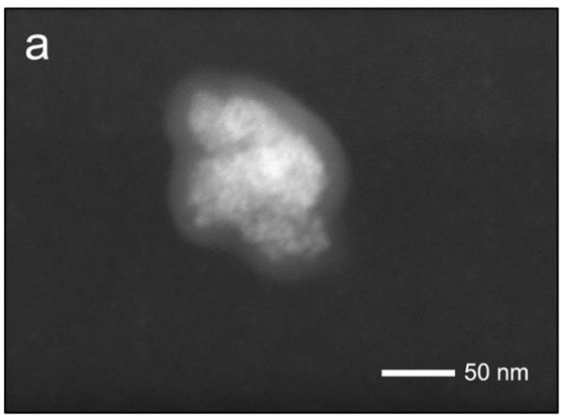

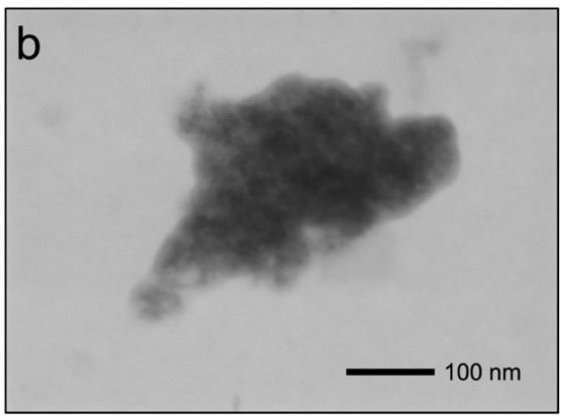

Figure 3.36. The STEM images of the ZnO nanoparticles synthesized under the optimum conditions from two different scales: (a) 50 nm and (b) 100 nm.

The STEM images of the ZnO nanoparticles synthesized under the optimum conditions are shown in Figure 3.36. HAADF detector in the STEM allowed for a closer

look at the synthesized nanoparticles in Figure 3.36a. It is clearly visible with the help of a HAADF mode that the nanoparticles, including Fe_3O_4 and CuO, are covered with quercetin from the leaf extract, and they are aggregated during the formation process. Therefore, the XRD results of all nanoparticles showed weakened crystalline structures, and the EDX and XPS results revealed that the highest percentage of elemental composition for each metal nanoparticle was carbon. Additionally, the STEM image which BF detector is used in Figure 3.36b demonstrated that ZnO nanoparticles synthesized under the optimum conditions ranged in size from 5 nm to 10 nm, even smaller than the nanoparticles shown in the previous SEM images.

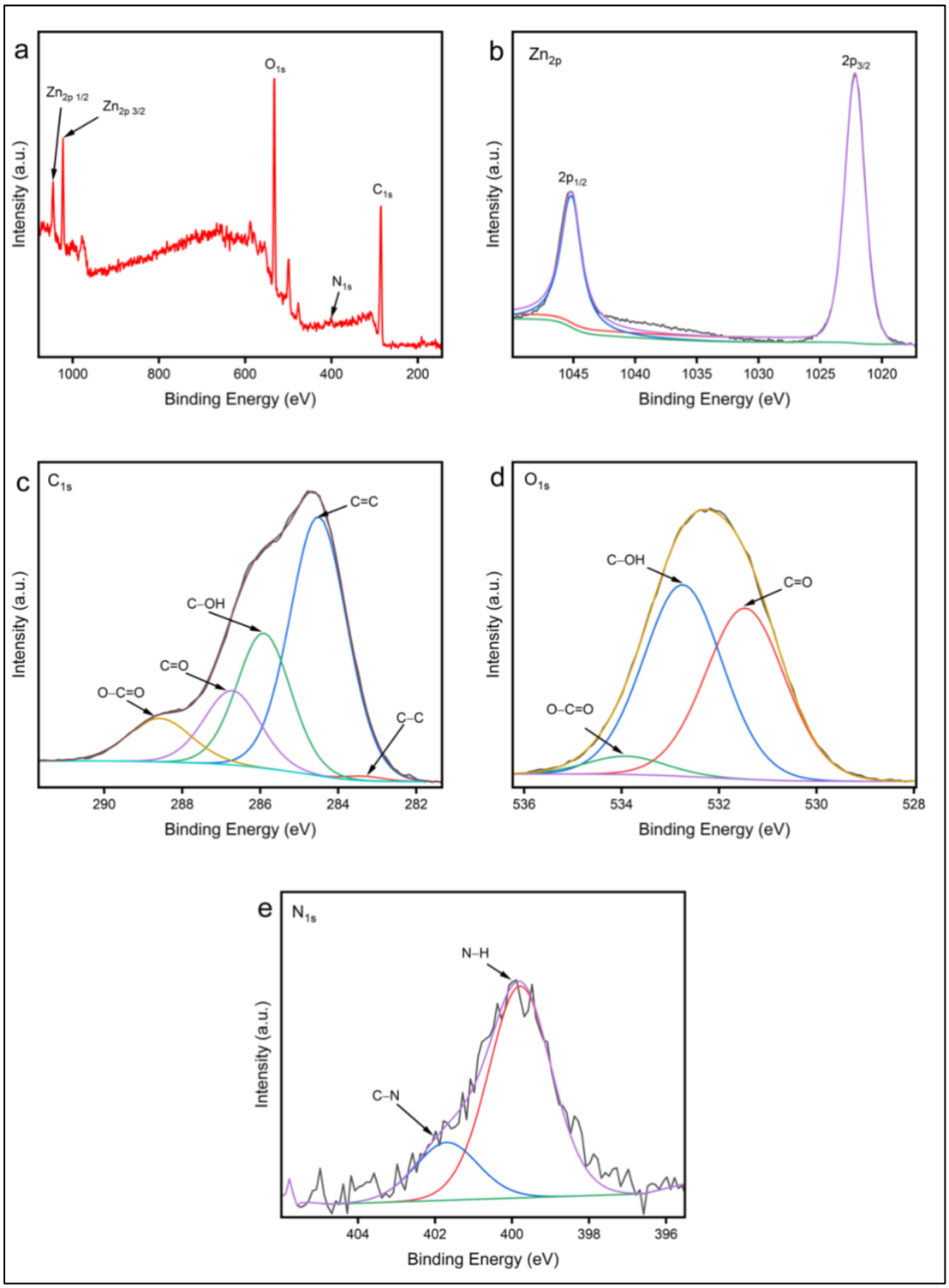

Figure 3.37. The XPS spectra of the ZnO nanoparticles synthesized using *Prunus serrulata* leaf extract under the optimum conditions including the (a) survey and (b) Zn_{2p} (c), C_{1s}, (d) O_{1s}, and (e) N_{1s} profiles of the ZnO nanoparticles.

The XPS results of the ZnO nanoparticles synthesized under the optimum conditions are shown in Figure 3.37. The XPS survey in Figure 3.37a showed the presence of Zn, C, O, and N elements on the surface of ZnO nanoparticles. The Zn_{2p} profile in Figure 3.37b displayed two characteristic peaks of $2p_{1/2}$ and $2p_{3/2}$ at 1022.18 eV and 1045.08 eV, respectively. The binding energy difference between these two peak, 22.9 eV, confirmed the Zn ions is in Zn^{+2} form according to the similar study [83]. The C_{1s} profile in Figure 3.37c revealed the five characteristic peaks similar to Fe_3O_4 and CuO nanoparticles. The C–C peak at 283.28 eV, the C=C peak at 284.48 eV, the C–OH peak at 285.88 eV, the C=O peak at 286.78 eV, and the O–C=O at 288.58 eV were observed. The O_{1s} profile in Figure 3.37d showed three characteristic peaks with smaller shifts according to similar research [84, 85]. The C=O peak at 531.48 eV, the C–OH peak at 532.78 eV, and the O–C=O peak at 533.98 eV were observed. The N_{1s} profile in Figure. 3.37e displayed two characteristic peaks. The N–H peak at 399.78 eV and the C–N peak at 401.68 eV were observed. Overall, the C_{1s}, O_{1s}, and N_{1s} profiles confirmed that the surface of the nanoparticles was in oxide form whereas the Zn_{2p} profile indicated the presence of Zn^{+2} peaks meaning that it was in the ZnO form. The XPS analysis was consistent with the XRD and FT-IR results.

4. CONCLUSION

The present study successfully demonstrates the synthesis of Fe_3O_4, CuO, and ZnO nanoparticles utilizing a plant-mediated extract of *Prunus serrulata* leaves. UV-Vis, FT-IR, LC-MS, and NMR analytical methods verify that quercetin from *Prunus serrulata* leaf extract is the responsible flavonoid as the reducing and capping agent for the synthesis of the nanoparticles. UV-Vis spectroscopy analysis of *Prunus serrulata* leaf extracts in ACN, MeOH, and H_2O confirms the detection of the flavonoid. FT-IR spectra results indicate the presence of the same flavonoid on the surface of stabilized nanoparticles. LC-MS spectroscopy results establish that this flavonoid is found most abundantly with a 325 m/z ratio in $[M+Na]^+$ mode, matching with quercetin. Finally, ^{1}H-NMR spectroscopy validates that this flavonoid has specific protons that belong to quercetin.

All of the synthesized nanoparticles ranged in size between 10 nm to 100 nm, which was aimed at the beginning of this project. In order to control the morphology and crystalline structure of the nanoparticles, the effect of the volume ratio between the reaction precursors and the plant-mediated extract, the concentration of the reaction precursors, the pH, and the temperature of the reactions are investigated to determine the optimum conditions for each type of nanoparticle. The morphological analysis of the nanoparticles is conducted employing SEM, STEM, EDX, XRD, and XPS analytical methods. SEM results demonstrate that all of the synthesized nanoparticles have a spherical shape. STEM results display the nanoparticles with higher-resolution images. EDX results indicate the elemental composition of the nanoparticles, mostly C and O elements with higher percentages and metals (Fe, Cu, and Zn) with lower percentages. XRD results confirm that all of the produced nanoparticles have an amorphous structure and does not have strong crystal planes in their structures. Finally, XPS results show that all of the produced nanoparticles are in oxide form on their surfaces, and Fe_3O_4, CuO, and ZnO nanoparticles are produced with their corresponding oxidation states (Fe^{+2} and Fe^{+3} together, Cu^{+2} and Zn^{+2}).

5. FUTURE WORK

The biggest challenge encountered during this work was obtaining amorphous nanoparticles over the development of stronger crystalline structures. It made it difficult to analyze the produced nanoparticles since most of the XRD patterns were similar and did not have noticeable differences. Therefore, XPS analysis was required to confirm the oxidation states of the nanoparticles. One possible solution to this problem might be changing variables. The variables in this research were chosen after conducting multiple experiments. Several leaves, different weight percentages of leaf extracts, and concentrations of the metal ions solutions were investigated, but there is no limit to further experimentation. In the end, it may be possible to find stronger crystalline structures without increasing the size of the nanoparticles.

The next step for this study is to expand the green synthesis method not only for a wider range of nanoparticles but also for core-shell structures. For example, Se nanoparticles are promising for the nutritional industry, and utilizing them in this industry might provide economic advantages. However, the production of this type of nanoparticle employing the green synthesis method is limited in the literature due to the greater difficulty in the precipitation of Se nanoparticles compared to iron, copper, or zinc nanoparticles. It requires additional analytical methods and energy. On the other hand, for instance, it might be worth trying to combine Se and iron nanoparticles together, since iron nanoparticles are readily producible and could easily encapsulate Se nanoparticles in a possible reaction.

Last but not least, nanoparticles synthesized through the green synthesis method could be useful in various industries as catalysts and renewable energy sources. The development of efficient and environmentally friendly catalysts could increase reaction rates. Moreover, the implementation of these nanoparticles in fuel cells or materials used in wind turbines could increase their efficiency while reducing their carbon footprint.

REFERENCES

1. Christian, P., F. Von der Kammer, M. Baalousha, and T. Hofmann, “Nanoparticles: Structure, Properties, Preparation and Behavior in Environmental Media”, *Ecotoxicology*, Vol. 17, No. 5, pp. 326–343, 2008.

2. Jahangirian, H., K. Kalantari, Z. Izadiyan, R. Rafiee-Moghaddam, K. Shameli, and T. J. Webster, “A Review of Small Molecules and Drug Delivery Applications Using Gold and Iron Nanoparticles”, *International Journal of Nanomedicine*, Vol. 14, pp. 1633–1657, 2019.

3. Silva, S., A. Almeida, and N. Vale, “Combination of Cell-Penetrating Peptides With Nanoparticles for Therapeutic Application: A Review”, *Biomolecules*, Vol. 9, No. 1, p. 22, 2019.

4. Sircar, A., K. Rayavarapu, N. Bist, K. Yadav, and S. Singh, “Applications of Nanoparticles in Enhanced Oil Recovery”, *Petroleum Research*, Vol. 7, No. 1, pp. 77–90, 2022.

5. Abid, N., A. M. Khan, S. Shujait, K. Chaudhary, M. Ikram, M. Imran, J. Haider, M. Khan, Q. Khan, and M. Maqbool, “Synthesis of Nanomaterials Using Various Top-Down and Bottom-Up Approaches, Influencing Factors, Advantages and Disadvantages: A Review.”, *Advances in Colloid and Interface Science*, Vol. 300, p. 102597, 2022.

6. Saif, S., A. Tahir, and Y. Chen, “Green Synthesis of Iron Nanoparticles and Their Environmental Applications and Implications”, *Nanomaterials*, Vol. 6, No. 11, p. 209, 2016.

7. Nguefack, M., A. F. Popa, S. Rossignol, and C. Kappenstein, “Preparation of Alumina Through a Sol–Gel Process. Synthesis, Characterization, Thermal Evolution and

Model of Intermediate Boehmite", *Physical Chemistry Chemical Physics*, Vol. 5, No. 19, pp. 4279–4289, 2003.

8. Jensen, K. M. Ø., H. L. Andersen, C. Tyrsted, E. D. Bøjesen, A. C. Dippel, N. Lock, S. J. L. Billinge, B. B. Iversen, and M. Christensen, "Mechanisms for Iron Oxide Formation under Hydrothermal Conditions: An In Situ Total Scattering Study", *ACS Nano*, Vol. 8, No. 10, pp. 10704–10714, 2014.

9. Rajaeiyan, A. and M. M. Bagheri-Mohagheghi, "Comparison of Sol-Gel and Co-Precipitation Methods on the Structural Properties and Phase Transformation of γ and α-Al_2O_3 Nanoparticles", *Advances in Manufacturing*, Vol. 1, No. 2, pp. 176–182, 2013.

10. Wang, Y. and Y. Xia, "Bottom-Up and Top-Down Approaches to the Synthesis of Monodispersed Spherical Colloids of Low Melting-point Metals", *Nano Letters*, Vol. 4, No. 10, pp. 2047–2050, 2004.

11. Solanki, J. N. and Z. V. P. Murthy, "Controlled Size Silver Nanoparticles Synthesis With Water-in-Oil Microemulsion Method: A Topical Review", *Industrial & Engineering Chemistry Research*, Vol. 50, No. 22, pp. 12311–12323, 2011.

12. Singh, L. P., S. K. Bhattacharyya, R. Kumar, G. Mishra, U. Sharma, G. Singh, and S. Ahalawat, "Sol-Gel Processing of Silica Nanoparticles and Their Applications", *Advances in Colloid and Interface Science*, Vol. 214, pp. 17–37, 2014.

13. Rane, A. V., K. Kanny, V. K. Abitha, S. Thomas, and S. Thomas, *Synthesis of Inorganic Nanomaterials*, Elsevier, Cambridge, 2018.

14. Gan, Y. X., A. H. Jayatissa, Z. Yu, X. Chen, and M. Li, "Hydrothermal Synthesis of Nanomaterials", *Journal of Nanomaterials*, Vol. 2020, pp. 1–3, 2020.

15. Yang, G. and S. J. Park, “Conventional and Microwave Hydrothermal Synthesis and Application of Functional Materials: A Review”, *Materials*, Vol. 12, No. 7, p. 1177, 2019.

16. Huang, G., C. H. Lu, and H. H. Yang, *Novel Nanomaterials for Biomedical, Environmental and Energy Applications*, Elsevier, Amsterdam, 2019.

17. Odularu, A. T., “Metal Nanoparticles: Thermal Decomposition, Biomedicinal Applications to Cancer Treatment, and Future Perspectives”, *Bioinorganic Chemistry and Applications*, Vol. 2018, pp. 1–6, 2018.

18. Malik, M. A., M. Y. Wani, and M. A. Hashim, “Microemulsion Method: A Novel Route to Synthesize Organic and Inorganic Nanomaterials”, *Arabian Journal of Chemistry*, Vol. 5, No. 4, pp. 397–417, 2012.

19. Riegler, J. and T. Nann, “Application of Luminescent Nanocrystals as Labels for Biological Molecules”, *Analytical and Bioanalytical Chemistry*, Vol. 379, No. 7–8, pp. 913–919, 2004.

20. Deepak, P., V. Amutha, C. Kamaraj, G. Balasubramani, D. Aiswarya, and P. Perumal, *Green Synthesis, Characterization and Applications of Nanoparticles*, Elsevier, Amsterdam, 2019.

21. Kirtane, A. R., M. Verma, P. Karandikar, J. Furin, R. Langer, and G. Traverso, “Nanotechnology Approaches for Global Infectious Diseases”, *Nature Nanotechnology*, Vol. 16, No. 4, pp. 369–384, 2021.

22. Wong, C. Y., H. Al-Salami, and C. R. Dass, “Potential of Insulin Nanoparticle Formulations for Oral Delivery and Diabetes Treatment”, *Journal of Controlled Release*, Vol. 264, pp. 247–275, 2017.

23. Cong, W., R. Bai, Y. F. Li, L. Wang, and C. Chen, “Selenium Nanoparticles as an Efficient Nanomedicine for the Therapy of Huntington’s Disease”, *ACS Applied Materials and Interfaces*, Vol. 11, No. 38, pp. 34725–34735, 2019.

24. Rezaei, R., M. Safaei, H. R. Mozaffari, H. Moradpoor, S. Karami, A. Golshah, B. Salimi, and H. Karami, “The Role of Nanomaterials in the Treatment of Diseases and Their Effects on the Immune System”, *Open Access Macedonian Journal of Medical Sciences*, Vol. 7, No. 11, pp. 1884–1890, 2019.

25. Oz, Y., M. Arslan, T. N. Gevrek, R. Sanyal, and A. Sanyal, “Modular Fabrication of Polymer Brush Coated Magnetic Nanoparticles: Engineering the Interface for Targeted Cellular Imaging”, *ACS Applied Materials and Interfaces*, Vol. 8, No. 30, pp. 19813–19826, 2016.

26. Banerjee, A. N., “Graphene and Its Derivatives as Biomedical Materials: Future Prospects and Challenges”, *Interface Focus*, Vol. 8, No. 3, p. 20170056, 2018.

27. Skalickova, S., V. Milosavljevic, K. Cihalova, P. Horky, L. Richtera, and V. Adam, “Selenium Nanoparticles as a Nutritional Supplement”, *Nutrition*, Vol. 33, pp. 83–90, 2017.

28. Surai, P. F. and I. I. Kochish, “Food for Thought: Nano-Selenium in Poultry Nutrition and Health”, *Animal Health Research Reviews*, Vol. 21, No. 2, pp. 103–107, 2020.

29. Lyons, M. P., T. T. Papazyan, and P. F. Surai, “Selenium in Food Chain and Animal Nutrition: Lessons from Nature -Review-”, *Asian-Australasian Journal of Animal Sciences*, Vol. 20, No. 7, pp. 1135–1155, 2007.

30. Bodnar, M., P. Konieczka, and J. Namiesnik, “The Properties, Functions, and Use of Selenium Compounds in Living Organisms”, *Journal of Environmental Science and Health, Part C*, Vol. 30, No. 3, pp. 225–252, 2012.

31. Hosnedlova, B., M. Kepinska, S. Skalickova, C. Fernandez, B. Ruttkay-Nedecky, T. D. Malevu, J. Sochor, M. Baron, M. Melcova, J. Zidkova, and R. Kizek, "A Summary of New Findings on the Biological Effects of Selenium in Selected Animal Species—A Critical Review", *International Journal of Molecular Sciences*, Vol. 18, No. 10, p. 2209, 2017.

32. Parveen, K., V. Banse, and L. Ledwani, "Green Synthesis of Nanoparticles: Their Advantages and Disadvantages", *AIP Conference Proceedings*, Rajasthan, pp. 020048, 2015.

33. Goutam, S. P., G. Saxena, D. Roy, A. K. Yadav, and R. N. Bharagava, *Bioremediation of Industrial Waste for Environmental Safety*, Springer, Singapore, 2020.

34. Sengul, A. B. and E. Asmatulu, "Toxicity of Metal and Metal Oxide Nanoparticles: A Review", *Environmental Chemistry Letters*, Vol. 18, No. 5, pp. 1659–1683, 2020.

35. Bahrulolum, H., S. Nooraei, N. Javanshir, H. Tarrahimofrad, V. S. Mirbagheri, A. J. Easton, and G. Ahmadian, "Green Synthesis of Metal Nanoparticles Using Microorganisms and Their Application in the Agrifood Sector", *Journal of Nanobiotechnology*, Vol. 19, No. 1, p. 86, 2021.

36. Sastry, M., A. Ahmad, M. Islam Khan, and R. Kumar, "Biosynthesis of Metal Nanoparticles Using Fungi", *Current Science*, Vol. 85, No. 2, pp. 162–170, 2003.

37. Majeed, S., M. Danish, A. H. Binti Zahrudin, and G. K. Dash, "Biosynthesis and Characterization of Silver Nanoparticles from Fungal Species and Its Antibacterial and Anticancer Effect", *Karbala International Journal of Modern Science*, Vol. 4, No. 1, pp. 86–92, 2018.

38. Rostami, H., F. Khosravi, M. Mohseni, and A. A. Rostami, "Biosynthesis of Ag Nanoparticles Using Isolated Bacteria from Contaminated Sites and Its Application as an Efficient Catalyst for Hydrazine Electrooxidation", *International Journal of Biological Macromolecules*, Vol. 107, No. PartA, pp. 343–348, 2018.

39. Ajinkya, N., X. Yu, P. Kaithal, H. Luo, P. Somani, and S. Ramakrishna, “Magnetic Iron Oxide Nanoparticle (IONP) Synthesis to Applications: Present and Future”, *Materials*, Vol. 13, No. 20, p. 4644, 2020.

40. Elfeky, S. A., S. E. Mahmoud, and A. F. Youssef, “Applications of CTAB Modified Magnetic Nanoparticles for Removal of Chromium (VI) from Contaminated Water”, *Journal of Advanced Research*, Vol. 8, No. 4, pp. 435–443, 2017.

41. Kumar, P., V. Tomar, D. Kumar, R. K. Joshi, and M. Nemiwal, “Magnetically Active Iron Oxide Nanoparticles for Catalysis of Organic Transformations: A Review”, *Tetrahedron*, Vol. 106–107, p. 132641, 2022.

42. Jung, D. S., Y. N. Ko, Y. C. Kang, and S. Bin Park, “Recent Progress in Electrode Materials Produced by Spray Pyrolysis for Next-Generation Lithium-ion Batteries”, *Advanced Powder Technology*, Vol. 25, No. 1, pp. 18–31, 2014.

43. Cruz, P., Y. Pérez, I. del Hierro, and M. Fajardo, “Copper, Copper Oxide Nanoparticles and Copper Complexes Supported on Mesoporous SBA-15 as Catalysts in the Selective Oxidation of Benzyl Alcohol in Aqueous Phase”, *Microporous and Mesoporous Materials*, Vol. 220, pp. 136–147, 2016.

44. Benhadria, N., M. Hachemaoui, F. Zaoui, A. Mokhtar, S. Boukreris, T. Attar, L. Belarbi, and B. Boukoussa, “Catalytic Reduction of Methylene Blue Dye by Copper Oxide Nanoparticles”, *Journal of Cluster Science*, Vol. 33, No. 1, pp. 249–260, 2022.

45. Wanninayake, A. P., S. Gunashekar, S. Li, B. C. Church, and N. Abu-Zahra, “Performance Enhancement of Polymer Solar Cells Using Copper Oxide Nanoparticles”, *Semiconductor Science and Technology*, Vol. 30, No. 6, p. 064004, 2015.

46. Singh, J., G. Kaur, and M. Rawat, “A Brief Review on Synthesis and Characterization of Copper Oxide Nanoparticles and its Applications”, *Journal of Bioelectronics and Nanotechnology*, Vol. 1, No. 1, p. 2016.

47. Xiong, Q., A. Liu, Q. Ren, Y. Xue, X. Yu, Y. Ying, H. Gao, H. Tan, Z. Zhang, W. Li, S. Zeng, and C. Xu, "Cuprous Oxide Nanoparticles Trigger Reactive Oxygen Species-Induced Apoptosis Through Activation of Erk-Dependent Autophagy in Bladder Cancer", *Cell Death & Disease*, Vol. 11, No. 5, p. 366, 2020.

48. Wongpisutpaisan, N., P. Charoonsuk, N. Vittayakorn, and W. Pecharapa, "Sonochemical Synthesis and Characterization of Copper Oxide Nanoparticles", *Energy Procedia*, Vol. 9, pp. 404–409, 2011.

49. Waichal, R. P., G. D. Karvir, K. R. Patil, P. Ambekar, I. S. Mulla, and S. N. Kale, "Synthesis of Cuprous Oxide Nanoparticles by Electrochemical Method and Evaluation of the Corresponding Nanoparticle Film for Humidity Sensing", *1st International Symposium on Physics and Technology of Sensors (ISPTS-1)*, Pune, pp. 47–50, 2012.

50. Muhammad, W., N. Ullah, M. Haroon, and B. H. Abbasi, "Optical, Morphological and Biological Analysis of Zinc Oxide Nanoparticles (ZnO NPs) Using *Papaver somniferum* L.", *RSC Advances*, Vol. 9, No. 51, pp. 29541–29548, 2019.

51. Smijs, T. and Pavel, "Titanium Dioxide and Zinc Oxide Nanoparticles in Sunscreens: Focus on Their Safety and Effectiveness", *Nanotechnology, Science and Applications*, Vol. 4, No. 1, p. 95, 2011.

52. Vijayakumar, S., B. Vaseeharan, B. Malaikozhundan, and M. Shobiya, "*Laurus nobilis* Leaf Extract Mediated Green synthesis of ZnO Nanoparticles: Characterization and Biomedical Applications", *Biomedicine & Pharmacotherapy*, Vol. 84, pp. 1213–1222, 2016.

53. Anju Manuja, R. R., "Zinc Oxide Nanoparticles: Opportunities and Challenges in Veterinary Sciences", *Immunome Research*, Vol. 11, No. 2, p. 2015.

54. Engelhard, M. H., T. C. Droubay, and Y. Du, *Encyclopedia of Spectroscopy and Spectrometry*, Elsevier, London, 2017.

55. Roodbar Shojaei, T., S. Soltani, and M. Derakhshani, *Fundamentals of Bionanomaterials*, Elsevier, Dublin, 2022.

56. Titus, D., E. James, J. Samuel, and S. M. Roopan, *Green Synthesis, Characterization and Applications of Nanoparticles*, Elsevier, Amsterdam, 2019.

57. Jose Chirayil, C., J. Abraham, R. Kumar Mishra, S. C. George, and S. Thomas, *Thermal and Rheological Measurement Techniques for Nanomaterials Characterization*, Elsevier, Amsterdam, 2017.

58. Mukherjee, P. K., *Quality Control and Evaluation of Herbal Drugs*, Elsevier, Imphal, 2019.

59. Stark, N. M., D. J. Yelle, and U. P. Agarwal, *Lignin in Polymer Composites,* Elsevier, Oxford, 2016.

60. Kaliva, M. and M. Vamvakaki, *Polymer Science and Nanotechnology*, Elsevier, Amsterdam, 2020.

61. Dias, M. C., D. C. G. A. Pinto, and A. M. S. Silva, "Plant Flavonoids: Chemical Characteristics and Biological Activity", *Molecules*, Vol. 26, No. 17, p. 5377, 2021.

62. Rani Verma, P. and F. Khan, "Green Approach for Biofabrication of CuO Nanoparticles From *Prunus amygdalus* Pericarp Extract and Characterization", *Inorganic and Nano-Metal Chemistry*, Vol. 49, No. 3, pp. 69–74, 2019.

63. Jeevanandam, J., Y. S. Chan, and Y. H. Ku, "Aqueous *Eucalyptus globulus* Leaf Extract-Mediated Biosynthesis of MgO Nanorods", *Applied Biological Chemistry*, Vol. 61, No. 2, pp. 197–208, 2018.

64. Yi, E. J., E. S. Yoo, C. H. Han, and A. R. Lee, "Dyeing Properties and Color Characteristics of Silk Fabrics Dyed with *Prunus yedoensis* Matsumura Flower Extract", *Textile Coloration and Finishing*, Vol. 22, No. 3, pp. 194–206, 2010.

65. Nandiyanto, A. B. D., R. Oktiani, and R. Ragadhita, "How to Read and Interpret FTIR Spectroscope of Organic Material", *Indonesian Journal of Science and Technology*, Vol. 4, No. 1, p. 97, 2019.

66. Horai, H., M. Arita, S. Kanaya, T. Nishioka, "MassBank: A Public Repository for Sharing Mass Spectral Data for Life Sciences", *Journal of Mass Spectrometry*, Vol. 45, No. 7, pp. 703–714, 2010.

67. Turan, B., A. Gülşen, D. P. Makris, and P. Kefalas, "Interactions Between Quercetin and Catechin in A Model Matrix: Effects on the in Vitro Antioxidant Behavior", *Food Research International*, Vol. 40, No. 7, pp. 819–826, 2007.

68. Bouhoreira, A. and B. Dadamoussa, "Characterization of Some Flavonoids in *Phoenix dactylifera L* Using HPLC-MS-MS", *Journal of Chemical and Pharmaceutical Research*, Vol. 8, No. 5, pp. 169–176, 2016.

69. Pilařová, V., L. Kuda, H. K. Vlčková, L. Nováková, S. Gupta, M. Kulkarni, F. Švec, J. Van Staden, and K. Doležal, "Carbon Dioxide Expanded Liquid: An Effective Solvent for the Extraction of Quercetin From South African Medicinal Plants", *Plant Methods*, Vol. 18, No. 1, p. 87, 2022.

70. Aytac, Z., S. Ipek, E. Durgun, and T. Uyar, "Antioxidant Electrospun Zein Nanofibrous Web Encapsulating Quercetin/cyclodextrin Inclusion Complex", *Journal of Materials Science*, Vol. 53, No. 2, pp. 1527–1539, 2018.

71. Wishart, D. S., C. Knox, A. C. Guo, I. Forsythe, "HMDB: A Knowledgebase for the Human Metabolome", *Nucleic Acids Research*, Vol. 37, No. Database, pp. D603–D610, 2009.

72. Holder, C. F. and R.E. Schaak, "Tutorial on Powder X-ray Diffraction for Characterizing Nanoscale Materials", *ACS Nano*, Vol. 13, No. 7, pp. 7359–7365, 2019.

73. Hawn, D. D. and B. M. Dekoven, “Deconvolution as a Correction for Photoelectron Inelastic Energy Losses in the Core Level XPS Spectra of Iron Oxides”, *Surface and Interface Analysis*, Vol. 10, pp. 63–74, 1987.

74. Njagi, E. C., H. Huang, L. Stafford, H. Genuino, H. M. Galindo, J. B. Collins, G. E. Hoag, and S. L. Suib, “Biosynthesis of Iron and Silver Nanoparticles at Room Temperature Using Aqueous Sorghum Bran Extracts”, *Langmuir*, Vol. 27, No. 1, pp. 264–271, 2011.

75. Han, F., L. Ma, Q. Sun, C. Lei, and A. Lu, “Rationally Designed Carbon-Coated Fe_3O_4 Coaxial Nanotubes With Hierarchical Porosity as High-Rate Anodes for Lithium-ion Batteries”, *Nano Research*, Vol. 7, No. 11, pp. 1706–1717, 2014.

76. Pan, Z., Y. Lin, B. Sarkar, G. Owens, and Z. Chen, “Green Synthesis of Iron Nanoparticles Using Red Peanut Skin Extract: Synthesis Mechanism, Characterization and Effect of Conditions on Chromium Removal”, *Journal of Colloid and Interface Science*, Vol. 558, pp. 106–114, 2020.

77. Qi, L., Z. Jiaqi, D. Yimin, L. Danyang, W. Shengyun, and C. Ling, “Facile Synthesis of 5-Aminoisophthalic Acid Functionalized Magnetic Nanoparticle for the Removal of Methylene Blue”, *Journal of Materials Science: Materials in Electronics*, Vol. 31, No. 1, pp. 457–468, 2020.

78. Yuan, J., J. J. Zhang, M. P. Yang, W. J. Meng, H. Wang, and J. X. Lu, “CuO Nanoparticles Supported on TiO_2 With High Efficiency for CO_2 Electrochemical Reduction to Ethanol”, *Catalysts*, Vol. 8, No. 4, p. 171, 2018.

79. Zhou, Q., T. T. Li, W. Xu, H. L. Zhu, and Y. Q. Zheng, “Ultrathin Nanosheets-Assembled CuO Flowers for Highly Efficient Electrocatalytic Water Oxidation”, *Journal of Materials Science*, Vol. 53, No. 11, pp. 8141–8150, 2018.

80. Akram, N., J. Guo, W. Ma, Y. Guo, A. Hassan, and J. Wang, "Synergistic Catalysis of $Co(OH)_2$/CuO for the Degradation of Organic Pollutant Under Visible Light Irradiation", *Scientific Reports*, Vol. 10, No. 1, p. 1939, 2020.

81. Liu, Y., L. Ma, D. Zhang, G. Han, and Y. Chang, "A Simple Route to Prepare a Cu_2O–CuO–GN Nanohybrid for High-Performance Electrode Materials", *RSC Advances*, Vol. 7, No. 20, pp. 12027–12032, 2017.

82. Badawy, A. A., N. A. H. Abdelfattah, S. S. Salem, M. F. Awad, and A. Fouda, "Efficacy Assessment of Biosynthesized Copper Oxide Nanoparticles (CuO-NPs) on Stored Grain Insects and Their Impacts on Morphological and Physiological Traits of Wheat (*Triticum aestivum L.*) Plant", *Biology*, Vol. 10, No. 3, p. 233, 2021.

83. Primo, J. de O., C. Bittencourt, S. Acosta, A. Sierra-Castillo, J. F. Colomer, S. Jaerger, V. C. Teixeira, and F. J. Anaissi, "Synthesis of Zinc Oxide Nanoparticles by Ecofriendly Routes: Adsorbent for Copper Removal From Wastewater", *Frontiers in Chemistry*, Vol. 8, p. 2020.

84. Das, J., S. K. Pradhan, D. R. Sahu, D. K. Mishra, S. N. Sarangi, B. B. Nayak, S. Verma, and B. K. Roul, "Micro-Raman and XPS Studies of Pure ZnO Ceramics", *Physica B: Condensed Matter*, Vol. 405, No. 10, pp. 2492–2497, 2010.

85. Chen, M., X. Wang, Y. H. Yu, Z. L. Pei, X. D. Bai, C. Sun, R. F. Huang, and L. S. Wen, "X-ray Photoelectron Spectroscopy and Auger Electron Spectroscopy Studies of Al-Doped ZnO Films", *Applied Surface Science*, Vol. 158, No. 1–2, pp. 134–140, 2000.

APPENDIX: ADDITIONAL FIGURES

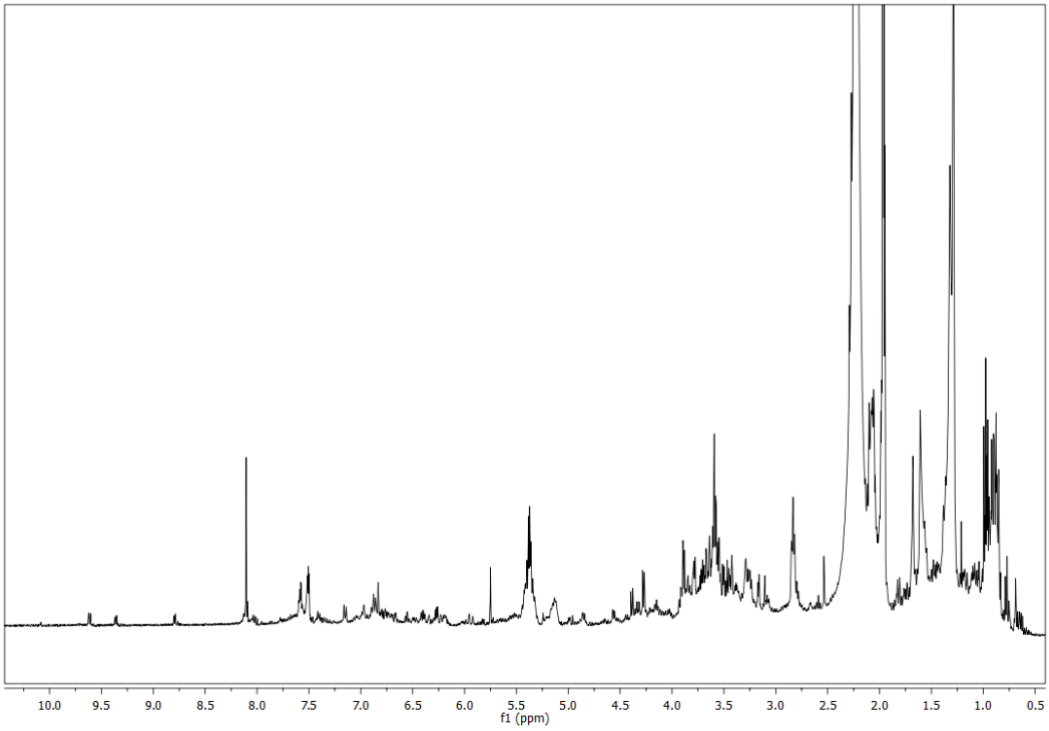

Figure A.1. The ^{1}H-NMR spectrum of *Prunus serrulata* leaf extract in CD_3CN.

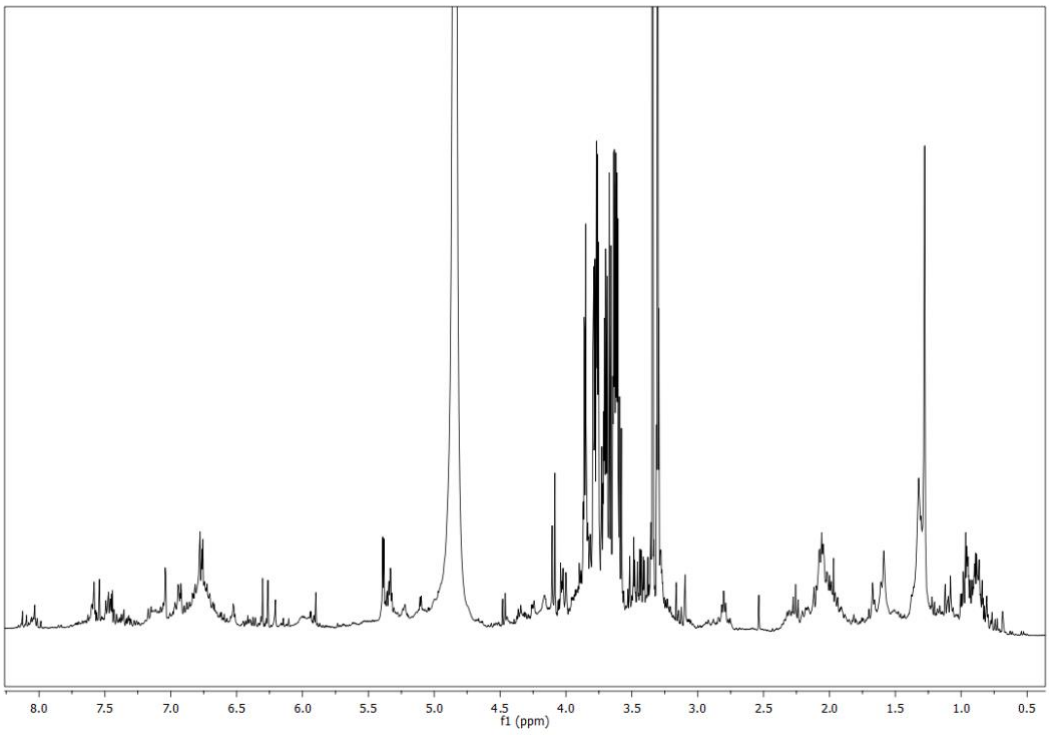

Figure A.2. The ^{1}H-NMR spectrum of *Prunus serrulata* leaf extract in CD_3OD.

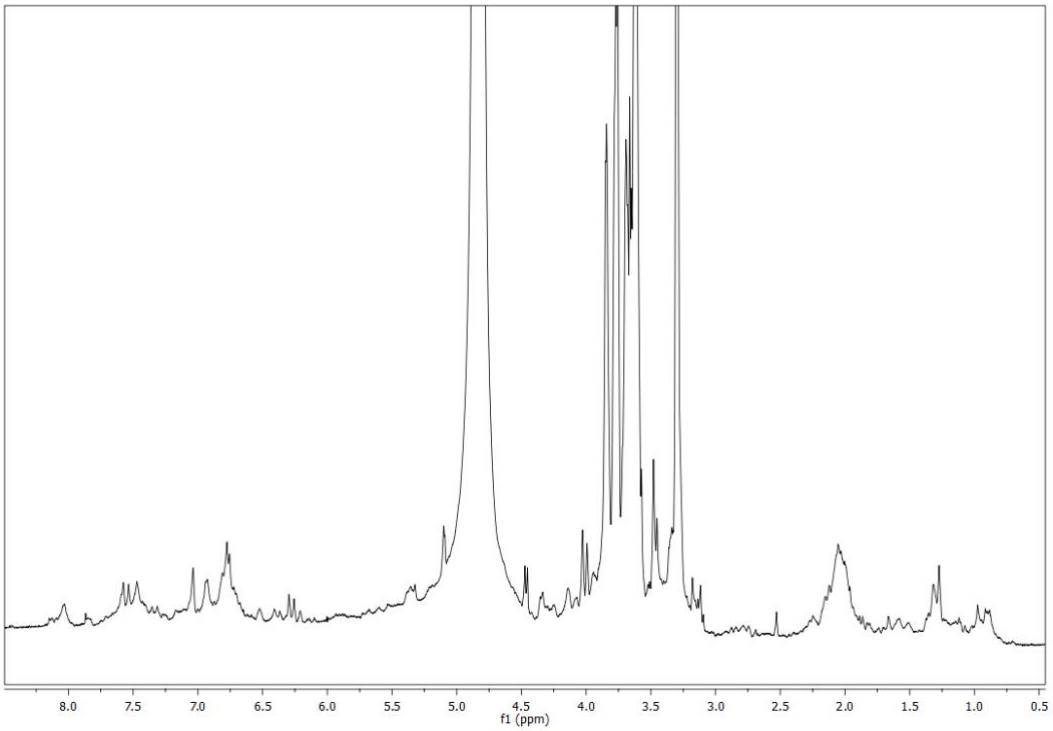

Figure A.3. The ^{1}H-NMR spectrum of *Prunus serrulata* leaf extract in D_2O.